



# Optimal steering control input generation for vehicle's entry speed maximization in a double-lane change manoeuvre

Matthias Tidlund  
Stavros Angelis

Vehicle Engineering  
KTH Royal Institute of Technology

Master Thesis

TRITA-AVE 2013:64  
ISSN 1651-7660

---

**Postal address**  
KTH  
Vehicle Dynamics  
SE-100 44 Stockholm, Sweden

**Visiting Address**  
Teknikringen 8  
Stockholm

**Telephone**  
+46 8 790 6000

**Telefax**  
+46 8 790 9290

**Internet**  
[www.kth.se](http://www.kth.se)

# Acknowledgment

This thesis study was performed between June and November 2013 at Volvo Cars' Active Safety CAE department, which provided a really inspiring environment with skilled colleagues and the opportunity to get an insight of their work. Our Volvo Cars supervisor Diomidis Katzourakis, CAE Vehicle Dynamics engineer, has constantly provided invaluable feedback regarding both the content of the thesis as well as our presentations at Volvo. He has been a great knowledge asset and always available as source of answers and ideas when the vehicle's dynamic complexity was decided and modelled.

We also would like to thank our supervisor Mikael Nybacka, Assistant Professor in Vehicle Dynamics at KTH Royal Institute of Technology, for the support and guidance to reach the goal of delivering a report of high quality, for the scheduling and the timeline of this work, and the opportunity to present this work in parts so to have a better overview of its progress and quality. A special thanks should also be given to Mathias Lidberg, Associate Professor in Vehicle Dynamics at Chalmers Technical University, for his active participation in the project, not only saving us a great deal of time in the beginning by helping us understand the optimization tool Tomlab and the parts within an optimization problem which are most important, but also for constantly providing input with ideas and feedback.

Field tests would have been impossible without the help of Per Hesslund, who installed the robot in the vehicle during both of our testing sessions as well as conducted each test and guided us through the procedure of instrumenting a vehicle and performing a test. We would also like to thank Georgios Minos, Active Safety CAE department's manager, who provided us support with equipment and took care of technicalities like arranging for the vehicle tests in Hällerid as well as giving us the opportunity to take the T1 and T2 test driver courses. Volvo Cars employees that also provided input to this thesis are: Max Boerboom, Johan Hultqvist, Egbert Bakker, Mats Jonasson and Kenneth Ekström.

Matthias is particularly grateful for the support from his parents, Stig and Ingela, throughout the studies as well as Stephanie for her tremendous ability to encourage joy and success.

Stavros would like to specifically thank his family, Nikoleta, Maria and Georgios for their invaluable support as well as Anastasia for being by his side all of this time.

Stockholm November 22, 2013

Matthias Tidlund



Stavros Angelis



# Sammanfattning

Under utvecklingsprocessen av nya fordon sker en strävan mot att reducera fysiska tester, bilindustrier utvecklar därför metoder för att återskapa fysiska testscenarier i virtuella miljöer med hjälp av simuleringsmjukvara. Denna studie har som målsättning att utveckla en metod, med vilken fordonets dynamiska egenskaper kan utvärderas utan att utföra fysiska tester. Målet är att utveckla ett simuleringsverktyg som, i en tidig utvecklingsfas, kan användas av fordonsindustrin och som skulle införa både modifikations- och kalibreringsmöjligheter i detta skede.

Såväl en fordonsmodell som ett anti-sladd system är konstruerat och modellens prestanda i ett dubbelt filbyte, specificerat i ISO3888 del 2, är utvärderad. Då bilens dynamiska prestanda klassificeras utifrån ingångshastigheten i detta test utfördes en optimeringsprocess där hjulens styrvinklar reglerades för att uppnå högsta möjliga hastighet vid testets startposition, detta för att separera fordonets dynamiska klassificering från mänsklig inverkan.

Processen att konstruera fordonsmodellen utfördes med succesivt ökande antal av fordonsegenskaper, från en enkel implementering av en linjär cykel-modell till en tvåspårs-modell med krängning, transienta däckegenskaper, hjulupphängningsegenskaper samt ett anti-sladd system. Resultatet av den optimerade styrregleringen testades i motsvarande fordon på en testbana varefter modellen kunde utvärderas med det verkliga testet som referens.

Genom en utökad möjlighet till simulering kan detta verktyg ge möjligheten att studera fler scenarier såväl som alternativa modelleringskonfigurationer; det kan reducera fysiska tester då fordons dynamiska prestanda ska klassificeras, studeras samt utvärderas.

# Abstract

In an effort to reduce physical testing during the development process of a new vehicle, the automotive industries develop methods that can facilitate the recreation of the physical testing scenarios in virtual environments using simulation software. This thesis aims to develop a method which would help evaluate the vehicle's dynamic properties without it being subjected to physical testing. The goal is to develop a tool that can be used in an early development phase by the industry and that would allow for modifications and calibration to take place.

A vehicle model as well as an electronic stability control implementation is built, and the model's performance to an ISO3888 part-2 double lane change test is evaluated. Since the handling potentials of the vehicle are rated by its entry speed in that test, the model was subjected to an optimization process where its steering action was controlled in order to achieve the highest possible entry speed to the test in an effort to isolate the vehicle's dynamic potential from the influence of a human driver when conducting this test.

The vehicle modelling procedure is done in steps, from a simple implementation of a linear bicycle model to a more complex implementation of a four-wheel vehicle including roll, tire relaxation and suspension compliance properties as well as a simplified ESC implementation. The results of the steering input optimization process were physically tested on a test track, where the correspondence of the model to the real vehicle was evaluated.

By further promoting the vehicle dynamics modelling, this tool can facilitate study more testing scenarios and options and it can serve as a step toward the reduction of the physical testing when the vehicle's dynamic and handling performance need to be studied and evaluated.

# Contents

<b>Acknowledgment.....</b>	<b>i</b>
<b>Sammanfattning .....</b>	<b>ii</b>
<b>Abstract.....</b>	<b>iii</b>
<b>1 Introduction .....</b>	<b>1</b>
1.1 Background .....	1
1.2 Problem description .....	2
1.3 Goal of this thesis .....	2
1.4 Project assumptions.....	2
<b>2 Literature study.....</b>	<b>3</b>
2.1 Optimization.....	3
2.2 Tools for optimization .....	3
2.3 Track boundary creation.....	5
2.4 Vehicle parameters and coordinate systems.....	5
2.5 Bicycle model.....	6
2.6 Four wheel vehicle model.....	9
2.7 Tire behaviour .....	11
2.7.1 Slip angle.....	11
2.7.2 Linear tire model .....	12
2.7.3 Non-linear tire model .....	13
2.7.4 Transient tire properties.....	15
2.7.5 Pneumatic trail .....	16
2.7.6 Camber influence .....	16
2.8 Electronic stability control and its functionalities .....	18
2.9 Vehicle parameter estimation.....	20
<b>3 Methodology .....</b>	<b>23</b>
3.1 Double lane-change track modelling .....	24
3.2 Objective function .....	25
3.3 Point mass trajectory and initial inputs .....	26

3.4	Bicycle model trajectory optimization .....	28
3.4.1	Linear tire model .....	28
3.4.2	Magic formula tire model.....	31
3.5	Car body boundary modelling .....	34
3.6	Four wheel vehicle model trajectory optimization .....	35
3.7	ESC modelling.....	36
3.7.1	Optimal ESC modelling – a torque controller.....	37
3.7.2	Sideslip angle controlled ESC .....	38
3.7.3	Yaw rate error controlled ESC .....	39
3.7.4	Yaw and slip controlled ESC .....	41
3.8	Model refinement.....	42
3.8.1	Wheel kinematics and compliance .....	42
3.8.2	Tire relaxation.....	46
3.8.3	Camber thrust.....	47
3.8.4	Fully featured model without ESC.....	48
3.9	Parameter study .....	51
3.9.1	Vehicle parameter changes .....	51
3.9.2	ESC-characteristics variations.....	53
3.9.3	Influence of discretization .....	54
3.10	Animation of a car along the track.....	55
3.11	Steering robot test 1; driving procedure.....	55
3.11.1	Parameter estimation .....	56
3.12	Steering robot test 2; driving procedure.....	58
<b>4</b>	<b>Results.....</b>	<b>59</b>
4.1	Optimal controller driving inputs.....	60
4.2	Optimal trajectory.....	62
4.3	ESC influence .....	63
4.3.1	Other ESC models investigated.....	67
4.4	Steering robot test 1.....	68
4.4.1	Parameter estimation .....	69

4.5	Steering robot test 2.....	71
4.6	Parameter study.....	75
4.6.1	Mass.....	75
4.6.2	Yaw inertia.....	76
4.6.3	Body width and length .....	77
4.6.4	Roll stiffness.....	79
4.6.5	Tire property changes.....	82
4.6.6	ESC-characteristics variations.....	86
4.6.7	Influence of discretization .....	89
<b>5</b>	<b>Discussion.....</b>	<b>92</b>
5.1	Vehicle dynamics and ESC modelling.....	92
5.2	Results .....	92
5.3	Parameter study and method robustness .....	93
<b>6</b>	<b>Recommendations .....</b>	<b>94</b>
<b>7</b>	<b>Future Work.....</b>	<b>95</b>
<b>8</b>	<b>Nomenclature .....</b>	<b>97</b>
<b>9</b>	<b>References.....</b>	<b>99</b>

## Appendix

- A – ISO 3888 description**
- B – Test vehicle**
- C – Measured data part 1**
- D – Test 2 manoeuvre test list**
- E – Measured data part 2**
- F – Code structure**
- G – Kinematics & compliance**
- H - Test 1 data illustration**
- I - Simulink bicycle model**

# 1 Introduction

Traditionally, the car development procedure includes the building of prototypes and subjecting them to extensive physical testing for assessing overall performance; The double lane change test constitutes a physical test normally used to rate the car's dynamic characteristics. In an effort to reduce development time and promote safety, new development methods should be employed, which do not require prototype vehicles to be built before their behaviour can be estimated.

## 1.1 Background

Rating the handling potentials of a car is a necessary part for the assessment of its safety performance. Such a rating is conducted by independent organizations such as the EuroNCAP and among their tests the electronic stability control systems (ESC) are tested by evaluating the vehicle's lateral and yaw stability [1].

The ISO 3888 Part 2-Obstacle avoidance is a dynamic test where the vehicle is driven closed loop in a severe lane change manoeuvre inducing high lateral accelerations [2]. The test is related to passenger cars<sup>1</sup> and light commercial vehicles up to 3500kg and involves rapidly driving from an initial lane to another parallel lane and then back to the initial one, so as to recreate an obstacle avoidance scenario. During the manoeuvre not one of the cones marking the track should be displaced to assume a valid run. The results of this test serve as a subjective evaluation of the vehicle's handling potential. The test track that defines the manoeuvre can be seen in Figure 1 and more details regarding the test are presented in Appendix A – ISO 3888 description.

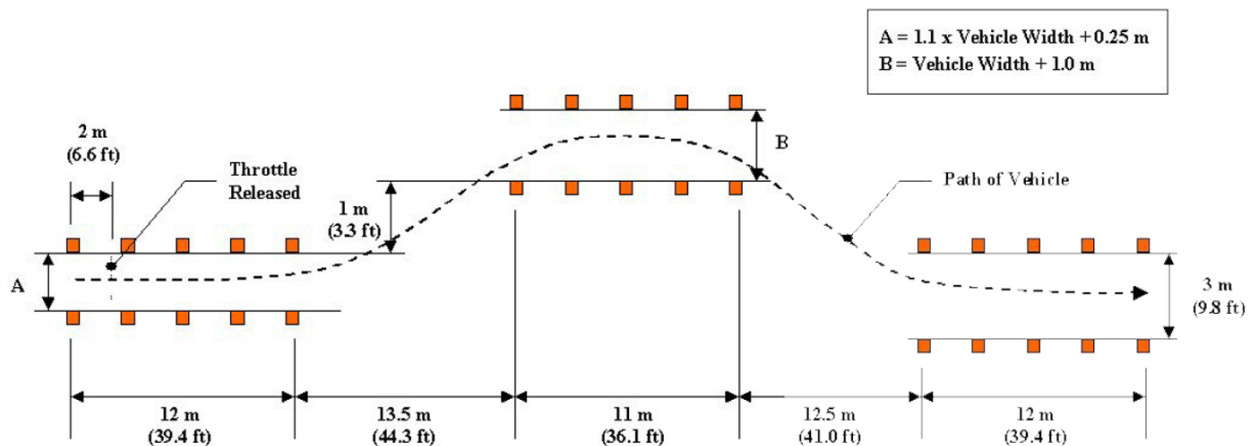


Figure 1. ISO 3888 course, part 2 obstacle avoidance. Definition of the double-lane change track to be used for the entry speed optimization [3]

<sup>1</sup> According to the definition of passenger cars in ISO 3833 [57].

Since a driver controls the car, he or she is involved in the control loop, so these methods are often characterized as unsuitable for objective evaluation. Objective evaluation in an early development stage of the car would be made possible if the driver could be substituted with a controller that determines the optimum steering input to maximize the entry speed.

## 1.2 Problem description

When performing the ISO 3888 part 2 test, objectivity can be achieved if the human driver is not included in the loop, such that the vehicle's contribution to the manoeuvre can be isolated. This substitution would be meaningful if somehow the test drivers are replaced by a "perfect driver model," that would always be able to use the full potential of the vehicle when conducting the test, so that an objective performance metric could be defined. This "perfect driver" model is the optimal steering controller input generator, whose development is the fundamental problem of this study. Usually, when performing vehicle simulations, a driver model controls the steering angle to follow a path. The current problem eliminates that need to simulate such a driver.

## 1.3 Goal of this thesis

The goal of this thesis is to develop a vehicle steering controller that generates the optimal steering inputs that enable maximum vehicle entry speed in a double-lane change manoeuvre. The vehicle should also be operating in conjunction with its ESC system. The rationale is to develop an assessment tool to be used in an early development phase, allowing for direct evaluation of the car's handling and tuning adaptations. This would reduce development time and cost and could potentially promote safety.

## 1.4 Project assumptions

The process of determining the optimal solution requires knowledge of the whole task, with the solution, dependent on all parameters (vehicle properties, double-lane change track dimension, etc.). The controlled systems, steering and ESC, behave optimally according to the objective function.

Model complexity was not limited when the study started; however, when the increase of the model's complexity features did not notably affect the results, no more features were added.

Tire model parameters were estimated from tests performed at dry conditions. All the results from the simulations assumed those parameters to be valid.

Robustness of the optimization algorithm was investigated by changing the ESC torque characteristics, tire model properties, body length and width, mass, yaw inertia and roll stiffness in a range which should cover most passenger cars. Other parameters were held in their nominal values and no more than three parameters were changed at the same time.

# 2 Literature study

Following the aim presented in section 1.3, the interesting areas for this thesis are; theory of optimal control, vehicle models, tire models as well as different extra features such as electronic stability control. This chapter condenses the relevant information for this thesis.

## 2.1 Optimization

If a problem has more than one solution and the goal is to have one single solution as an answer, that would best fulfil some requirements, it is an optimization problem. The problem can be constrained or unconstrained and does not necessarily need to be mathematically described. Often, the problem needs to be solved numerically, meaning that an iterative procedure is used when solving, and then it is necessary to formulate the problem mathematically [4].

The algorithm also influences the solving process as cited below.

*“...there are numerous algorithms, each of which is tailored to a particular type of optimization problem. It is often the user’s responsibility to choose an algorithm that is appropriate for the specific application. This choice is an important one; it may determine whether the problem is solved rapidly or slowly and, indeed, whether the solution is found at all.”*

(Nocedal and Wright [5])

When a local optimum solution is found, meaning that in an infinitesimal neighbouring region of the solution a local optimal solution is obtained, it does not ensure that the solution is the global optimum. There may exist completely different solutions that are better. To guarantee that the solution is the global optimum one must solve the Hamilton-Jacobi-Bellman equation. However, if different bounds are used and the optimization converges to the same point for different starting values, it is an indication that the local optimum is the global optimum [6].

## 2.2 Tools for optimization

In this section, the term, “tools” refers to software but is not limited to a specific runtime environment. Optimization can be done with many different tools after the problem has already been mathematically described; Dyna4 framework [7], VI-carrealtime [8], Mode Frontier, Optimica [9], Matlab [10] and the Matlab extension Tomlab [11] are examples of such tools. Tomlab is the tool that was chosen during this study, for reasons described in chapter 3, and its functionality is described in more detail compared to the other tools. For a complete description of Tomlab the reader is however referred to the manual from Tomlab

[12], and the extensive guide by Stanford [13], which covers the SNOPT solver version 7, is useful to judge the outcome from a solution.

Dyna4 framework is the latest tool from TESISdynaware, and is a successor to Vedyna and Endyna. It performs simulations of vehicle dynamics tests, uses a three dimensional road description, various manoeuvre controls and a driver model [7].

VI-carrealtime is an environment where vehicle simulations can be done in real time. A real time model can be exported automatically from the multi-body dynamics vehicle program ADAMS Car [14]. Optimization studies of vehicle and control system performance can be facilitated. Matlab can be integrated with VI-carrealtime, making it easier to perform various post-processing operations. A track can be set up in a virtual environment in the same way as in Figure 1, but the reference provides poor information about which solvers are actually being used to solve any optimization problem within the program [8].

Mode frontier has the capability of multi-objective and single-objective optimization as well as it has built-in functionality for post-processing. The variables can either be discrete or continuous and the program also has tools to help the user decide if a local optimum, a global optimum or a point in between should be the goal to achieve the most robust design [15].

Optimica is an optimization tool which is based on the Modelica language, it enables high level specification of static and dynamic optimization problems. [9]

Matlab is a high level programming language for analysis of data, algorithms, models and applications [10]. Different toolboxes are used for different purposes, and for optimization Matlab has an optimization toolbox with the option to do minimization through linear programming, binary integer programming, quadratic programming and multi-objective optimization in serial or parallel [16].

Tomlab, which is a Matlab extension, is an optimization tool with the possibility to define abruptly changed constraints over the interval, although not recommended for robustness, as well as it generally solves problems faster than Matlab's built-in optimization tool. It is built to simplify optimization of practical problems and gives access to several solvers at the same time as Matlab can be used for constructing the main program. The Matlab toolboxes for nonlinear programming, parameter estimation, linear optimization and discrete optimization are the base for Tomlab and by integrating all these systems together with new solvers the intention Tomlab has had during the development of the program has been to gather all optimization tools in one place. This also makes it possible to not only solve the optimization problem in one environment but also perform extensive analysis with the help of Matlab [12].

A new variable class, called `tomsym`, is introduced in Matlab with Tomlab; a class that can be used to generate Matlab code for further processing as well as automatically generate first and second order derivatives. `Tomsym` continues to work in two dimensions even when taking matrix derivatives of matrix functions. That implies that Matlab's efficient handling of sparse matrices, matrices with mostly zeros, still can be used, resulting in a faster solution [17].

There also exist a few tools with open source code that everyone can rewrite or adjust; one example is the tool Openopt, which has several own solvers and can solve both linear and nonlinear problems with automatic differentiation features [18].

### 2.3 Track boundary creation

The problem to be optimized, illustrated in Figure 1, is necessary to be formulated in terms of equations, independent of whether those equations have discontinuous derivatives or not. Such mathematical description of a track's boundaries can be done mainly in two ways; either by a set of equations describing each section that still has a continuous derivative, or by the use of equations which are approximations of the boundary. These approximations should then be equal to the real track at least at the positions close to where the optimal trajectory is expected to be. If an approximate boundary is close to the resulting trajectory at some positions, the result may be incorrect.

Corners with infinite or undefined derivative can, according to the Tomlab instructions [6], be described with

$$Y = \frac{1}{2} \left( 1 + \tanh \left( \frac{X}{a_{tr}} \right) \right) \quad \text{Eq. 1}$$

where for  $X \gg a_{tr}$  gives a behaviour that is the same as the real corner and  $a_{tr}$  dictates the corner smoothness.

### 2.4 Vehicle parameters and coordinate systems

In the vehicle dynamics literature, various coordinate systems are used, with the most dominant ones being the American SAE and the German DIN system. In this study the DIN system is used. It is a right hand rule system where the x-axis points forwards, the y-axis points leftwards and hence the z-axis points upwards. The roll, pitch and yaw motions of the car, i.e. the rotational motions around the x-, y- and z-axis respectively, follow the right hand grip rule. The steering angle, denoted as  $\delta$ , is positive when turning towards the left. A visualization of the DIN system is shown in the figure below [19].

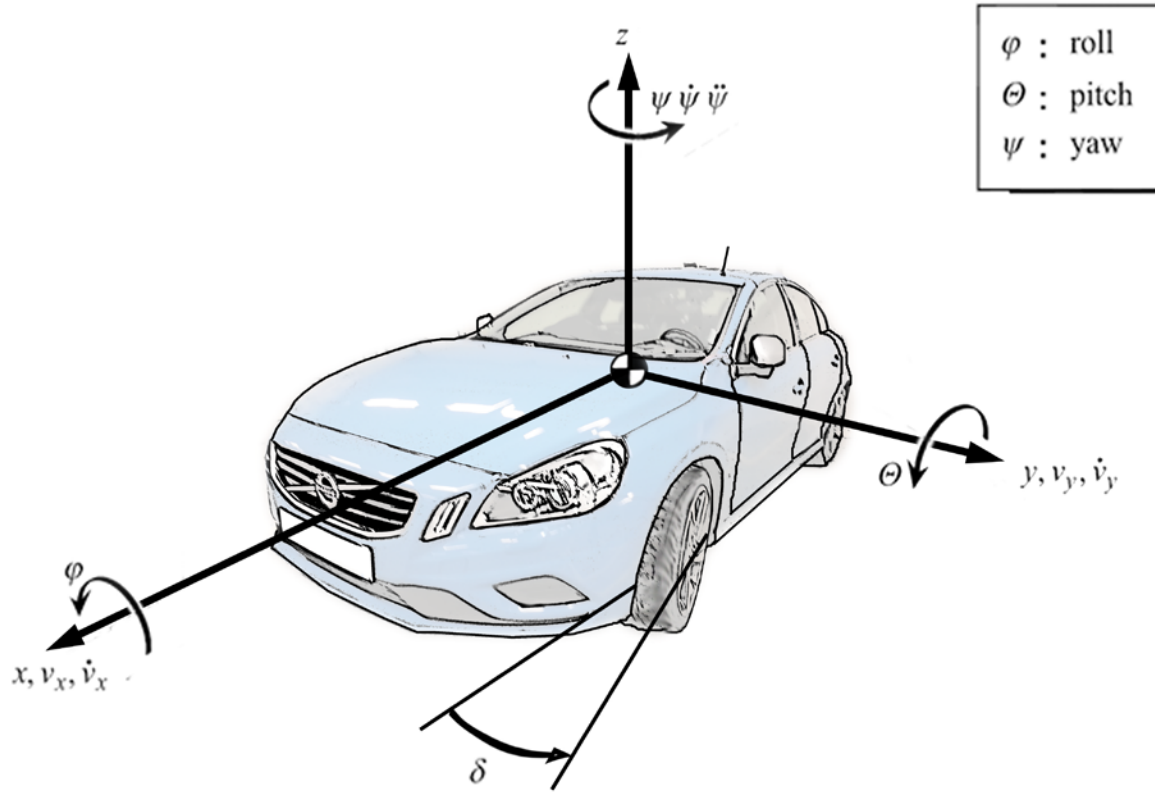


**Figure 2 - DIN coordinate system illustration.**

The SAE coordinate system, differs from the DIN system in that the z- and y-axis points in the opposite directions, that is, the y-axis points rightwards while the z-axis points downwards. The right hand rule for the axes and the right hand grip rule for the rotational motions apply the same.

## 2.5 Bicycle model

In the vehicle dynamics literature there exist various models that describe the motion of the vehicle in space. The simplest model that captures the basic dynamic behaviour of a vehicle is the bicycle or single-track model, developed by Riekert and Schunck in 1940 [20]. Its simplest form is a two-degree of freedom model that captures the lateral and the yaw motion of the vehicle. A three-degree of freedom bicycle model adds the longitudinal motion too, so as to provide a mathematical description of the full vehicle motion in the Global X-Y plane, as shown in Figure 3.

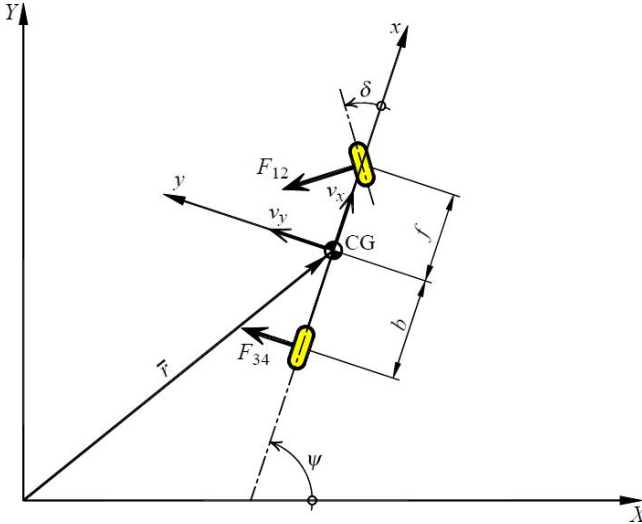


Figure 3 - Illustrated three-degree-of-freedom bicycle model with notations; it is a simplified vehicle model that captures the vehicle's motion in the X-Y plane where the degrees of freedom are the longitudinal, lateral and yaw motion. An index,  $i$ , is used to refer to the front and rear part of the model [19].

The bicycle model is considered to give satisfactory results for lateral accelerations less than 4 [ $\text{m/s}^2$ ]. In this case the forces exerted by the tires can be linearly approximated. The assumptions made by the bicycle model are [21]:

- i. The vehicle's dynamic behaviour is symmetrical between its right and left wheels. Therefore, the left and right vehicle tracks are merged into one.
- ii. The vehicle's centre of gravity (CoG) lies on the road level. This implies that there is no change in the wheel loads during a manoeuvre, and thus no pitch or roll occurs either.
- iii. The lateral forces produced by the tires are linearly dependent on their slip angles.
- iv. The lateral forces of the tires act exactly in the centre of their contact patch with the road, i.e. no pneumatic trail.
- v. The axles' kinematics and elasto-kinematics are modelled in the tires.

The equations of motion for the bicycle model, with respect to the vehicle coordinate system, can be derived using small angle approximation as [22] [19]:

$$m(\dot{v}_x - \dot{\psi}v_y) = -F_{12} \sin(\delta) \approx -F_{12}\delta, \quad \text{Eq. 2}$$

$$m(\dot{v}_y + \dot{\psi}v_x) = F_{34} + F_{12} \cos(\delta) \approx F_{34} + F_{12} \quad \text{Eq. 3}$$

and

$$I_z \ddot{\psi} = fF_{12} \cos(\delta) - bF_{34} \approx fF_{12}\delta - bF_{34} \quad \text{Eq. 4}$$

where  $m$  and  $I_z$  are the vehicle's mass and yaw inertia respectively and on the right side of the approximated equal sign small angle approximations,  $\delta \ll 1$ , have been applied. The vehicle's CoG velocities in the global coordinates  $X$  and  $Y$ , as denoted in Figure 3, are described by [22]:

$$\dot{X} = v_x \cos(\psi) - v_y \sin(\psi) \quad \text{Eq. 5}$$

and

$$\dot{Y} = v_x \sin(\psi) + v_y \cos(\psi). \quad \text{Eq. 6}$$

As mentioned in the bicycle model assumptions, the lateral forces generated by the tires are linearly dependent on their slip angles. This means they can be described as [22] [23] [19]:

$$F_{12} = -C_{12}\alpha_{12} \quad \text{Eq. 7}$$

and

$$F_{34} = -C_{34}\alpha_{34} \quad \text{Eq. 8}$$

where  $\alpha_{12}$  and  $\alpha_{34}$ , the front and rear slip angle respectively, are given by [22] [19]:

$$\alpha_{12} = \tan^{-1} \frac{v_y + f\dot{\psi}}{v_x} - \delta \approx \frac{v_y + f\dot{\psi}}{v_x} - \delta \quad \text{Eq. 9}$$

and

$$\alpha_{34} = \tan^{-1} \frac{v_y - b\dot{\psi}}{v_x} \approx \frac{v_y - b\dot{\psi}}{v_x}. \quad \text{Eq. 10}$$

When Eq. 9 and Eq. 10 are written in the form of the right side of the approximated equal sign, small angle approximations have been applied.  $C_{12}$  and  $C_{34}$  are the front and rear cornering stiffness respectively. The minus sign in Eq. 9 and Eq. 10 is added for convention purposes, such that the cornering stiffness is defined as a positive value [23].

The bicycle model is a simple mathematical description but its practicality is more than just academic, where it is used to introduce the basic vehicle dynamic concepts. It is found also in practical applications determining vehicle attributes like under- and over-steering, stability, peak response time and even for calculating the vehicle's desired yaw rate during a manoeuvre. This desired yaw rate can be compared to the vehicle's actual/measured yaw rate and then corrections can be applied by a stability system.

## 2.6 Four wheel vehicle model

The theory presented in this chapter is based on “Dynamik der Kraftfahrzeuge” [21]. When a more detailed study of the vehicle’s behaviour is desired, than that possible with the bicycle model, then a more detailed model needs to be utilized, with as many degrees of freedom as necessary to capture the desired behaviour. The two-track model is such a model and was the one used in the current study. The two-track model extends the bicycle model in the following basic ways:

- i. There is no symmetry between the left and right wheels of the vehicle regarding its dynamic behaviour. This allows for the modelling of the different steering angles between the left and right wheel (normally invoked by the Ackermann geometry) and therefore the modelling of different slip angles between the right and left wheels.
- ii. The vehicle’s centre of gravity lies at a certain height above the ground. This introduces changes in the wheel loads during a manoeuvre (load transfer), as well as pitch and roll motions. Also, the centre of gravity can be modelled and positioned at a certain lateral position with respect to the vehicle’s longitudinal symmetry axis. This introduces a difference in the static load between the left and right wheels and the normal load on each wheel can then be calculated by [19] [24]

$$F_{zfl} = \frac{mgb\frac{t}{2}}{Lt} - \frac{mh\frac{t}{2}}{Lt} a_x - \frac{m}{t} \left( \frac{h_e K_f}{K_f + K_r - mgh_e} + \frac{b}{L} e_f \right) a_y, \quad \text{Eq. 11}$$

$$F_{zfr} = \frac{mgb\frac{t}{2}}{Lt} - \frac{mh\frac{t}{2}}{Lt} a_x + \frac{m}{t} \left( \frac{h_e K_f}{K_f + K_r - mgh_e} + \frac{b}{L} e_f \right) a_y, \quad \text{Eq. 12}$$

$$F_{zrl} = \frac{mgf\frac{t}{2}}{Lt} + \frac{mh\frac{t}{2}}{Lt} a_x - \frac{m}{t} \left( \frac{h_e K_r}{K_f + K_r - mgh_e} + \frac{f}{L} e_r \right) a_y, \quad \text{Eq. 13}$$

and

$$F_{zrr} = \frac{mgf\frac{t}{2}}{Lt} + \frac{mh\frac{t}{2}}{Lt} a_x + \frac{m}{t} \left( \frac{h_e K_r}{K_f + K_r - mgh_e} + \frac{f}{L} e_r \right) a_y \quad \text{Eq. 14}$$

where  $K_f$  is the roll stiffness at the front,  $K_r$  is the roll stiffness at the rear<sup>2</sup>,  $e_f$  is the height of the roll centre at the front,  $e_r$  the height of the roll centre at the rear.  $h_e$  is the distance of the centre of gravity from the roll axis, given by

$$h_e = h - \frac{f \cdot e_b + b \cdot e_f}{L}. \quad \text{Eq. 15}$$

---

<sup>2</sup> The term “roll stiffness” includes not only the stiffness imposed by antiroll bars, but also from the suspension geometry, springs, frame, and all the factors that contribute to the axle’s total roll stiffness in general.

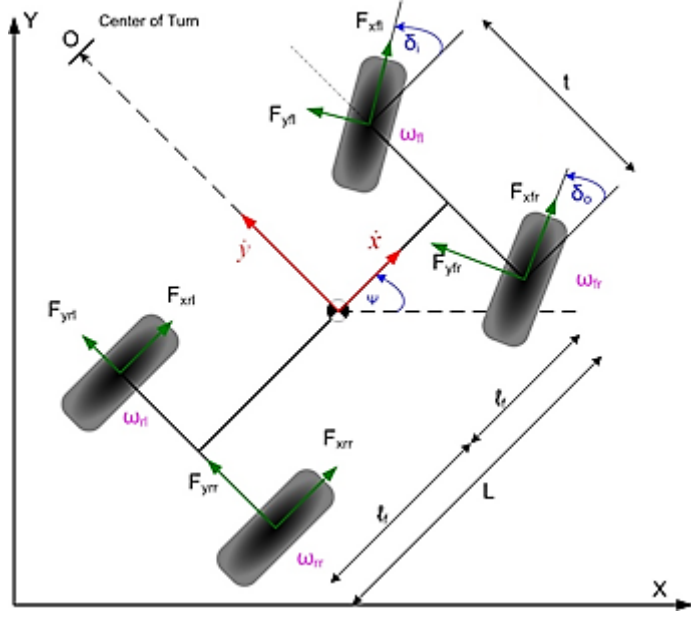


**Figure 4.** Two track model with notations [25]; index  $i$  is front or rear as for the bicycle model and index  $j$  is left or right when referring to one of the vehicle's wheels or corners.

The equations of motion in the case of the two-track front wheel steer vehicle, Figure 4, are given by

$$m(\dot{v}_x - \dot{\psi}v_y) = F_{xfl} \cos \delta_i + F_{xfr} \cos \delta_o + F_{xrl} + F_{xrr} - F_{yfl} \sin \delta_i - F_{yfr} \sin \delta_o, \quad \text{Eq. 16}$$

$$m(\dot{v}_y + \dot{\psi}v_x) = F_{yrl} + F_{yrr} + F_{xfl} \sin \delta_i + F_{xfr} \sin \delta_o + F_{yfl} \cos \delta_i + F_{yfr} \cos \delta_o, \quad \text{Eq. 17}$$

$$I_z \ddot{\psi} = f(F_{yfl} \cos \delta_i + F_{yfr} \cos \delta_o + F_{xfl} \sin \delta_i + F_{xfr} \sin \delta_o) - b(F_{yrl} + F_{yrr}) + W_l(F_{yfl} \sin \delta_i + F_{yrl} - F_{xfl} \cos \delta_i - F_{xrl}) + W_r(F_{xfr} \cos \delta_o + F_{xrr} - F_{yfr} \sin \delta_o) \quad \text{Eq. 18}$$

and the wheel rotation dynamics by

$$I_w \dot{\omega}_{ij} = T_{ij} - F_{xij}r. \quad \text{Eq. 19}$$

Translation between the local and global coordinate systems can still be performed with Eq. 5 and Eq. 6. The calculation of the forces generated by the tires depends on the tire model that is used. If a linear approximation is used, then the calculation is the same as in the case

of the bicycle model described in sections 2.5 and 2.7.2. In the case of a magic formula tire model the force calculation is conducted as described in section 2.7.3. Other details can be added if desired, as:

- i. More detailed tire modelling: The tires can be modelled by utilizing models like the Dugoff model, the Brush model or the Magic Formula model [23]. These models capture the tire behaviour also in the nonlinear tire region, which makes them suitable for cases where the lateral accelerations exceed  $0.4g$ . Also, the lateral force can be modelled to act at a point different than the centre of the tire-road contact patch, i.e. the pneumatic trail.
- ii. Suspension kinematics and compliance phenomena can also be modelled, and not included in the tire modelling, like in the bicycle model case.

As the details captured by the vehicle model increase, a significant computational cost is also introduced, and this is the main disadvantage of the two-track model. This model is most often used when performing suspension analysis/design or ride and comfort studies since it captures load transfer, roll and pitch motions that primarily affect those factors.

## 2.7 Tire behaviour

In this chapter the most fundamental concepts and principles of tire behaviour are presented. It is intended to serve as an introduction to the tire related modelling details that have been used in this study rather than a complete description of all existing models, which could have been used.

### 2.7.1 Slip angle

When a pneumatic tire is subjected to a lateral load while rolling, its sidewalls deform, and it deflects along a direction different than that defined by the wheel plane [23]. This difference in the directions between the wheel's plane and the velocity vector of the wheel's centre is called “slip angle<sup>3</sup>”, see Figure 5. The slip angle is intertwined with the lateral tire force generation that is acting on the wheel, called “cornering force”, which causes changes in the vehicle direction during the manoeuvre.

---

<sup>3</sup> The tire's slip angle is different than the vehicle's slip angle (also called sideslip angle or float angle), which is the angle between the longitudinal axis of the vehicle and the velocity vector acting on its centre of gravity, or  $\beta = \tan^{-1}(v_y/v_x)$ , where  $v_y$  and  $v_x$  are the vehicle's lateral and longitudinal velocity respectively [20] [52].

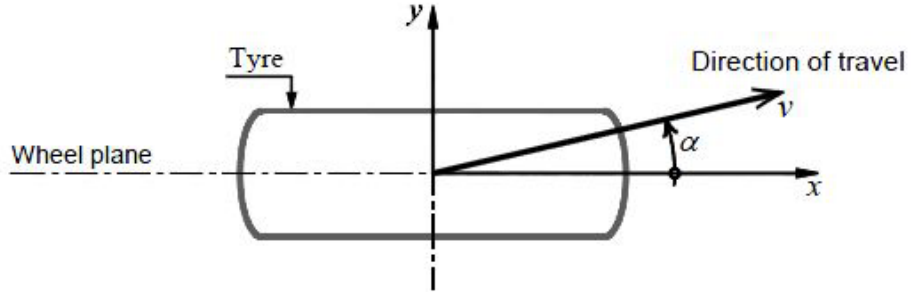


Figure 5. Slip angle definition [23].

A non-zero slip angle arises because of deformation in the tire. As the tire rotates, the friction between the contact patch and the road results in individual tread elements remaining stationary with respect to the road. This tire deflection gives rise to the slip angle and the cornering force [26].

### 2.7.2 Linear tire model

For small slip angles the lateral force increases approximately linearly for the first few degrees of slip, called the elastic region, and then increases non-linearly to a maximum before beginning to decrease. A typical diagram relating the lateral force to the wheel slip angle is presented below in Figure 6.

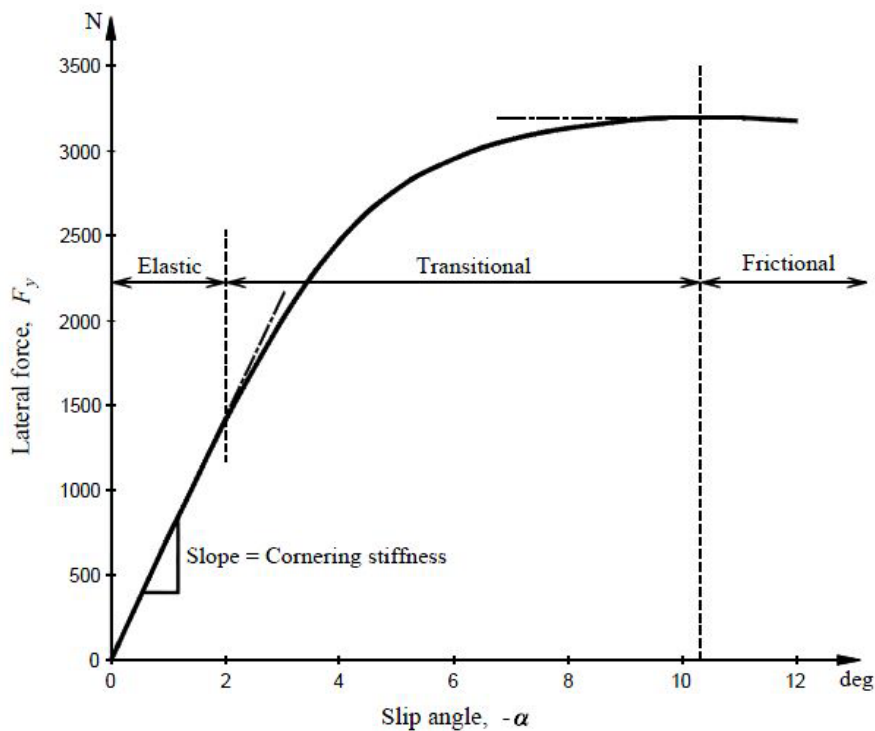


Figure 6. For small slip angles the lateral force is linearly proportional to the slip angle. The figure shows a typical example of this relationship. The numbers and regions noted above depend on factors like tire size, tire pressure and normal load [23].

This linear relationship can be formulated as

$$F_y = -C_a \cdot \alpha \quad \text{Eq. 20}$$

where  $C_a$  is called the cornering stiffness of the tire, defined as [23]

$$C_a = -\left(\frac{\partial F_y}{\partial \alpha}\right)_{\alpha=0}. \quad \text{Eq. 21}$$

It is noteworthy to emphasize that this relationship holds only for small slip angles, as shown also in Figure 6.

### 2.7.3 Non-linear tire model

While the linear tire model gives satisfactory results for small slip angles, where the tire is considered to be in its linear region<sup>4</sup>, it needs to be either improved or replaced for larger slip angles. Many tire models can be found in the literature, and one of the most well-known is the “magic formula” model, which is an empirically derived curve fit. It utilizes a combination of trigonometric functions rather than a polynomial, which is a more usual fitting method, and it is the result of studies carried by Egbert Bakker and Lars Lidner and Hans B. Pacejka [27]. Largely owing its popularity to the fact that its equations were made public, the Magic Formula has very quickly been adopted from the industry as a standard tire model for vehicle handling simulations. Since its first appearance in 1987 various modifications have been made to improve the accuracy and to extend the capabilities of the model, and include factors like the camber angle, the tire inflation pressure, the rolling resistance and the overturning moment, and depending on the vehicle type or the phenomena that one wishes to study, each version may better apply to some certain situations [20][21].

The most used version of the formula is

$$\begin{aligned} f(u) &= D \sin(C \tan^{-1}(Bu - E(Bu - \tan^{-1}(Bu)))) \\ F(U) &= f(u) + S_v \\ u &= U + S_h \end{aligned} \quad \text{Eq. 22}$$

where  $F(U)$  represents the output, that is the lateral or longitudinal force, or the self-aligning torque and  $U$  denotes the input, that is the slip angle  $\alpha$  or the longitudinal slip  $\kappa$  [26].

---

<sup>4</sup> The linear region is usually considered for up to  $0.4g$  [22] [43].

A simplified version of Eq. 22 also exists, which is an early version of it, and gives a relation between the friction coefficient,  $\mu$ , and the resultant tire slip,  $s$ , at a given tire. The expression holds as follows

$$\mu(s) = D \sin(C \tan^{-1}(Bs)) \quad \text{Eq. 23}$$

where  $D$ ,  $C$  and  $B$  are the peak value factor, shape factor and stiffness factor respectively. The product  $B \cdot C \cdot D \cdot F_z$ , where  $F_z$  is the normal load on the tire, represents the cornering stiffness  $C_{ij}$  of the tire with index  $ij$  [28] [29].

The resultant slip,  $s$ , is given by

$$s = \sqrt{s_x^2 + s_y^2} \quad \text{Eq. 24}$$

where the indices x and y denote the longitudinal and lateral slip respectively [28] [22] [23].

From the friction coefficient  $\mu$ , assuming linear dependence of the tire friction forces on the tire vertical force, one can calculate the resultant friction force on the plane of the road surface as

$$f = \sqrt{f_x^2 + f_y^2} = \mu f_z \quad \text{Eq. 25}$$

where the friction coefficient is related to its longitudinal and lateral component according to

$$\mu = \sqrt{\mu_x^2 + \mu_y^2} \quad \text{Eq. 26}$$

and the lateral and longitudinal forces are then obtained from Eq. 27 [28] [22] [23].

$$\begin{aligned} f_x &= \mu_x f_z = -\frac{s_x}{s} \mu f_z = -\frac{s_x}{s} f \\ f_y &= \mu_y f_z = -\frac{s_y}{s} \mu f_z = -\frac{s_y}{s} f \end{aligned} \quad \text{Eq. 27}$$

Assuming the above behaviour, the tire's force potentials move inside a so called "friction circle", or in general a "friction ellipse", as indicated by Eq. 26 and illustrated in Figure 7.

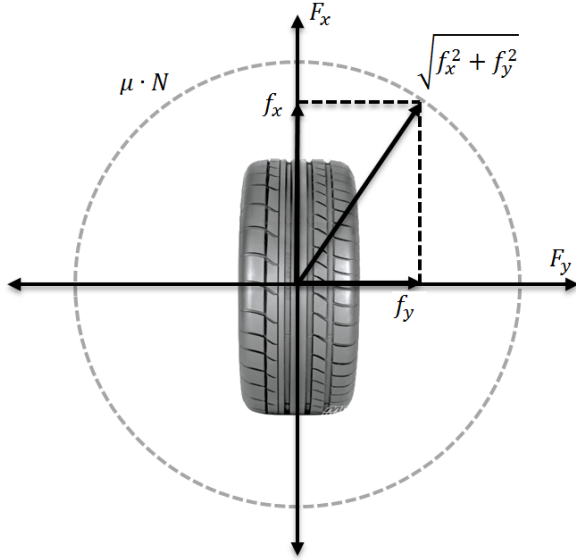


**Figure 7.** Illustration [30] of the friction circle, the total force can never exceed a certain limit [24] [31].

This means that a tire has a limit to the lateral force that it can produce for a given value of the longitudinal force and vice versa, such that the resultant force never reaches out the friction circle, which is a characteristic of each tire [28] [22] [23].

#### 2.7.4 Transient tire properties

As mentioned above, the deformation of the tire during a cornering manoeuvre gives rise to a slip angle which results in a lateral force generation on the tire. This lateral force will not appear instantly on the tire though. A delay between the slip angle application and the lateral force generation is always present. After a steering angle is imposed, the wheel needs to travel a certain amount of length, during which the tire will gradually begin to deform and build up the lateral force up to its steady state value. This length,  $L_{relax}$ , is called *relaxation length* and it is a characteristic property of the pneumatic tires. Half to one wheel turn is a typical amount of roll needed for the force to build up to its steady state value [22] [23] [31].

A way to define this transient behaviour is through the first order differential equation

$$\tau \dot{f}_y(a, t) + f_y(a, t) = f_{yss}(a) \quad \text{Eq. 28}$$

where  $\tau$  is a time constant and  $f_{yss}$  is the steady state value of the lateral force for a given slip angle  $a$ . The time constant is related to the relaxation length as

$$\tau = \frac{L_{relax}}{V_x} \quad \text{Eq. 29}$$

where  $V_x$  is the tire's longitudinal velocity. When reading equation Eq. 29 the relaxation length is taken as a constant value, a characteristic of the tire. But in reality the relaxation length is dependent on the level of slip, more specifically, the higher the slip angle, the shorter the relaxation length becomes [26].

### 2.7.5 Pneumatic trail

When a pneumatic tire is subjected to a lateral load while rolling, as it is in the case of cornering, it will produce lateral forces throughout the whole length of its contact patch. Due to the asymmetrical deformation of the tire, these tire forces will also be asymmetrically distributed and thus the resultant lateral force will be a force applied to some distance behind the centre of the contact patch<sup>5</sup>. This distance is called the *pneumatic trail* and for low lateral accelerations, linear tire region, the pneumatic trail is almost constant<sup>6</sup>. For higher lateral accelerations (large slip angles/nonlinear tire region) the tire deformation becomes more symmetric, and thus the pneumatic trail becomes smaller reducing to almost zero, and in some cases it might even change sign [23] [24] [32] [26].

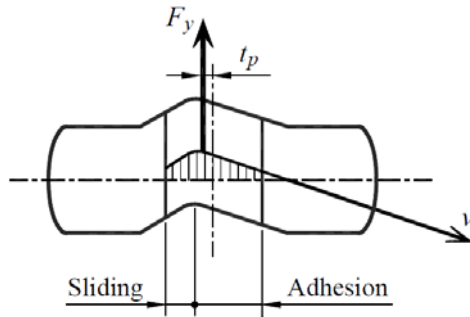


Figure 8. The asymmetrical deformation of the tire in low slip angles results in a lateral force  $F_y$  acting at a distance  $t_p$  behind the centre of the contact patch. This distance is called the pneumatic trail [23].

### 2.7.6 Camber influence

The angle between the vertical plane and the plane defined by the wheel is termed as camber angle; it can be measured either with respect to the vehicle body or with respect to the ground as shown in Figure 9. In the first case the camber angle is denoted as  $\epsilon$  and it is considered positive when the top of the wheel tilts outwards from the vehicle body.

<sup>5</sup> This phenomenon, of a force applied at a certain distance, gives rise to a moment. This moment tends to steer the wheel back to its straight position, and is therefore called aligning moment. The aligning moment is an important concept of the steering design [17] [19] [22].

<sup>6</sup> In this model, a typical value for the pneumatic trail at low lateral accelerations was used, equal to approximately 30mm [30].

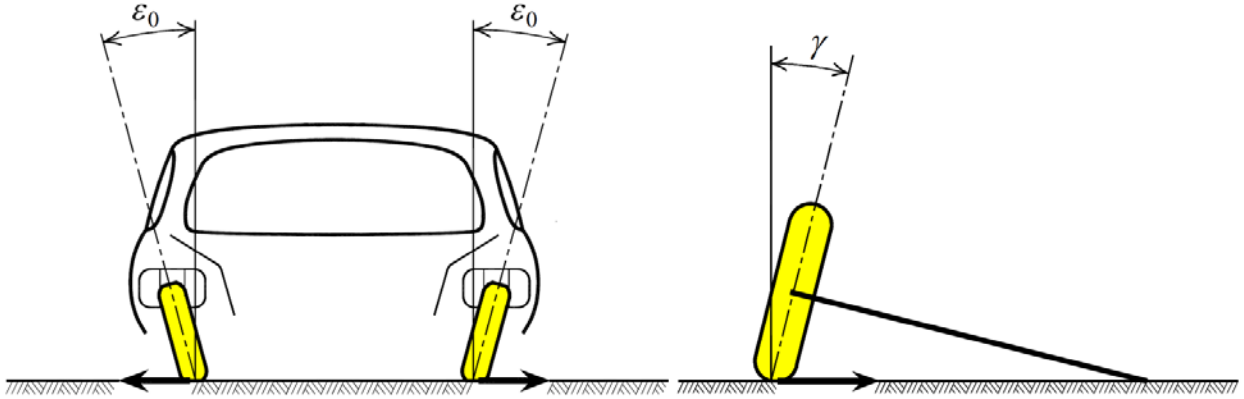


**Figure 9.** Positive camber angle definitions with respect to the vehicle body and the ground, as seen from behind. The lateral force generation due to camber is also shown. This force acts toward the direction of the apex of the virtual cone defined by the wheel [19].

This means that when both the left and right wheel have positive camber  $\varepsilon$  they are tilted towards opposite directions. In the second case, when the camber angle is defined with respect to the ground – also termed as inclination angle of the wheel, it is denoted as  $\gamma$  and it is considered positive when the wheel is tilted in the clockwise direction as seen from behind [23] [24] [31] [19] [26]. This time, when the wheels of an axle have positive inclination angle, they both tilt toward the same direction. It is often that the wheels on a vehicle have a pre-set camber angle so that some desired ride and handling characteristics, like for example performance and safety, are achieved [26] [33]. This camber pre-set, which the wheels have when at rest, is called *static camber*.

While manoeuvring the vehicle will be subjected to wheel steer, body roll and suspension jounce/rebound movements. These factors affect the camber angle. This change to the camber angle due to wheel steer and suspension travel (body roll), which depends on the suspension design, is called *camber gain*. The camber of the wheel is important since it generates a force towards the direction of the tilt when the wheel rolls, as shown also in Figure 9 above, termed as *camber thrust* [24]. The lateral force due to camber is much lower than the one due to the slip angle, but it does nevertheless add to the lateral force due to slip and can play an important role for handling characteristics like understeer and oversteer [19]. It is therefore important that camber relative to the ground is always as near as possible to its optimal value (taken care by the camber gain of the suspension), so that the desired handling behaviour is achieved, while also other factors like braking ability or tire wear are not compromised. An interesting study on this camber optimization can be found in [33].

The lateral force due to camber can be calculated as [19] [31]

$$F_\gamma = -C_\gamma \cdot \gamma \quad \text{Eq. 30}$$

where  $C_\gamma$  is called the *camber stiffness* and the minus sign is a convention such that  $C_\gamma$  is positive. The contribution of the camber angle to the lateral force is complex; in the linear region the camber thrust and lateral force due to slip can be considered as separate and additive effects, but when the tire enters its nonlinear region the camber thrust's additive effect decreases, a behaviour termed as “camber roll-off” [24]. In recent improvements in the magic formula equation, camber is one of the factors that can be taken into consideration by the formula [34] [26].

## 2.8 Electronic stability control and its functionalities

The electronic stability control (ESC) is a system used to prevent the vehicle’s path to deviate from the desired path [22]. ESC may also be referred to as yaw stability control systems and automotive manufacturers use numerous other branded names. The yaw rate relationship to the steering wheel angle is very different for small and large slip angles. Manoeuvrability is lost at different steering angles for different surfaces [22]. The vehicle’s yaw rate is controlled by the steering wheel angle, and could pose difficulty for the driver to utilize the maximum available physical adhesion between the tires and the road [35] [36]. At the same time the need for driving stability motivates the ESC principle [22].

The ESC can influence the yaw rate by adapting the braking torque and steering angle that is applied to each wheel. ESC can apply differential braking to generate yaw moment; those systems can also utilize torque vectoring to independently control the drive torque. In Steer-by-wire systems the steering angle can be controlled by the ESC system [22].

To employ such control, the vehicle needs to be equipped with a yaw rate sensor, a lateral acceleration sensor, wheel speed sensors and a steering wheel angle sensor. Assuming that certain vehicle and environment properties are known (friction coefficient, tire cornering stiffness, etc...), the sensors make it possible to calculate the desired slip angle as described by Eq. 31 [22].

$$\beta_d = \frac{b - \frac{fmV^2}{2C_{ar}(f + b)}}{(f + b) + \frac{mV^2(fC_{af} - bC_{ar})}{2C_{af}C_{ar}(f + b)}} \delta_{ss} \quad \text{Eq. 31}$$

It is also possible to calculate the steady state relation between the steering angle and the radius of the vehicle trajectory according to

$$\frac{1}{R} = \frac{\delta_{ss}}{(f + b) + \frac{mV^2(fC_{af} - bC_{ar})}{2C_{af}C_{ar}(f + b)}} \quad \text{Eq. 32}$$

which implies that the desired yaw rate is given by Eq. 33 [22]

$$\psi_d = \frac{\dot{x}}{R} = \frac{\dot{x}\delta_{ss}}{(f+b) + \frac{m\dot{x}^2(fC_{af} - bC_{ar})}{2C_{af}C_{ar}(f+b)}} \quad \text{Eq. 33}$$

and the yaw acceleration is given by Eq. 18.

The friction coefficient of the road influences the yaw rate that the vehicle can develop. An upper limit for the yaw rate that the controller can achieve is given by

$$\dot{x}\dot{\Psi} - \tan(\beta)\ddot{x} + \frac{\dot{x}\dot{\beta}}{\sqrt{1 + \tan^2(\beta)}} \leq \mu g \quad \text{Eq. 34}$$

according to [22]. The next step for the controller is to determine the desired yaw torque to track the target yaw rate and slip angle [22]. The objective of tracking yaw rate and slip angle can be done with sliding mode control design, where the sliding surface is chosen so either the yaw rate, the slip angle or a combination of them is tracked [37] [38] [39] [40]. Rajamani [22] suggests the use of the formula given in Eq. 35, and also suggests the reader who wants an introduction to the subject to look further in the text by Slotine and Li [41].

$$s = \dot{\Psi} - \dot{\Psi}_d + \xi(\beta - \beta_d) \quad \text{Eq. 35}$$

In Eq. 35,  $\xi$  is a weighting factor for the slip angle contribution,  $\beta$  is the sideslip angle,  $\beta_d$  is the desired sideslip angle and  $s$  can be seen as a surface. If one can ensure that the vehicle response converges to  $s = 0$  the desired yaw rate and slip angle are obtained. The differentiation of Eq. 35 is then given by Eq. 36 [22].

$$\dot{s} = \ddot{\Psi} - \ddot{\Psi}_d + \xi(\dot{\beta} - \dot{\beta}_d) \quad \text{Eq. 36}$$

By assuming a small steering angle, a fixed brake ratio,  $\rho$ , between the front and rear wheel on each side of the car, the yaw acceleration is given by Eq. 38 with the yaw torque generated by the brakes defined by Eq. 37.

$$M_{\Psi_b} = \frac{l_w}{2} (F_{xfr} - F_{xfl}) \quad \text{Eq. 37}$$

$$\ddot{\Psi} = \frac{1}{I_z} [f(F_{yfl} + F_{yfr}) \cos(\delta) - b(F_{yrl} + F_{yrr}) + (\cos(\delta) + \rho)M_{\Psi_b}] \quad \text{Eq. 38}$$

and setting  $\dot{s} = -\eta s$  when substituting for  $\ddot{\Psi}$  it yields the control law in Eq. 39 [22].

$$M_{\Psi_b} = \frac{\frac{b(F_{yrl} + F_{yrr})}{I_z} - \frac{f(F_{yfl} + F_{yfr})}{I_z} - \eta s + \ddot{\Psi}_d - \xi(\dot{\beta} - \dot{\beta}_d)}{\frac{\rho + \cos(\delta)}{I_z}} \quad \text{Eq. 39}$$

Estimations for the sideslip angle, sideslip angle derivative and each of the lateral tire forces are needed, and for the interested reader some literature [42] [36] [43] [44] is suggested. After the desired torque,  $M_{\Psi_b}$ , produced by the differential braking has been calculated, the brake pressure can be calculated as the torque produced by differential braking is directly coupled to the dynamics of the wheels. If only the front wheels are used for braking the resulting equations for left,  $P_{bfl}$ , and right,  $P_{bfr}$ , brake pressure can be seen in Eq. 40 and Eq. 41 respectively [22].

$$P_{bfl} = P_0 - a \frac{\left(\frac{2M_{\Psi_b}}{l_w}\right) r_{eff}}{A_w \mu_b R_b} \quad \text{Eq. 40}$$

$$P_{bfr} = P_0 + (1 - a) \frac{\left(\frac{2M_{\Psi_b}}{l_w}\right) r_{eff}}{A_w \mu_b R_b} \quad \text{Eq. 41}$$

If small steering angles cannot be assumed, the yaw torque that should be generated by the brakes needs to be calculated from each force for each wheel in Eq. 18.

## 2.9 Vehicle parameter estimation

The procedure of performing a parameter estimation of the tire properties can be performed in three steps which are described in this chapter and are all based on the paper “An enhanced generic single track vehicle model and its parameter identification for 15 different passenger cars” [45].

### *Circular driving test – Effective cornering stiffness estimation*

The vehicle’s effective cornering stiffness<sup>7</sup>, for the front and rear axle, can be calculated from the results of circular driving tests. The necessary data for calculating the effective cornering stiffness are the vehicle’s lateral acceleration, forward velocity, lateral velocity, yaw rate and steering wheel angle. The bicycle model, presented in section 2.5, is used for simplicity in the calculations.

---

<sup>7</sup> By the term “effective” cornering stiffness the contribution of additional phenomena to the axle’s cornering stiffness is described. An axle’s cornering stiffness does not depend only on the tires but also on phenomena like camber forces, tire load sensitivity, steering elasticity and compliance steer, all of which contribute to the reduction of the cornering stiffness imposed by the tires alone [26] [17].

As a first step, equation Eq. 60 and Eq. 61 are used to calculate the slip angle of the front and rear wheel. The semi steady-state test assumes  $\ddot{\psi} = 0$ , since the turning radius is approximately the same. Then, from Eq. 3 and Eq. 4, the lateral forces on the front and rear axle are calculated as

$$F_{12} = \frac{b}{L} m \alpha_y \quad \text{Eq. 42}$$

and

$$F_{34} = \frac{f}{L} m \alpha_y. \quad \text{Eq. 43}$$

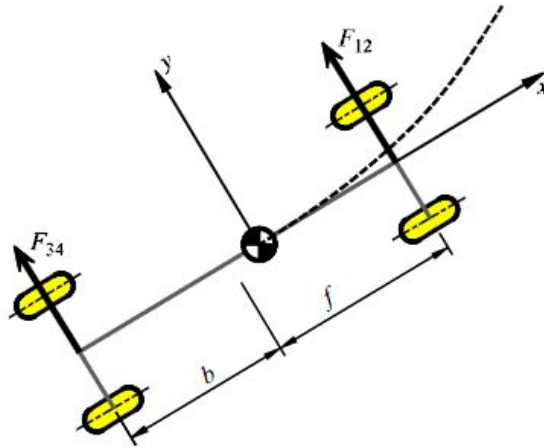


**Figure 10.** Lateral forces during cornering [19].

Next, the lateral forces, as can be seen in Figure 10, at the front and rear are plotted against the respective slip angles, resulting in a graph similar to Figure 6. The gradient of the curve for zero slip angle is the axle's effective cornering stiffness [23] [24], that is

$$C_a = \left( \frac{\partial F_y}{\partial a} \right)_{a=0} \quad \text{Eq. 44}$$

as also mentioned in Eq. 21.

#### Pseudorandom steering test – Yaw inertia calculation

The yaw inertia of the vehicle can be calculated by the results of a pseudorandom steering test. From this test the transfer functions from the measured steering angle to measured lateral acceleration and yaw rate can be obtained by calculating the fraction of the fast Fourier transform (FFT) of the output signal (lateral acceleration or yaw rate) over the FFT of the input signal (steering angle). From the bicycle model the expressions in Eq. 45 and Eq. 46, for analytically calculating these transfer functions, are obtained [19]:

$$\frac{\psi}{\Delta} = \frac{fC_{12}ms + \frac{L}{v_x}C_{12}C_{34}}{mI_zs^2 + \frac{(f^2C_{12} + b^2C_{34})m + I_z(C_{12} + C_{34})}{v_x}s + \frac{L^2C_{12}C_{34}}{v_x^2} + m(bC_{34} - fC_{12})} \quad \text{Eq. 45}$$

and

$$\frac{A_y}{\Delta} = \frac{v_x^2}{L + K_{us}v_x^2} \cdot \frac{1 + \frac{b}{v_x}s + \frac{I_z}{LC_{34}}s^2}{1 + v_x \frac{(f^2C_{12} + b^2C_{34})m + I_z(C_{12} + C_{34})}{LC_{12}C_{34}(K_{us}v_x^2 + L)}s + \frac{mI_zv_x^2}{LC_{12}C_{34}(K_{us}v_x^2 + L)}s^2} \quad \text{Eq. 46}$$

with the understeer gradient

$$K_{us} = \frac{m(bC_{34} - fC_{12})}{LC_{12}C_{34}}. \quad \text{Eq. 47}$$

The yaw inertia,  $I_z$ , value is then calculated by an optimization, where the error between the transfer functions calculated from the measurements and the transfer functions calculated analytically from the bicycle model is minimized by varying the  $I_z$  value accordingly.

### *Magic formula coefficients*

Next, the  $D$  value of the magic formula model for the tires can be calculated from a severe lane change manoeuvre test, like the double lane change. A number of lane change manoeuvres are conducted and recorded. For the coefficients calculation the manoeuvre with the highest achieved lateral acceleration is selected. From that manoeuvre, the peak lateral force of the tires is obtained and therefore the  $D$  value of the magic formula is found (since  $D$  defines the peak value of the magic formula curve). The  $C$  value can be assumed to be <sup>8</sup>, which means that the curve of the magic formula does not fall for large slip angles (i.e. the peak value force is not decreasing for large slip angles) which then leads to the calculation of the  $B$  value as

$$B = \frac{C_{Fa}}{CD}. \quad \text{Eq. 48}$$

where  $C_{Fa}$  is the *tire cornering stiffness*.

---

<sup>8</sup> The  $C = 1$  assumption facilitates an approximation of the magic formula curve for the tire. In general,  $C$  can be determined by the use of regression procedures [51].

# 3 Methodology

The problem of optimizing the steering control input generation for a vehicle's entry speed maximization in a double-lane change manoeuvre can be divided into the following smaller problems:

- Double-lane change track modelling
- Point mass trajectory optimization
- Bicycle model trajectory optimization
- Four wheel vehicle model trajectory optimization
- Electronic stability control implementation
- Model refinement
- Complete vehicle model optimal iteration process procedure

One of the first steps was to select the optimization tool to use. Matlab [10] was selected for pre- and post-processing and Tomlab [11] was selected for the optimization process. Tomlab was seen as an appropriate choice, since it offered its functionalities within Matlab. A general coding layout to be used in all models used in this study can be seen in Appendix F – Code structure.

A parameter study, in which “key” vehicle properties were altered, offered a study on the robustness of the method and demonstrated the way the parameters can influence the entry speed, as well as how close to the final result the initial guess needs to be. Visualization was also made by animating the vehicle, making it possible to examine the vehicle’s movement at any position and take a closer look at some parts. This type of evaluation is important since the car body should be discretized in as few points as possible to make the numerical solution converge faster, but between two discrete points it is possible that the car hits a corner of the track.

Further evaluation of the results with a driving robot in a real car was also done; a first test to improve the realism of the vehicle dynamics model, and a second test to investigate the performance of the method. When problems were detected, some of them could be corrected directly during the testing, while other problems led to knowledge about what to improve in the model.

### 3.1 Double lane-change track modelling

Initially, the track was modelled as an exact representation of Figure 1, with the global coordinates  $X$ , representing the length of the track, and  $Y$ , describing its width, the vehicle must then be constrained by Eq. 49.

$$\left\{ \begin{array}{ll} -\frac{A}{2}, & X < 25.5 \\ \frac{A}{2} + 1, & 25.5 \leq X \leq 36.5 \\ \frac{A}{2} - 3, & 36.5 < X \leq 61 \end{array} \right\} \leq Y \leq \left\{ \begin{array}{ll} \frac{A}{2}, & X \leq 12 \\ \frac{A}{2} + 1 + B, & 12 < X < 49 \\ \frac{A}{2}, & 49 \leq X \leq 61 \end{array} \right\} \quad \text{Eq. 49}$$

Constraints with discontinuous derivatives often need more iteration with a numerical solver compared to if they had continuous derivatives, and the problem may not be solved at all. To avoid this problem Eq. 1 was implemented in Eq. 49 around each of the abrupt changes with  $a_{tr} = 0.1$  to create a large curvature on each corner, see Figure 11. The new constraints to limit the car's movements are given by Eq. 50 and the rounded corners were placed so that the original corner point was still covered by the constraint.

$$\begin{aligned} \frac{1+A}{2} \left( 1 + \tanh \left( \frac{X - 25.2}{a_{tr}} \right) \right) - \frac{A}{2} + \frac{1+C}{2} \left( 1 - \tanh \left( \frac{X - 36.8}{a_{tr}} \right) \right) - 1 + C \\ \leq Y \leq \\ \frac{1+B}{2} \left( 1 + \tanh \left( \frac{X - 12.3}{a_{tr}} \right) \right) + \frac{A}{2} + \frac{1+B}{2} \left( 1 - \tanh \left( \frac{X - 48.7}{a_{tr}} \right) \right) - 1 - B \end{aligned} \quad \text{Eq. 50}$$

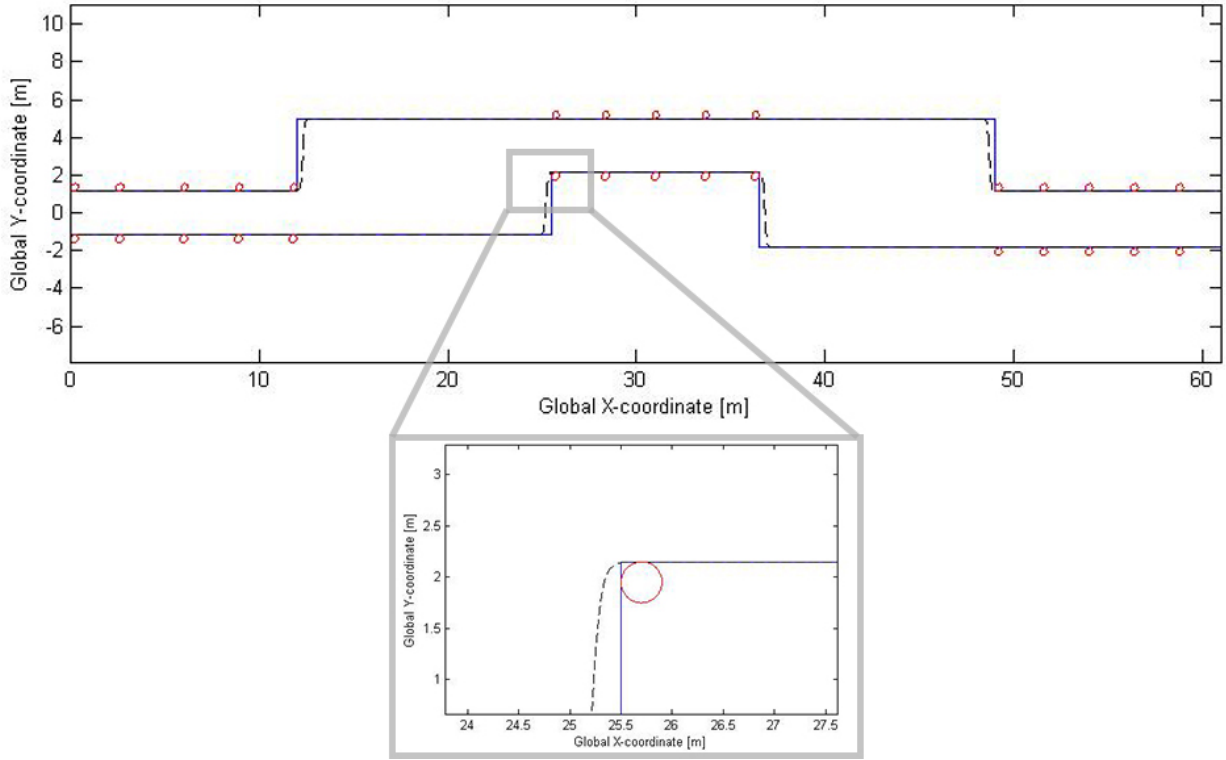


**Figure 11.** Real track boundaries are shown as solid lines, estimated boundaries as dashed lines with continuous derivatives and illustration of cone positions with circles. One of the corners has been magnified in the bottom of the figure to make the differences between the two types of boundaries more clear.

Figure 11 illustrates the difference between the two different types of constraints. The main parts are equal while the corners are different as well as two vertical constraints are within the track but at positions where the vehicle is not expected to drive when achieving its maximum entry speed.

### 3.2 Objective function

Section 1.3 describes that the objective was to maximize the entry speed; using Tomlab's [11] solver standard mode, that was the minimization of the cost function, one could set the cost function,  $J$ , according to

$$J = -V_x(X = 0) \quad \text{Eq. 51}$$

as

$$\max_{t=t_0} v_x = \min_{t=t_0} -v_x. \quad \text{Eq. 52}$$

The above objective function does not include the control variable, the steering angle, which implies that a solution may have bang-bang behaviour of the steering angles [46]. Such behaviour was not favourable but could be avoided by introducing a second part in the

objective, which grew larger when the steering angle rate became higher. From section 1.3 it occurs that the only objective should be the maximization of the entry speed, therefore a weighting factor for limiting the steering angle rate contribution to the result was also introduced. By doing a stepwise reduction of this weight factor,  $W_\delta$ , while the model got solved with more details, the most detailed model also got very little influence from the steering angle rate, thus the final objective used is given by Eq. 53.

$$J = -V_x(t=0) + W_\delta \int_{t=0}^{t=t_{final}} \dot{\delta}^2 \quad \text{Eq. 53}$$

In the first iteration, in the simplest model,  $W_\delta$  was set to 1.67 while it was set to just 0.05 in the most advanced model. If the first and second term in Eq. 53 are compared when  $W_\delta = 0.05$ , it can be seen that the influence from the second term is less than 1 %. A secondary weight factor can also be used for the first term to optimize  $J$  to be used with the numerical solver; in this case such a factor would just be set equal to 1.

### 3.3 Point mass trajectory and initial inputs

A simple guess, to the first optimization problem was crucial if it would be desired to easily change parameters and still have a solution which could converge without major changes to the input information. Therefore, the first optimization problem started from a guess of how much time,  $t_g$ , the run would need as well as how much the speed would drop in percentage of the entry speed,  $v_d$ , and the states of the vehicle were then estimated according to Eq. 54-Eq. 59.

$$X_g = \frac{61}{t_g} t \quad \text{Eq. 54}$$

$$Y_g = \frac{A+B+2}{4} \left( 1 + \tanh((X_g - 20) / a_g) \right) - \frac{B+C+2}{4} \left( 1 + \tanh((X_g - 43) / a_g) \right) \quad \text{Eq. 55}$$

$$v_{xg} = \frac{61}{t_g} \left( 1 + \frac{v_d}{100} \left( 1 - \frac{t}{t_g} \right) \right) \quad \text{Eq. 56}$$

$$v_{yg} = \frac{\dot{Y}_g}{3} \quad \text{Eq. 57}$$

$$\psi_g = \tan^{-1} \left( \frac{\dot{Y}_g}{\dot{X}_g} \right) \quad \text{Eq. 58}$$

$$\delta_g = \frac{\dot{\psi}_g}{2} \quad \text{Eq. 59}$$

Time,  $t$ , is continuous and present in all of the guess equations and it was found to be time efficient to provide a guessed total time,  $t_g$ , equal to 2.2 seconds as well as a speed decrease,  $v_d$ , of 15 %. Such a guess has a higher entry speed than was expected for the solution to find; the guessed position, yaw angle and speed can also be seen in Figure 12, Figure 13 and Figure 14 respectively.

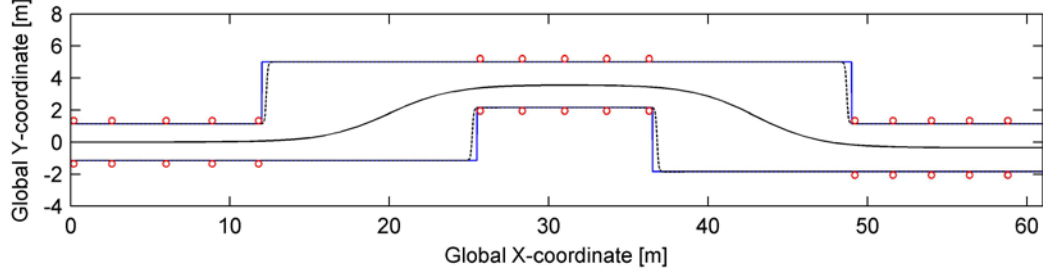


**Figure 12.** Guessed optimal position along the track.

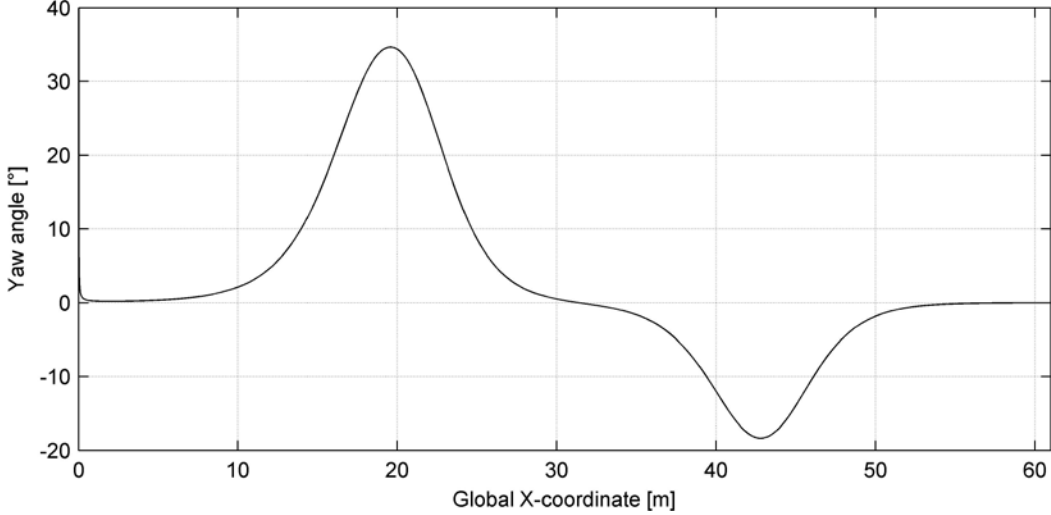


**Figure 13.** Guessed optimal yaw angle along the track.

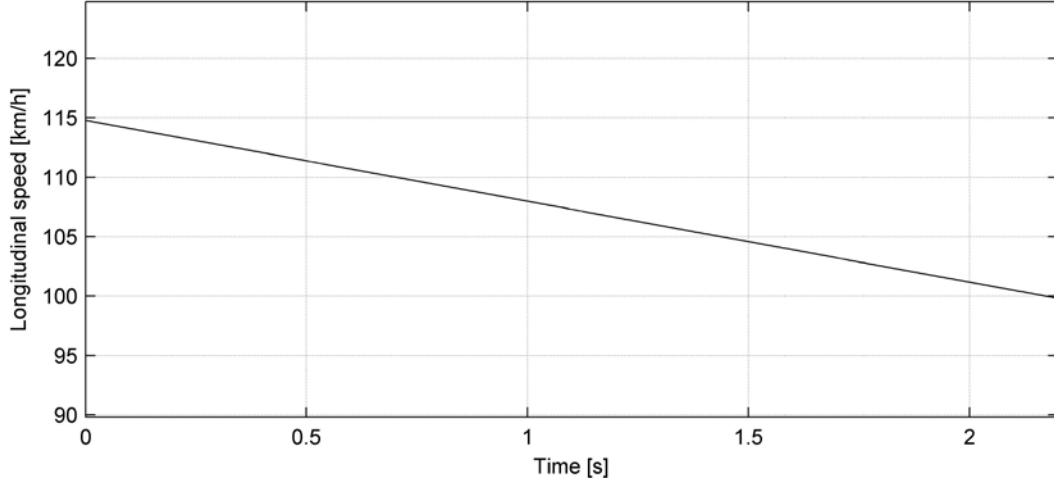


**Figure 14. Guessed longitudinal vehicle speed over time during the manoeuvre.**

The aforementioned guess was unrealistic but still provided information about the general pattern of the solution regarding the vehicle global coordinates, yaw angle and speed decrease over time.

### 3.4 Bicycle model trajectory optimization

Initially, the bicycle model, described in section 2.5, was used with a linear tire model, described in section 2.7.2. The results were used as a guess in a bicycle model with magic formula tire model as described in section 2.7.3. Specific details, such as the objective formulation and constraints, for the two models can be seen in the following sections.

#### 3.4.1 Linear tire model

As a first step, the bicycle model, shown in Figure 3, was studied. The side forces on the tires were calculated as linear functions of the slip angles and the cornering stiffness of the tires. In this step, no longitudinal forces were modelled.

Small angle approximations were used to keep this initial problem simple. This means that the steering angle  $\delta$  and the slip angles of the front and rear tire,  $\alpha_{12}$  and  $\alpha_{34}$  respectively, were considered to be small,  $\alpha_{12}, \alpha_{34} \ll 1$ . From Eq. 9 and Eq. 10 the slip angles were then given by

$$\alpha_{12} \approx \frac{v_y + f\dot{\psi}}{v_x} - \delta \quad \text{Eq. 60}$$

and

$$\alpha_{34} \approx \frac{v_y - b\dot{\psi}}{v_x}. \quad \text{Eq. 61}$$

As shown in section 2.5 the front and the right side force are then given by Eq. 62, Eq. 63 with the assumption to be linear functions of the slip angles.

$$F_{12} = -C_{12}\alpha_{12} \quad \text{Eq. 62}$$

$$F_{34} = -C_{34}\alpha_{34} \quad \text{Eq. 63}$$

The model was extended to incorporate air drag along the vehicle's longitudinal direction. With the extra term added, the equations of motion described by Eq. 2-Eq. 4 became:

$$m(\dot{v}_x - \dot{\psi}v_y) \approx -F_{12}\delta - \frac{1}{2} \rho \cdot A \cdot C_d \cdot V_x^2, \quad \text{Eq. 64}$$

$$m(\dot{v}_y + \dot{\psi}v_x) = F_{34} + F_{12} \cos(\delta) \approx F_{34} + F_{12} \quad \text{Eq. 65}$$

and

$$I_z\ddot{\psi} = fF_{12} \cos(\delta) - bF_{34} \approx fF_{12}\delta - bF_{34} \quad \text{Eq. 66}$$

with the term  $\frac{1}{2} \cdot \rho \cdot A \cdot C_d \cdot V_x^2$  representing the vehicle air drag [22] [23]. This air drag was also considered to be independent of the vehicle's sideslip angle. A solution was searched for the movement of the CoG position in the global coordinate system shown in Figure 3, thus Eq. 5 and Eq. 6 could be used.

An implementation of Eq. 60-Eq. 66 and the coordinate translation Eq. 5-Eq. 6 was programmed in TOMLAB and the solutions were constrained to be paths travelling inside the double lane change manoeuvre, as described in the ISO3888 Part 2 [2], according to Table 1. The state variables were  $v_x$ ,  $v_y$ ,  $\dot{\psi}$ <sup>9</sup>,  $\psi$ ,  $X$  and  $Y$  while the control variable was the steering angle,  $\delta$ , alone. This meant that during the manoeuvre the only way for the controller to control the vehicle was by changing the steering wheel angle, with no throttle, brakes, or engine braking at all.

---

<sup>9</sup> The choice of  $\dot{\psi}$  as a Tomlab state variable was done in order to avoid the double derivation of  $\psi$  required in Eq. 4, such that only a single derivation of the state  $\dot{\psi}$  was required instead. This was done since in Tomlab double derivations are advised against, and an inclusion of an additional state is preferred [16].

**Table 1. Constraints for the linear bicycle model. No vehicle dimensions in the model.**

Variable constraints	Description
$V_x \geq 10^{(i)}$	The car's longitudinal speed in m/s
$-20 \leq V_y \leq 20^{(i)}$	The car's lateral speed in m/s
$-\pi/2 \leq \psi \leq \pi/2^{(i)}$	Yaw angle in rad
$-4 \leq \dot{\psi} \leq 4^{(i)}$	Yaw rate in rad/s
$-31^\circ \leq \delta \leq 31^\circ$	Steering angle in degrees
$-4\pi \leq \dot{\delta}_{sw} \leq 4\pi^{(ii)}$	Steering wheel rate in rad/s
$X(t = 0) = 0^{(iii)}$	Initial longitudinal position of CoG in m
$X(t = t_{final}) = 61^{(iii)}$	Final longitudinal position of CoG in m
$width/2 - A/2 \leq Y(t = 0) \leq A/2 - width/2^{(iii)}$	Initial vertical position of the CoG in m
$width/2 + A/2 - C \leq Y(t = t_{final}) \leq A/2 - width/2^{(iii)}$	Final vertical position of the CoG in m
$\psi(t = 0) = 0^{(iv)}$	Initial yaw angle in rad
$\dot{\psi}(t = 0) = 0^{(iv)}$	Initial yaw rate in rad/s
$\delta(t = 0) = 0^{(iv)}$	Initial steering angle in rad
$V_y(t = 0) = 0^{(iv)}$	Initial lateral velocity in m/s
$C_f = \frac{BCD}{2} N_f^{(v)}$	Cornering stiffness on the front in N/rad
$C_r = \frac{BCD}{2} N_r^{(v)}$	Cornering stiffness on the rear in N/rad

(i) Constraints to help limit the search space. In order to help the optimizer converge to a solution this limitation should be neither too loose nor too strict [6].

(ii) Constraint that prevents the steering output from being faster than a human driver or steering robot [47]. This constraint was added to the model only after the first visit to Hällered test track took place. Initially, only the steering angle  $\delta$  was restricted, and the resulted steering rate, being unrestricted, was too high. As a result, the steering torque request from the steering robot was also too high and the robot could not perform the manoeuvre. In a later step, this restriction to the steering rate was posed.

(iii) Constraints that limit the vehicle movement outer boundaries.

(iv) Constraints that define the entrance of the vehicle to be in a straight driving manner.

(v) The values of the cornering stiffness for the front and rear tire were set to half of the magic formula stiffness, division by 2 was necessary in order not to produce unrealistic high forces with the linear model when performing a manoeuvre outside of the linear range. This facilitated the use of the result as a guess when the magic formula also got implemented.

Furthermore, the solution was done in two steps with  $n$  equals to 20 and 80 collocation points<sup>10</sup> respectively where the cost function was given by Eq. 53, and the weight factor,  $W_\delta$ , was set according to

$$W_\delta = \frac{3000}{90n} \quad \text{Eq. 67}$$

<sup>10</sup> Collocation points as used by the collocation method described in the Tomlab manual [6].

which implies its value was 1.67 during the first iteration and 0.04 for the result given by this model. The high initial value of the cost function weight factor,  $W_\delta$ , was selected as an arbitrary number. After the first iteration it was lowered in order to reduce its effect on the output without getting a bang-bang behaviour of the steering angle input.

### 3.4.2 Magic formula tire model

After the above linear model produced an optimal path the model was augmented by increasing the complexity, and thus the accuracy, of the equations of motion. While the linear tire model can describe lateral dynamics that involve accelerations of up to 40% of the road friction potential, that is up to  $4 \text{ m/s}^2$  or  $0.4 \text{ g}$  for dry road conditions, it is inadequate for higher lateral accelerations, which imposes the need for a non-linear model, since the manoeuvre that was studied was highly dynamical [24] [45]. The non-linear model that was used here was the Magic Formula tire model where the vehicle's tire forces were calculated by their slip, according to the simplified Magic Formula [28] as described in 2.7.3 Non-linear tire model and given by Eq. 23.

This simplified expression was chosen since the modelling in this study focused on the whole vehicle, rather than the tires alone, and thus it was considered that this version captured a satisfactory amount of information, which was reasonably detailed, yet simple enough for use in an optimization study like this. The resultant tire slip  $s$  for each tire was defined as

$$s_i = \sqrt{s_{ix}^2 + s_{iy}^2} \quad \text{Eq. 68}$$

with

$$s_{ix} = \frac{V_{ix} - \omega_i r_i}{\omega_i r_i}, \quad s_{iy} = \frac{V_{iy}}{\omega_i r_i} \quad \text{Eq. 69}$$

as the theoretical slip quantities [28].  $V_{ix}$  and  $V_{iy}$  are the tire frame components of the vehicle velocity vector at the centres of the wheels, such that  $s_{ix}$  and  $s_{iy}$  are the tire slips in the tire frame's x and y direction respectively. With the slip values calculated, the friction coefficients in the tire's x and y direction are defined as

$$\mu_{ix} = -\frac{s_{ix}}{s_i} \mu_i, \quad \mu_{iy} = -\frac{s_{iy}}{s_i} \mu_i. \quad \text{Eq. 70}$$

The normal forces at the tires,  $F_{fz}$  and  $F_{rz}$  for the front and rear tire respectively, was then obtained from

$$F_{fz} = \frac{mgb}{L} - \frac{mh}{L} a_x, \quad F_{rz} = \frac{mgf}{L} + \frac{mh}{L} a_x \quad \text{Eq. 71}$$

which resulted in the tire forces at each tire frame as

$$F_{ix} = \mu_{ix} F_{iz}, F_{iy} = \mu_{iy} F_{iz}. \quad \text{Eq. 72}$$

It is noteworthy that in this model also the longitudinal force, at the tire frame of each tire,  $F_{ix}$  was included, in contrast to the linear tire bicycle mode. The term  $\frac{mh}{L} a_x$  in Eq. 71 is the load transfer in the longitudinal direction, that is, between the front and the rear wheels. Load transfer occurs since the extended version of the bicycle model used here also included the height of the CoG. Therefore, when the vehicle accelerates, the normal force on the front will become lower as the term  $\frac{mh}{L} a_x$ , introduced by the acceleration, is subtracted from its static load, while the normal force on the rear will become larger since this load will be now be added to its static load value. The ODE's describing this model and the global velocities of the CoG were then formulated by Eq. 5, Eq. 6, Eq. 19 and Eq. 64-Eq. 66; with indices corresponding to this model they are given by

$$m(v_x - \dot{\psi} v_y) = F_{fx} \cos \delta - F_{fy} \sin \delta + F_{rx} - \frac{1}{2} \rho \cdot A \cdot C_d \cdot V_x^2, \quad \text{Eq. 73}$$

$$m(v_y + \dot{\psi} v_x) = F_{ry} + F_{fx} \sin \delta + F_{fy} \cos \delta, \quad \text{Eq. 74}$$

$$I_z \ddot{\psi} = f(F_{fy} \cos \delta + F_{fx} \sin \delta) - b F_{ry}, \quad \text{Eq. 75}$$

$$I_w \dot{\omega}_f = T_f - F_{fx} r, \quad \text{Eq. 76}$$

$$I_w \dot{\omega}_r = T_r - F_{rx} r, \quad \text{Eq. 77}$$

$$\dot{X} = v_x \cos(\psi) - v_y \sin(\psi) \quad \text{Eq. 78}$$

$$\dot{Y} = v_x \sin(\psi) + v_y \cos(\psi) \quad \text{Eq. 79}$$

where  $m$  is the vehicle's mass,  $I_z$  its moment of inertia around the vertical axis (yaw inertia),  $I_w$  the moment of inertia of each wheel and  $T_f, T_r$  the applied torque in the forward movement direction on the front and rear wheel respectively<sup>11</sup> [28] [22]. As shown in Eq. 76

---

<sup>11</sup> The drive/brake torques are considered as zero in this case, but will be used later where the ESC implementation will also be included in the model.

and Eq. 77, in addition to the nonlinear tire model, the wheel rotation dynamics were also introduced in this step.

Eq. 23 and Eq. 68-Eq. 72 were used to calculate the relevant slips and forces and Eq. 73-Eq. 79 were inserted in the TOMLAB solver as the model's ODEs. The constraints used for the state and control variables for this problem are shown in Table 2.

**Table 2. Constraints for the nonlinear bicycle model.**

Variable constraints	Description
$V_x \geq 10^{(i)}$	The car's longitudinal speed in m/s
$-20 \leq V_y \leq 20^{(i)}$	The car's lateral speed in m/s
$-\pi/2 \leq \psi \leq \pi/2^{(i)}$	Yaw angle in rad
$-4 \leq \dot{\psi} \leq 4^{(i)}$	Yaw rate in rad/s
$-31^\circ \leq \delta \leq 31^\circ$	Steering angle in degrees
$-4\pi \leq \dot{\delta}_{sw} \leq 4\pi^{(ii)}$	Steering wheel rate in rad/s
$X(t = 0) = 0^{(iii)}$	Initial longitudinal position of the CoG in m
$X(t = t_{final}) = 61^{(iii)}$	Final longitudinal position of the CoG in m
$width/2 - A/2 \leq Y(t = 0) \leq A/2 - width/2^{(iii)}$	Initial vertical position of the CoG in m
$width/2 + A/2 - C \leq Y(t = t_{final}) \leq A/2 - width/2^{(iii)}$	Final vertical position of the CoG in m
$\psi(t = 0) = 0^{(iv)}$	Initial yaw angle in rad
$\dot{\psi}(t = 0) = 0^{(iv)}$	Initial yaw rate in rad/s
$\delta(t = 0) = 0^{(iv)}$	Initial steering angle in rad
$V_y(t = 0) = 0^{(iv)}$	Initial lateral velocity in m/s
$10/r \leq \omega_f \leq 180/r^{(i)}$	The front wheel's rotational speed in rad/s
$10/r \leq \omega_r \leq 180/r^{(i)}$	The rear wheel's rotational speed in rad/s
$\omega_f \cdot r \leq 1.2 \cdot V_x^{(i)}$	Indirect limitation on front wheel slip
$\omega_r \cdot r \leq 1.2 \cdot V_x^{(i)}$	Indirect limitation on rear wheel slip

(i) Constraints to help limit the search space. In order to help the optimizer converge to a solution this limitation should be neither too loose nor too strict [6].

(ii) Constraint that prevents the steering output from being faster than a human driver or steering robot [47]. This constraint was added to the model only after the first visit to Hällered test track took place. Initially, only the steering angle  $\delta$  was restricted, and the resulted steering rate, being unrestricted, was too high. As a result, the steering torque request from the steering robot was also too high and the robot could not perform the manoeuvre. In a later step, this restriction to the steering rate was posed.

(iii) Constraints that limit the vehicle movement into some specific boundaries dictated by the manoeuvre.

(iv) Constraints that define the entrance of the vehicle to be in a straight driving manner.

The cost function was the same as in the linear tire bicycle model, given by Eq. 53, but with the weight factor,  $W_\delta = 0.0521$ , which is slightly higher than the value used for the start

guess' last iteration. Once again an iterative solution strategy with increasing collocation points; 20, 30, 35, 40, and 80 collocation points were used. A long iterative procedure was used in this case, as the guess was the result from the linear solution, thus the solution was expected to change for all states.

### 3.5 Car body boundary modelling

While the dimensionless car model moves along the track the global position of all points on the car body can be calculated from the information about its CoG position, the yaw angle and the points' coordinates in the car's local coordinate system. The numerical solver cannot check an infinite number of points on the car body boundary, which means the boundary has to be discretized into a few points which then represent the whole car body. As the corners of the car body are describing the car body extension, those were selected as the first points. The right and left side of the car could still hit a corner when turning, posing an additional problem, which was solved by describing the sides of the car with eight points each; the number of points needed will depend on the yaw rate, the length of the car and how sharp the corner is.

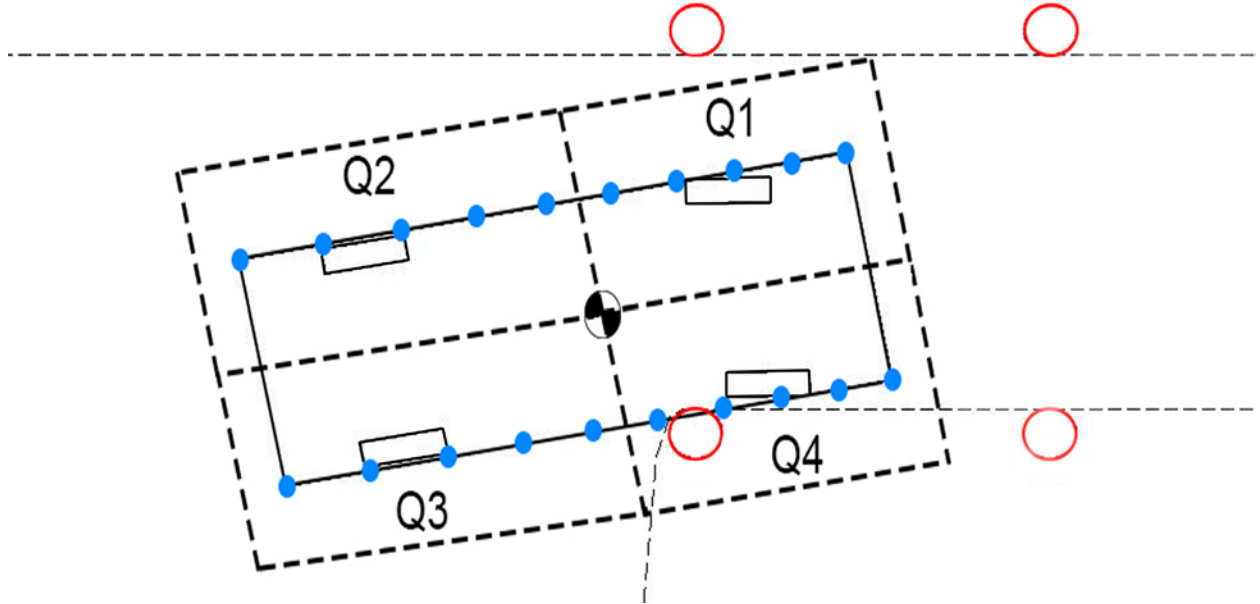


**Figure 15.** Illustration of the discretized car travelling from left to right. Each filled circle is a discrete point, and a corner is passing through the car body without violating any discrete point. It is also shown how the car is divided into the four quadrants Q1, Q2, Q3 and Q4.

The situation in Figure 15 can exist if the yaw rate is high enough to place the car away from the corner before the next discrete point reaches it, and therefore it is important to check if that is the case after the solution has been found. In section 3.10 a visual verification method is described which gives an indication of whether the car hit the corner or not.

Each discrete point on the left side of the car was given the constraints to not cross the left side of the track, corresponding to the left side of Eq. 50, while each point on the right side of the car was given the constraints to not cross the right side of the track, corresponding to the right side of Eq. 50. It was possible to use one side of Eq. 50 at a time since the points also are constrained to each other and Eq. 50 then must be fulfilled if the points do not cross the boundary on their own side of the car. It would be possible to manually specify the constraints for each point but then it would also be necessary to redo that process for cars with different sizes; instead the car was divided into four quadrants according to Figure 15. Each quadrant contains evenly spaced discrete points which are generated with each corner as base and a number specifying the number of the points that should be used. This method makes it possible to create a model, which decides how many points should be used based on the dimensions of the car.

### 3.6 Four wheel vehicle model trajectory optimization

In Figure 16 a vehicle model known as the two track model is shown. This is the vehicle model that was used for this study as a basis for drawing some first conclusions, and is also studied in [28] [48] [47] [22]. It is an actual extension of the bicycle model, in order to differentiate between the left and right wheels of the vehicle, and allows the vehicle's movement to be described in a more detailed manner. This model was the one that produced the first results to test and compare with a real vehicle in a test track, with no ESC activated yet.

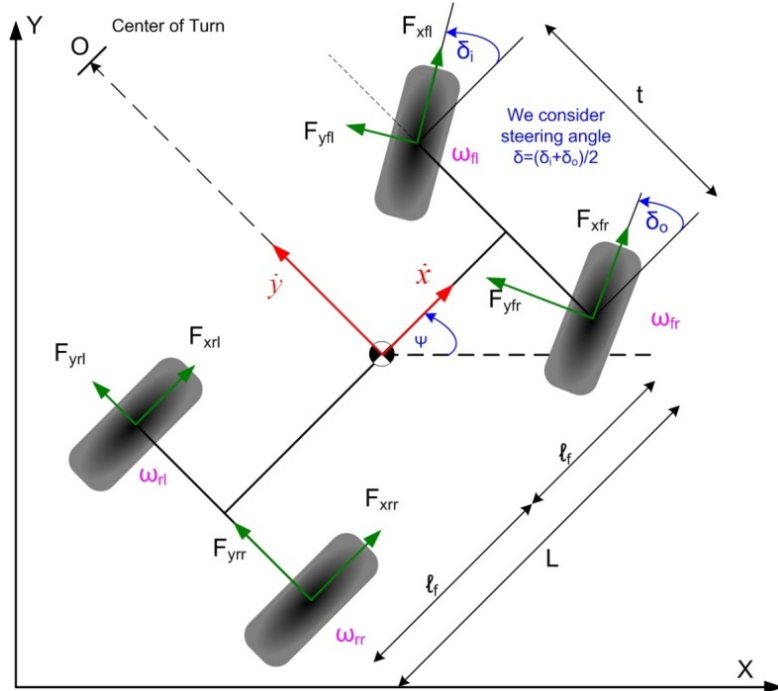


Figure 16. Illustration of the four wheel vehicle model with notation [25].

As depicted in Figure 16, during a turn, the inner and outer wheels steer by a different angle,  $\delta_i$  and  $\delta_o$  respectively, since the outer wheel is required to travel at a longer path (lower curvature) than the inner one<sup>12</sup>. This applies to actual vehicles. During this study though, a common simplification was followed and the steering angle  $\delta$  was considered to be the same for both of the wheels and equal to their mean value, that is [22]

$$\delta = \frac{\delta_i + \delta_o}{2} \quad \text{Eq. 80}$$

The details that were modelled and were possible to use in the two track model, are described in section 3.8. The equations used for this case are presented in 3.8.4 Fully featured model without ESC.

### 3.7 ESC modelling

As Appendix A – ISO 3888 description involves releasing the throttle before the first turn when entering the double-lane change track, as seen in Figure 1, the ESC can only choose to brake each wheel or change the steering angle of the front wheels, no extra torque can be transferred to any wheel. However, in this study it was only the brakes which were considered to be a part of the ESC as the steering angle input was optimized no matter if the ESC was used or not.

Four types of ESC systems will be described below, of which the three first are slip angle controlled ESC, yaw rate error controlled ESC as well as a combined slip angle error and yaw rate error controlled ESC. An optimal controller, for the studied scenario, has also been defined and modelled to be used as a reference; by definition it should outperform any ESC implementation.

By using a threshold for activating the system and a logic for determining which wheel to brake the ESC system got described by discontinuous functions, which is not recommended to be used within the Tomlab solver. Such discontinuous functions behave according to Eq. 81; they were approximated by using Eq. 1 as shown in Eq. 82.

$$\begin{aligned} O < Q &\rightarrow P = 0 \\ O \geq Q &\rightarrow P = 1 \end{aligned} \quad \text{Eq. 81}$$

$$P = \frac{1}{2} \left( 1 + \tanh \left( \frac{O - Q}{a} \right) \right) \quad \text{Eq. 82}$$

---

<sup>12</sup> For cars operating in low speed and lateral acceleration conditions (street cars) usage of Ackermann geometry is most commonly the case. With this design the wheels are traveling along concentric paths, and that ensures that all the wheels roll freely with no slip angles. In vehicles designed for other purposes, like for example racing, other steering geometries apply [12][18].

In Eq. 82  $a$  is a constant determining how small the transition region from the lower to the higher value of the curve is, in which the equation does not behave as Eq. 81, as illustrated in Figure 17 below.

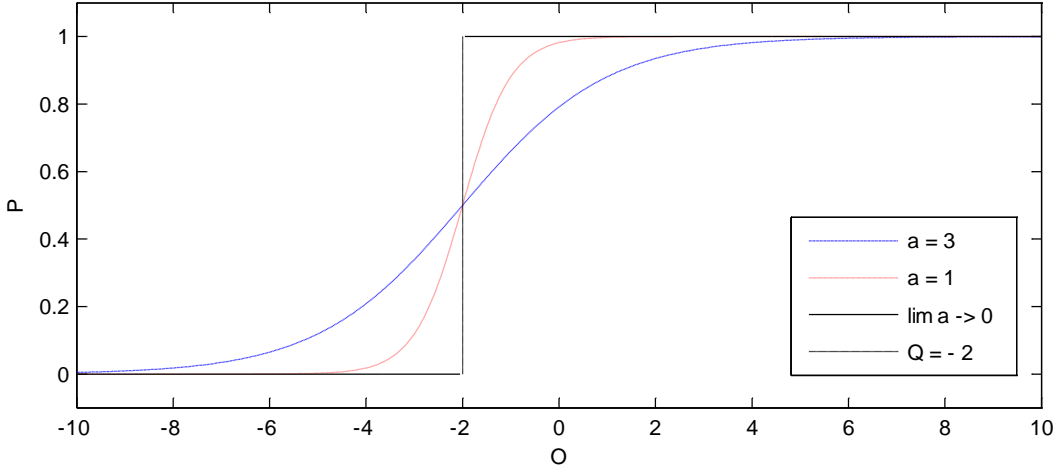


**Figure 17. Illustration of Eq. 82 for different values of  $a$ . When  $a$  approaches zero the resulting value of  $P$  approaches the value which is given by Eq. 81.**

The value of  $a$  in Eq. 82 should always be much smaller than the output value,  $C$ , of the equation but always greater than zero.

### 3.7.1 Optimal ESC modelling – a torque controller

Optimality in this case means everything that results in a higher entry speed without hitting any cone when driving through the track. For an ESC this results in controlling exactly how much braking torque should be applied on each wheel at all times. This was implemented in the optimal controller by adding a torque control variable to each wheel's equations of motion with the only restriction that the variable had to be negative. The tire-road friction limit serves as the upper bound for how much braking torque can be applied, resulting in maximum utilization of friction forces.

As it was desired to know how well an ESC could perform, and use that knowledge when creating another type of ESC, two versions of the torque model were modelled with different limitations.

- Optimal braking torque applied only after the vehicle reached the first turn
- Optimal braking torque applied only if a threshold was reached, e.g. yaw rate error or slip angle error. The torque rate was then limited to one rate for pressure build up and another rate for releasing the brakes.

The first of these limited optimal torque models was just intended to avoid braking during the initial straight path while the second one should determine how well an optimal ESC with a certain threshold would perform. The second limited model then could be used as a reference, and an upper limit, for any ESC-model as long as the same threshold was used.

### 3.7.2 Sideslip angle controlled ESC

When using the Tomlab [11] optimization environment it was not recommended by the solver instructions to use discontinuous functions (although it was allowed). As the test vehicle<sup>13</sup> had an ESC with discontinuous behaviour, a simple ESC, but with discontinuous behaviour, was implemented to study its robustness.

Control of when to activate each brake was done by only activating the ESC after the magnitude of the sideslip angle, which was defined as

$$\beta = \tan^{-1} \left( \frac{v_y}{v_x} \right), \quad \text{Eq. 83}$$

was higher than a certain level – the case of a 2 ° threshold,  $\beta_{th}$ , was investigated in this study.

When the ESC had been activated, braking torque was applied to the right front wheel when oversteering to the left, to the left front wheel when oversteering to the right, to the right rear wheel when understeering right and to the left rear wheel when understeering to the left. Whether the vehicle understeered or not was determined by calculating the understeer gradient,  $K_{us}$ , according to [22]

$$K_{us} = \frac{\left( \delta - \frac{L}{R} \right)}{a_y} \quad \text{Eq. 84}$$

where R is given by

$$R = \frac{\sqrt{v_x^2 + v_y^2}}{|\dot{\psi}|}. \quad \text{Eq. 85}$$

Table 3 shows the  $\text{SlipESC}_{ij}$  value for each wheel during each of the above described situations. If  $\beta < \beta_{th}$  then  $\text{SlipESC}_{ij}$  was always set to 0.

---

<sup>13</sup> The test vehicle was a Volvo S60 with specifications according to Appendix B.

**Table 3. Binary logic of the sideslip controlled ESC.**

	Oversteer		Understeer	
	$K_{us} < 0, \delta > 0$	$K_{us} < 0, \delta < 0$	$K_{us} > 0, \delta > 0$	$K_{us} > 0, \delta < 0$
SlipESC <sub>fr</sub>	1	0	0	0
SlipESC <sub>fl</sub>	0	1	0	0
SlipESC <sub>rl</sub>	0	0	1	0
SlipESC <sub>rr</sub>	0	0	0	1

The magnitude of the torque was then set to increase proportionally with the slip angle, which resulted in two selectable variables for this type of ESC; the slip angle threshold and the proportional constant between the braking torque and the slip angle. The proportional constant could even be different for each wheel but in this study the ESC was activated over a slip angle magnitude of 2 ° and with each wheel torque,  $T_{fr}$ ,  $T_{fl}$ ,  $T_{rr}$  and  $T_{rl}$ , according to

$$T_{ij} = 5000(\beta - \beta_{th})\text{SlipESC}_{ij} \quad \text{Eq. 86}$$

Note that if both the slip angle threshold and proportional constants for the braking torque at each wheel are set to be control variables within the optimization, this method becomes equal with the optimal torque control method.

### 3.7.3 Yaw rate error controlled ESC

Control of when to activate each brake was done by only activating the ESC after the magnitude of the yaw rate error was higher than a certain level. A desired yaw rate was calculated with Eq. 33, which describes the vehicle's steady state yaw rate.

The actual yaw rate was a part of the solution of the states, thus it was possible to use directly without any extra calculations. It was then compared to the desired yaw rate and the error was defined as the difference between them,

$$\dot{\psi}_e = \dot{\psi} - \dot{\psi}_d \quad \text{Eq. 87}$$

When the yaw rate error was obtained, it was possible to know when the ESC should be activated, but a logic braking scheme is also needed for which wheel should brake.

The following four scenarios describe the situation when each wheel needs to brake:

- **Brake rear left wheel  $ESC_{rl}$** (understeer): Positive desired yaw rate, a left turn, but negative yaw rate error – the vehicle does not turn left as much as desired.
- **Brake rear right wheel  $ESC_{rr}$** (understeer): Negative desired yaw rate, a right turn, and positive yaw rate error – the vehicle does not turn right as much as desired.
- **Brake front left wheel  $ESC_{fl}$** (oversteer): Negative desired yaw rate, a right turn, and negative yaw rate error – the vehicle turns right more than desired.
- **Brake front right wheel  $ESC_{fr}$** (oversteer): Positive desired yaw rate, a left turn, and positive yaw rate error – the vehicle turns left more than desired.

The logic described above was implemented using continuous functions according to Eq. 82; thus the resulting logic is described by

$$ESC_{rl} = \frac{1}{4} \left( 1 + \tanh \left( \frac{-\dot{\psi}_e}{a} \right) \right) \left( 1 + \tanh \left( \frac{\dot{\psi}_d}{a} \right) \right), \quad \text{Eq. 88}$$

$$ESC_{rr} = \frac{1}{4} \left( 1 + \tanh \left( \frac{\dot{\psi}_e}{a} \right) \right) \left( 1 + \tanh \left( \frac{-\dot{\psi}_d}{a} \right) \right), \quad \text{Eq. 89}$$

$$ESC_{fl} = \frac{1}{4} \left( 1 + \tanh \left( \frac{-\dot{\psi}_e}{a} \right) \right) \left( 1 + \tanh \left( \frac{-\dot{\psi}_d}{a} \right) \right), \quad \text{Eq. 90}$$

and

$$ESC_{fr} = \frac{1}{4} \left( 1 + \tanh \left( \frac{\dot{\psi}_e}{a} \right) \right) \left( 1 + \tanh \left( \frac{\dot{\psi}_d}{a} \right) \right). \quad \text{Eq. 91}$$

When the logic scheme given by Eq. 88-Eq. 91 determined which wheel should brake, the approach was to apply a braking torque as function of the yaw rate error as long as the error is larger than the threshold,  $\dot{\psi}_t$ . By formulating the threshold according to Eq. 82 and multiplying it with the desired initial braking torque,  $T_{init}$ , as well as a linear increase as function of the yaw rate error, the ESC behaviour could be adapted while always being continuous. The torque for the rear left wheel,  $T_{rl}$ , the rear right wheel,  $T_{rr}$ , the front left wheel,  $T_{fl}$ , and the front right wheel,  $T_{fr}$ , is then given by

$$T_{ij} = ESC_{ij} \left( -\frac{T_{init}}{2} \left( 1 + \tanh \left( \frac{\dot{\psi}_e - \dot{\psi}_t}{a} \right) \right) \left( 1 + T_{if}(\dot{\psi}_e - \dot{\psi}_t) \right) \right. \\ \left. - \frac{T_{init}}{2} \left( 1 + \tanh \left( \frac{\dot{\psi}_e + \dot{\psi}_t}{a} \right) \right) \left( 1 - T_{if}(\dot{\psi}_e + \dot{\psi}_t) \right) \right) \quad \text{Eq. 92}$$

The substantial torque increase,  $T_{init}$ , at the yaw rate error threshold as well as the increase factor,  $T_{if}$ , for the torque relative to its value at the threshold, could, in the ESC torque model, Eq. 92, be arbitrary positive numbers.

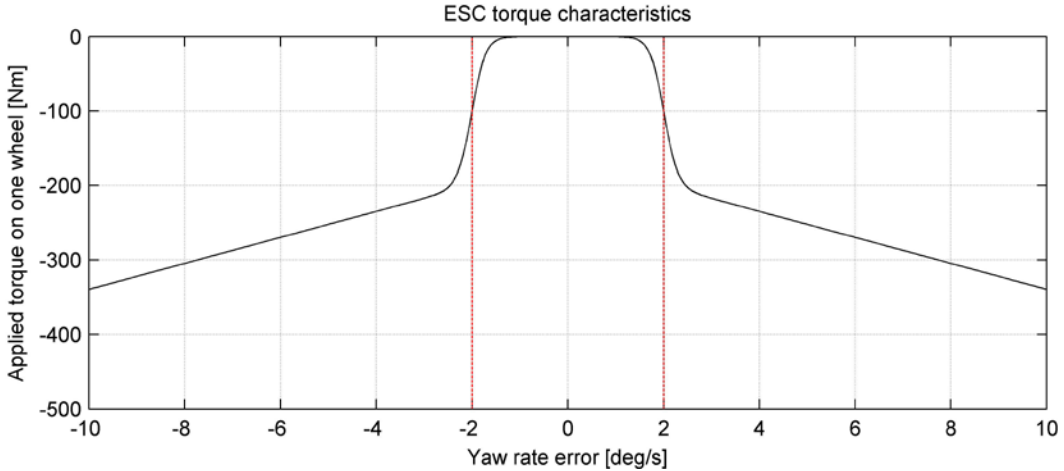


**Figure 18. ESC torque characteristics; scheme for the magnitude of the braking torque applied on one of the wheels for a given yaw rate error, which here is shown as vertical dashed lines. In this case the figure show a yaw rate error of 2°, an initial torque of 200 Nm, a torque increase factor of 5 and a smoothness factor of 0.005.**

The ESC torque characteristics shown in Figure 18 was seen to be one of the characteristic setups which was producing the highest entry speed and was used in all comparisons with an ESC except for in the ESC characteristic parameter study.

### 3.7.4 Yaw and slip controlled ESC

All solutions without any ESC suggested that the steering angle was not small and hence it was not possible to use the simplified equation, Eq. 39, to determine how much yaw torque the brakes needed to generate. Instead Eq. 18 was used without simplification in Eq. 36 and with  $\dot{s} = -\eta s$ . When the contact forces between the road and tire were rearranged to the left hand side, Eq. 93 was obtained.

$$\begin{aligned}
& -l_f(F_{xfl} + F_{xfr}) \sin(\delta) - l_f(F_{yfl} + F_{yfr}) \cos(\delta) \\
& + l_r(F_{yrl} + F_{yrr}) - \frac{l_{wf}}{2}(F_{xfr} - F_{xfl}) \cos(\delta) \\
& - \frac{l_{wr}}{2}(F_{xrr} - F_{xrl}) - \frac{l_{wf}}{2}(F_{yfl} - F_{yfr}) \sin(\delta) \\
& = \eta s I_z - \ddot{\Psi}_d + \xi(\dot{\beta} - \dot{\beta}_d)
\end{aligned} \tag{Eq. 93}$$

As the numerical solver in Tomlab [11] solves the problem in all points along the track at once Eq. 93 can now be a part of the iterative procedure. The solution to each wheel's dynamic equation, Eq. 19, then also contains the torque needed and as no propulsion is allowed during the manoeuvre the torque was limited to never be positive. But fulfilling Eq. 93 by only controlling the steering wheel angle in such a way  $\dot{s} = -\eta s$  became an optimization problem itself, thus not suitable to use in another optimization problem.

The yaw rate error and the slip angle error, which is part of the sliding surface  $s$ , can still be used to control the ESC if the relation to the braking torque,  $T_{ij}$ , is a function of the form

$$T_{ij} = f(\dot{\psi}, \dot{\psi}_e, \beta, \beta_e) \tag{Eq. 94}$$

as the braking torque then does not introduce another optimization problem. A threshold for the activation of the ESC could be placed on the sliding surface  $s$ . This type of ESC is however not covered by this study.

### 3.8 Model refinement

It is almost impossible to provide a guess that is close to the solution for many different choices of parameters if the model has all of its modelling features implemented at once, hence the need of a stepwise refinement of it. The following modelling features and their corresponding implementation is depicted in this chapter:

1. Wheel kinematics and compliance
2. Tire relaxation
3. Wheel camber effects

#### 3.8.1 Wheel kinematics and compliance

A phenomenon modelled is the change of the toe angle due to two important factors: body roll and lateral force application on the wheels. The first case is termed “roll steer,” which is a change in the wheel angle that results from body roll motion<sup>14</sup>, and the second one is the

---

<sup>14</sup> Even though this is undesirable, it is a very common characteristic of most of the suspension and steering systems, which depends on their geometry [17] [22].

lateral force compliance steer, which is a change in the wheel angle due to compliance of the suspension by lateral forces applied at the tire-road contact [24] [31] [19] [21].

### *Roll steer*

From the Kinematics and Compliance (K&C) datasheet for the Volvo S60, more specifically from the “Toe-in angle at double side roll movement” test case, the values in the following Table 4 were extracted. The values are the ratio of the induced toe-in angle over the corresponding roll angle, and would be translated to what is commonly called *roll steer coefficient*  $\frac{\partial \delta}{\partial \varphi}$ , such that the steering angle  $\delta$  was described as a function of roll angle  $\varphi$  [19]. The roll angle was positive when the vehicle was leaning to the right as seen from behind (i.e. the right side is at jounce while the left at rebound). [Appendix G – Kinematics & compliance]

**Table 4.** Toe-in versus roll angle,  $\frac{\partial(\text{ToeIn})}{\partial \varphi}$  [deg/deg] for the Volvo S60.

	Left wheel	Right wheel
Front axle	+0.14	-0.11
Rear axle	+0.00	-0.01

The values above depict that during cornering the front wheels steer outwards with respect to the curve. In other words, the wheels toe out when compressed and toe in when expanded. For example, in a left turn the roll angle is positive. According to Table 4 then the front left wheel (in rebound) will toe in and the front right wheel (in jounce) will toe out. The rear wheels have negligible roll steer.<sup>15</sup> For the front axle, a *negative* roll steer coefficient then applies, and results in an understeer effect. When occurring on the rear axle an oversteer effect would occur [31] [19]. If the toe-in angle of each wheel is translated to steer angle  $\delta$  according to ISO standard [19], Table 4 is equivalent to Table 5 below.

**Table 5.** Roll steer coefficients,  $\frac{\partial \delta}{\partial \varphi}$  [deg/deg] for the Volvo S60.

	Left wheel	Right wheel
Front axle	-0.135	-0.111
Rear axle	-0.00	-0.01

---

<sup>15</sup> This result came from the interpretation of the S60 K&C datasheet that can be found in the Appendix G. According to Volvo Cars’ Vehicle Dynamics engineer Johan Hultqvist: ‘In most passenger cars a roll steer understeer effect is desired. This means that the front wheels will tend to steer outwards with respect to the curve. The rear wheels are usually neutral, the change in toe is negligible, but in some cars they can be designed to give roll steer understeer too – that would mean that the rear wheels tend to steer inwards with respect to the curve. In this case, we see some very low values for the rear axle but the measurement is obviously very noisy. From the shape of the curve we can assume a neutral rear axle behaviour.’

With roll steer oversteer tuning we can achieve some better “turn in” to the curve, but the vehicle might be unstable to higher speeds and the driver has to make corrections, so it is generally undesirable.”

The different sign for the case of the left wheels results from the fact that the steering angle  $\delta$  is positive in the opposite direction towards which the left wheel toes in. The opposite is true for the right wheels, so the signs for the right wheels are the same between Table 4 and Table 5.

Since the steering angle was considered the same for the left and right wheels, as mentioned in Eq. 80, a common roll steer coefficient can be used for the left and rear wheels at each axle. This value was the mean value of the right and left wheel roll steer coefficient. This means that for the front axle the value to be used would be

$$\left. \frac{\partial \delta}{\partial \varphi} \right|_{front} = \frac{-0.135 + (-0.111)}{2} = -0.123 \quad \text{Eq. 95}$$

adding an understeer effect, and for the rear axle

$$\left. \frac{\partial \delta}{\partial \varphi} \right|_{rear} \approx 0 \quad \text{Eq. 96}$$

The rear axle was considered to have a neutral behaviour to roll movement.

Modelled in this study was roll steer kinematics rather than roll steer dynamics, since the change to the steering angle as a function to roll angle was not inserted in a differential equation form, but rather as a steady state calculation (i.e. the change to steer angle induced by roll occurs instantaneously rather than gradually). In reality though, roll steer effects lag the steer input, appearing after the sprung mass has begun rolling [31]. The respective equations that were used in the model was

$$\delta_{rsf} = \left. \frac{\partial \delta}{\partial \varphi} \right|_{front} \cdot \varphi \quad \text{Eq. 97}$$

and

$$\delta_{rsr} = \left. \frac{\partial \delta}{\partial \varphi} \right|_{rear} \cdot \varphi \quad \text{Eq. 98}$$

for the change in the steering angle due to roll steer on the front and rear wheel respectively. The second equation, the roll steer at the rear wheels, could be regarded here as trivial, since the roll steer coefficient of the rear axle was zero as mentioned above. But for consistency and generality purposes it was inserted in the model nonetheless.

### *Lateral force compliance steer*

For modelling the lateral force compliance steer two test cases from the K&C datasheet were studied. The first one is the “*Toe-in angle at lateral force, unidirectional LH RH, at X = 0 mm*” case, which implies the change in the toe-in angle of a wheel when a lateral force is applied to

it at the centre of its contact patch with the ground ( $X = 0$ ). The second one is the “*Toe-in angle at lateral force, unidirectional LH RH, at  $X = 30 \text{ mm}$* ” case, which implies the change in the toe-in angle of a wheel when a lateral force is applied at a distance of  $X = 30 \text{ mm}$  behind<sup>16</sup> the centre of the tire-ground contact patch [Appendix G – Kinematics & compliance]. The distance  $X = 30\text{mm}$  behind the centre of the contact patch is an approximate value for a typical tire’s pneumatic trail in low slip angles [32]. Table 6 and Table 7 show extracted toe-in angle values.

**Table 6. Toe-in angle for positive lateral force applied at  $X= 0\text{mm}$   $\frac{\partial(\text{ToeIn})}{\partial F}$  [deg/kN].**

	Left wheel	Right wheel
Front axle	-0.029	-0.046
Rear axle	+0.07	+0.065

**Table 7. Toe-in angle for positive lateral force applied at  $X= 30\text{mm}$   $\frac{\partial(\text{ToeIn})}{\partial F}$  [deg/kN].**

	Left wheel	Right wheel
Front axle	-0.108	-0.143
Rear axle	+0.016	+0.018

The values in Table 6 and Table 7 refer to the change in a wheel’s toe-in angle with respect to the force acting on a given point on it, but they also describe the change in the steering angle for that given force. This time, no sign change was needed in order to match the wheel toe-in with the positive direction of the wheel steer (like in the case of the roll steer). The reason for that is the direction towards which the force was applied for each wheel when the measurement was taken. In the K&C tests a positive force indicates a force acting inwards to the wheel, and this means that while a positive toe-in angle at the left wheels translates to a negative respective steering angle, a positive force to the left wheels also translates to a negative force in the coordinate system that was used (where a lateral force is positive when it acts toward the direction of a positive abscissa – positive y axis), which means that for the left wheels

$$\left. \frac{\partial(\text{ToeIn})}{\partial F} \right|_{K\&C \text{ coord.}} = \left. \frac{\partial \delta}{\partial F} \right|_{\text{vehicle body coord.}} . \quad \text{Eq. 99}$$

Following the same argumentation it results to that the signs for the right wheels also needed no modification. The reason that these two sets of values were extracted from the K&C datasheet is the dynamic change of the pneumatic trail which results in a non-constant lateral force compliance steer coefficient. For small slip angles/linear tire region the pneumatic trail

<sup>16</sup> The word *behind* here indicates the direction that is opposite to the tire’s longitudinal travelling direction at the tire frame’s coordinate system.

is almost constant. But in larger slip angles/nonlinear tire region the pneumatic trail reduces (see also section for pneumatic trail in section 2.7.5) [23] [24] [32] [26]. The change in the toe-in angle of a wheel depends on the distance from its contact patch centre where the lateral force will be applied, which is the pneumatic trail, as Table 6 and Table 7 also indicate. The change in this lateral force compliance steer coefficient was approximated by linearly interpolating between its values for  $X = 0$  mm (nonlinear region pneumatic trail) and  $X = 30$  mm (linear region pneumatic trail). For example, the straight line between the lateral force compliance coefficients at  $X = 0$  mm and  $X = 30$  mm for the front left wheel would be

$$LF_{cfl} = \frac{0.029 - 0.108}{0.03} * t_{pfl} - 0.029 = -2.633 * t_{pfl} - 0.029 . \quad \text{Eq. 100}$$

and in a similar manner Table 8 was obtained.

**Table 8. Lateral force compliance steer coefficient as a function of the pneumatic trail when linearly interpolating between the K&C values [deg/kN].**  $LF_{cij}$  = lateral force compliance steer coefficient for the  $i,j$  wheel ( $i = f,r$ ,  $j = l,r$ ).  $t_{pij}$  = pneumatic trail for the  $i,j$  wheel.

	Left wheel	Right wheel
Front axle	$LF_{cfl} = -2.633 * t_{pfl} - 0.029$	$LF_{cfr} = -3.233 * t_{pfr} - 0.046$
Rear axle	$LF_{crl} = -1.8 * t_{prl} + 0.07$	$LF_{crr} = -1.5667 * t_{prr} + 0.065$

The change in the steering angle due to a lateral force could then be calculated as

$$\delta_{cij} = LF_{cij} * F_{ijy} . \quad \text{Eq. 101}$$

where  $F_{ijy}$  is the applied lateral force to the respective wheel. Again, as mentioned above, a mean induced steering angle due to lateral force compliance steer was used since the model did not include the difference in the right and left wheel steering angles but rather their mean value. This yields

$$\delta_{cf} = \frac{\delta_{cfl} + \delta_{cfr}}{2} , \quad \delta_{cr} = \frac{\delta_{crl} + \delta_{crr}}{2} \quad \text{Eq. 102}$$

for the induced steering angles on the front and rear axle. The tire's pneumatic trail also needed to be calculated at each instant, since this double lane change test is a manoeuvre where the tires largely operate in their nonlinear/high slip angle region, and thus their pneumatic trail cannot be considered constant. Its calculation was done using the methodology in [49].

### 3.8.2 Tire relaxation

Tire relaxation phenomena were modelled according to the methodology described in section 2.7.4. The dynamic build-up of the lateral forces on the tires was described by a first order

differential equation, which can also be seen as a first order low pass filter. At each time instant, each tire's lateral force should satisfy

$$\tau \dot{f}_y(a, t) + f_y(a, t) = f_{yss}(a) \quad \text{Eq. 103}$$

with a typical value of  $L = 0.3m$  chosen as the relaxation length in Eq. 29 [32].

### 3.8.3 Camber thrust

The lateral force due to camber, the camber thrust, was modelled as an additive force to the lateral force due to slip angle. Although this is not the case in the tires' nonlinear region, it is a simplification used in this work. From the K&C tests “*Camber angle at double side roll movement*,” as can be seen in Appendix G – Kinematics & compliance, where the camber of the wheel with respect to the vehicle body is measured for a given body roll value, Table 9 as well as all other tables in this chapter were obtained:

**Table 9. Camber gain per roll angle  $\frac{\partial \varepsilon}{\partial \varphi} [\text{deg}/\text{deg}]$ .**

	Left wheel	Right wheel
Front axle	+0.243	-0.264
Rear axle	+0.452	+0.434

The roll angle is considered positive when the vehicle leans right as seen from behind (the right side of the car is in jounce while the left in rebound). The decisive parameter for the camber thrust is the camber relative to the ground, the wheel's inclination angle, and therefore a translation from the camber relative to the body, given on the table above, is needed. This translation holds as [19]

$$\gamma_l = \gamma_0 + \varphi - \varepsilon_l . \quad \text{Eq. 104}$$

and

$$\gamma_r = \gamma_0 + \varphi + \varepsilon_r . \quad \text{Eq. 105}$$

for the left and right wheel respectively as seen from behind. The factor  $\gamma_0$  is the static camber of the wheels. For the S60's front wheels the static camber is taken as  $\gamma_{0f} = \varepsilon_{0f} = -0.7^\circ$  and for the rear wheels  $\gamma_{0r} = \varepsilon_{0r} = -1.3^\circ$ , which are typical static camber values for modern passenger vehicles. Also, for the camber stiffness a typical value of  $C_\gamma = 2000 [N/rad]$  was used [19]. The camber thrust for each tire was then calculated from

$$F_{\gamma ij} = -C_\gamma \cdot \gamma_{ij} . \quad \text{Eq. 106}$$

which then was added to the relevant calculated lateral force produced by the tire's slip angle.

### 3.8.4 Fully featured model without ESC

All features described in sections 3.8.1 - 3.8.3 were implemented in a model without ESC. The equations to be inserted into the solver, considering front-wheel steering and travelling on a horizontal plane, with indices corresponding to this model were:

$$\delta_f = \delta + \delta_{rsf} + \delta_{cf}, \quad \text{Eq. 107}$$

$$\delta_r = \delta_{rsr} + \delta_{cr}, \quad \text{Eq. 108}$$

$$\dot{F}_{yfl}(a, t) = (F_{yfl\_ss}(a) - F_{yfl}(a, t)) \cdot \frac{V_{xfl}}{L_{relax}}, \quad \text{Eq. 109}$$

$$\dot{F}_{yfr}(a, t) = (F_{yfr\_ss}(a) - F_{yfr}(a, t)) \cdot \frac{V_{xfr}}{L_{relax}}, \quad \text{Eq. 110}$$

$$\dot{F}_{yrl}(a, t) = (F_{yrl\_ss}(a) - F_{yrl}(a, t)) \cdot \frac{V_{xrl}}{L_{relax}}, \quad \text{Eq. 111}$$

$$\dot{F}_{yrr}(a, t) = (F_{yrr\_ss}(a) - F_{yrr}(a, t)) \cdot \frac{V_{xrr}}{L_{relax}}, \quad \text{Eq. 112}$$

$$m(\dot{v}_x - \psi \dot{v}_y) =$$

$$(F_{xfl} + F_{xfr}) \cos \delta_f + (F_{xrl} + F_{xrr}) \cos \delta_r - (F_{yfl} + F_{yfr}) \sin \delta_f - (F_{yrl} + F_{yrr}) \sin \delta_r - \frac{1}{2} \rho \cdot A \cdot C_d \cdot V_x^2, \quad \text{Eq. 113}$$

$$m(\dot{v}_y + \psi \dot{v}_x) =$$

$$(F_{yrl} + F_{yrr}) \cos \delta_r + (F_{xrl} + F_{xrr}) \sin \delta_r + (F_{xfl} + F_{xfr}) \sin \delta_f + (F_{yfl} + F_{yfr}) \cos \delta_f, \quad \text{Eq. 114}$$

$$I_z \ddot{\psi} =$$

$$f[(F_{yfl} + F_{yfr}) \cos \delta_f + (F_{xfl} + F_{xfr}) \sin \delta_f] - b[(F_{yrl} + F_{yrr}) \cos \delta_r + (F_{xrl} + F_{xrr}) \sin \delta_r] + W_l(F_{yfl} \sin \delta_f + F_{yrl} \sin \delta_r - F_{xfl} \cos \delta_f - F_{xrl} \cos \delta_r) + W_r(F_{xfr} \cos \delta_f + F_{xrr} \cos \delta_r - F_{yfr} \sin \delta_f - F_{yrr} \sin \delta_r), \quad \text{Eq. 115}$$

$$I_w \dot{\omega}_{fl} = T_{fl} - F_{xfl} r, \quad \text{Eq. 116}$$

$$I_w \dot{\omega}_{fr} = T_{fr} - F_{xfr} r, \quad \text{Eq. 117}$$

$$I_w \dot{\omega}_{rl} = T_{rl} - F_{xrl} r, \quad \text{Eq. 118}$$

$$I_w \dot{\omega}_{rr} = T_{rr} - F_{xrr}r , \quad \text{Eq. 119}$$

$$\dot{X} = v_x \cos(\psi) - v_y \sin(\psi) \quad \text{Eq. 120}$$

and

$$\dot{Y} = v_x \sin(\psi) + v_y \cos(\psi) \quad \text{Eq. 121}$$

where  $m$  is the vehicle's mass,  $I_w$  the moment of inertia of each wheel (considered the same for all wheels),  $F_{yij,ss}(a)$  the steady state lateral force of the i,j wheel for a given slip angle  $a$ ,  $W_r$  the distance of the right wheel from the axle's centreline,  $W_l$  the distance of the left wheel from the axle's centreline and  $T_{fr}, T_{fl}, T_{rr}, T_{rl}$  the drive/brake torque on the front right, front left, rear right and rear left wheel respectively. The constraints used for the state and control variables are shown in Table 10.

**Table 10. Constraints for the full vehicle model.**

Variable constraints	Description
$V_x \geq 10^{(i)}$	The car's longitudinal speed in m/s
$-10 \leq V_y \leq 10^{(i)}$	The car's lateral speed in m/s
$-\pi/2 \leq \psi \leq \pi/2^{(i)}$	Yaw angle in rad
$-4 \leq \dot{\psi} \leq 4^{(i)}$	Yaw rate in rad/s
$-31.5^\circ \leq \delta \leq 31.5^\circ$	Steering angle in degrees
$-4\pi/i \leq \dot{\delta} \leq 4\pi/i^{(ii)}$	Steering angle rate in rad/s
$X(t = 0) = 0^{(iii)}$	Initial longitudinal position of the CoG in m
$X(t = t_{final}) = 61^{(iii)}$	Final longitudinal position of the CoG in m
$width/2 - A/2 \leq Y(t = 0) \leq A/2 - width/2^{(iii)}$	Initial vertical position of the CoG in m
$width/2 + A/2 - C \leq Y(t = t_{final}) \leq A/2 - width/2^{(iii)}$	Final vertical position of the CoG in m
$\psi(t = 0) = 0^{(iv)}$	Initial yaw angle in rad
$\dot{\psi}(t = 0) = 0^{(iv)}$	Initial yaw rate in rad/s
$\delta(t = 0) = 0^{(iv)}$	Initial steering angle in rad
$V_y(t = 0) = 0^{(iv)}$	Initial lateral velocity in m/s
$10/r \leq \omega_{fl} \leq 80/r^{(i)}$	Front left wheel rotational speed rad/s
$10/r \leq \omega_{fr} \leq 80/r^{(i)}$	Front right wheel's rotational speed rad/s
$10/r \leq \omega_{rl} \leq 80/r^{(i)}$	Rear left wheel's rotational speed rad/s
$10/r \leq \omega_{rr} \leq 80/r^{(i)}$	Rear right wheel's rotational speed rad/s
$\omega_{fl} \cdot r \leq 1.2 \cdot V_x^{(v)}$	Indirect limitation on front left wheel slip
$\omega_{fr} \cdot r \leq 1.2 \cdot V_x^{(v)}$	Indirect limitation on front right wheel slip
$\omega_{rl} \cdot r \leq 1.2 \cdot V_x^{(v)}$	Indirect limitation on rear left wheel slip
$\omega_{rr} \cdot r \leq 1.2 \cdot V_x^{(v)}$	Indirect limitation on rear right wheel slip

(i) Constraints to help limit the search space. In order to help the optimizer converge to a solution this limitation should be neither too loose nor too strict [6].

(ii) Constraint that prevents the steering output from being faster than a human driver or steering robot [47]. This constraint was added to the model only after the first visit to Hällerod test track took place. Initially, only the steering angle  $\delta$  was restricted, and the resulted steering rate, being unrestricted, was too high. As a result, the steering torque request from the steering robot was also too high and the robot could not perform the manoeuvre. In a later step, this restriction to the steering rate was posed.

(iii) Constraints that limit the vehicle movement into some specific boundaries dictated by the manoeuvre.

(iv) Constraints that define the entrance of the vehicle to be in a straight driving manner.

(v) The wheel speed was limited to never exceed 120 % of the vehicle longitudinal speed to reduce the search space.

The cost function was kept the same as in Eq. 53 with the weight factor,  $W_\delta$ , set to 0.111 in the first iteration step and then 0.042 in the solution.

### 3.9 Parameter study

This parameter study was primarily intended to investigate the influence of the various vehicle parameters on the maximum entry speed and study the robustness of the method, especially for vehicles as the core study vehicle, the Volvo S60 2013. Robustness, R, was here defined by

$$R = \frac{100n_s}{n_{tot}} \quad \text{Eq. 122}$$

where  $n_s$  is the number of solved<sup>17</sup> cases,  $n_{tot}$  is the number of tested cases and R is then given in percentage of the total number of tested cases. This robustness metric can then be used to give an indication of whether the controller can be used as a generic controller to find a path. The differences between the resulting steering angle inputs, when comparing the four-wheel vehicle model with different features implemented, were very small (section 4.1). However, the simulation time of the model with most features implemented was up to 100 times longer compared to the model with least features<sup>18</sup>. For that reason the parameter study was based on the four-wheel vehicle model with yaw rate controlled ESC and roll kinematics but no tire relaxation and no wheel kinematics. 80 collocation<sup>19</sup> points as solution for each variable were used for all parameter studies and the influence of the number of discrete points was also studied, which was of interest to determine the minimum number of points needed.

#### 3.9.1 Vehicle parameter changes

Parameters that describe the vehicle geometry, as well as its mass and the tire model, were selected for performing changes of the vehicle properties. Those parameters have an impact on both the shape of the double-lane change track as well as on the vehicle response. Tire forces dictate what is possible to do in terms of aggressive manoeuvres, thus it was also of interest to study the tire model effects.

---

<sup>17</sup> A case was considered "solved" when Tomlab gave the output message "Optimality conditions satisfied" as defined by the Tomlab manual [6] and described, together with outer outputs, in the Tomlab guide [12].

<sup>18</sup> The most complex model includes all features as defined by section 3.7.3 and chapter 3.8 while the model with least features refers to the linear bicycle model as described in section 3.4.1.

<sup>19</sup> The solution takes the form of a polynomial function that satisfies all collocation points [4].

**Table 11.** Setup scheme for all vehicle parameter changes. When one of the parameters was changed the rest were set according to their base values while non-specified parameters were set according to Appendix B – Test vehicle.

Parameter	Nominal value	Variation	Step
Weight	1823 kg	$\pm 500$ kg	50 kg
Yaw inertia	3500 kgm <sup>2</sup>	$\pm 500$ kgm <sup>2</sup>	50 kgm <sup>2</sup>
Body length	4.635 m	$\pm 0.5$ m	0.05 m
Body width <sup>20</sup>	1.865 m	$\pm 0.5$ m	0.05 m
Magic formula tire stiffness, (B*constant, C*constant, D*constant)	12.6118	$\pm 50$ %	10 %
Magic formula, B	7.5418	$\pm 50$ %	10 %
Magic formula, C	1.4897	$\pm 50$ %	10 %
Magic formula, D	1.1233	$\pm 50$ %	10 %

All parameter variations that were used to study the influence from individual parameters can be seen in Table 11. When changing the tire specifications the same changes were always used for all tires. But a special case was also investigated, namely the case of keeping the product  $B*C*D$  constant while changing  $D$  according to Table 12.

**Table 12.** Special case of the tire parameter study, constant tire stiffness but variations of the parameter D.

Parameter	Nominal value	Variation	Step
Magic formula, D	1.1233	$\pm 50$ %	10 %

The product  $B*C*D$  was kept constant by using the relations given by Eq. 123, Eq. 124 and Eq. 125.

$$D = D_{nominal\ value} * D_{gain} \quad \text{Eq. 123}$$

$$B = B_{nominal\ value} * \sqrt{\frac{1}{D_{gain}}} \quad \text{Eq. 124}$$

$$C = C_{nominal\ value} * \sqrt{\frac{1}{D_{gain}}} \quad \text{Eq. 125}$$

This corresponds to a tire that always has the same cornering stiffness but different peak force.

<sup>20</sup> The ISO-3888 track sections width depends on the vehicle body width [1].

### 3.9.2 ESC-characteristics variations

The way the ESC applies the braking torque influences the entry speed; this influence was studied. An upper limit that cannot be exceeded with any ESC is posed by the optimal torque controller described in section 3.7.1; this optimal controller cannot be changed but can serve as a reference for various ESC configurations. No threshold and an optimal ESC algorithm would result in the same entry speed as the optimal torque controller, but not higher, since the ESC then is always activated.

With a constant ESC activation threshold, it was investigated how its braking torque characteristics influenced the entry speed; first by keeping the torque increase factor constant while changing the initial torque at the activation point and secondly by keeping the initial torque constant and changing the torque increase factor.

**Table 13. ESC-torque characteristic variation; all combinations of the specified parameters were used while non-specified parameters were set according to Appendix B – Test vehicle.**

Parameter	Base value	Variation	Step
Initial torque at the ESC activation yaw error	200 Nm	- 200 Nm + 100 Nm	50 Nm
Torque increase factor	5	$\pm 5$	0.5
Yaw error threshold	2 °	$\pm 2$ °	1 °

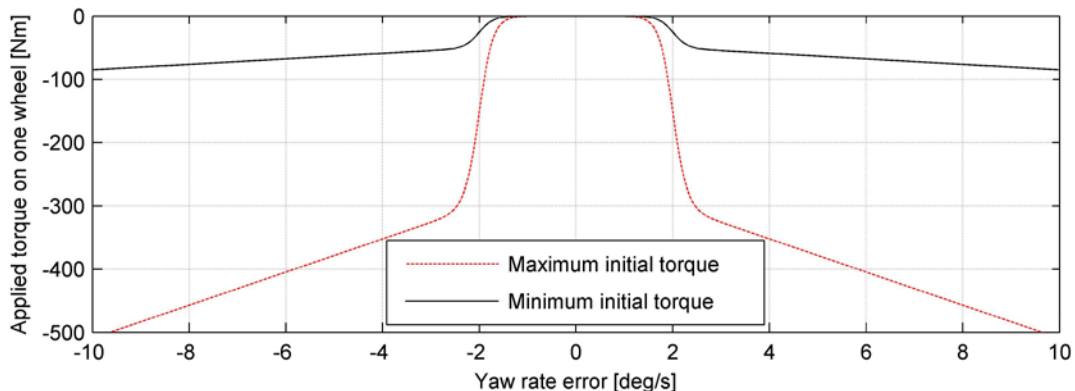


**Figure 19. ESC characteristics when changing only the initial torque.**

In Figure 19 the torque characteristics can be seen for the lowest tested initial torque as well as for the highest; for the base value of the torque increase factor and yaw rate error threshold. All tested values used during the study are given in Table 13. No initial torque at all represents a deactivated ESC system.

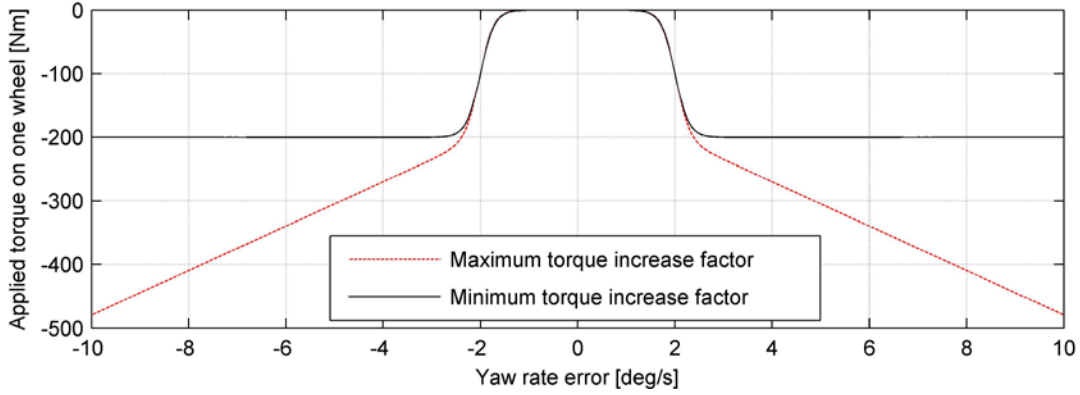


**Figure 20. ESC characteristics when changing only the torque increase factor.**

In Figure 20 the torque characteristics can be seen for the lowest tested torque increase factor as well as for the highest, for the base value of the initial torque and yaw error threshold, while all tested values used during the study are given by Table 13. A torque increase factor of zero represents a constant applied torque after the threshold limit has been reached. The smoothness factor, which determines the transition between the inactive ESC and activated ESC, was not changed during the parameter study.

An optimal ESC implementation derived an entry speed to be used as a reference; such an ESC would only brake when the specified yaw rate error threshold had been exceeded. The torque magnitude would not be limited while the torque application rate was limited to

$$-25000 \leq \dot{T}_{ij} \leq 7500 \text{ Nm/s} \quad \text{Eq. 126}$$

according to brake specifications given by [50].

### 3.9.3 Influence of discretization

An optimal solution was found in a finite number of points along the track, hence it was possible to obtain solutions which are not necessarily optimal between two consecutive collocation points. However, if the distance between two consecutive points approaches zero, the difference to the last result should also approach zero.

To study the effect of the collocation points, the entry speed was studied as a function of their number during the optimization. This was done in steps of 5 points from 20 points up to 150 points for the bicycle model with a linear tire model. For the models with more features this variation of discrete points was not possible to perform within this study due to the very long time to perform one single optimization.

### 3.10 Animation of a car along the track

Animation of the result facilitates subjective judgement of the result, and hence identify the parts of the model that need a more detailed and objective approach. During this study the vehicle, as well as the wheels, were visualized as rectangles and seen from above following the path of a polynomial function going through all of the discrete points. In each wheel arrows were plotted to show the braking torque as well as the lateral tire force. This information made it possible to gain understanding about the vehicle behaviour as it provided help to determine the validity of all the geometrical constraints. Another important benefit from the animation was that the controller could also be visualized, in Figure 21 an example of such an animation can be seen.

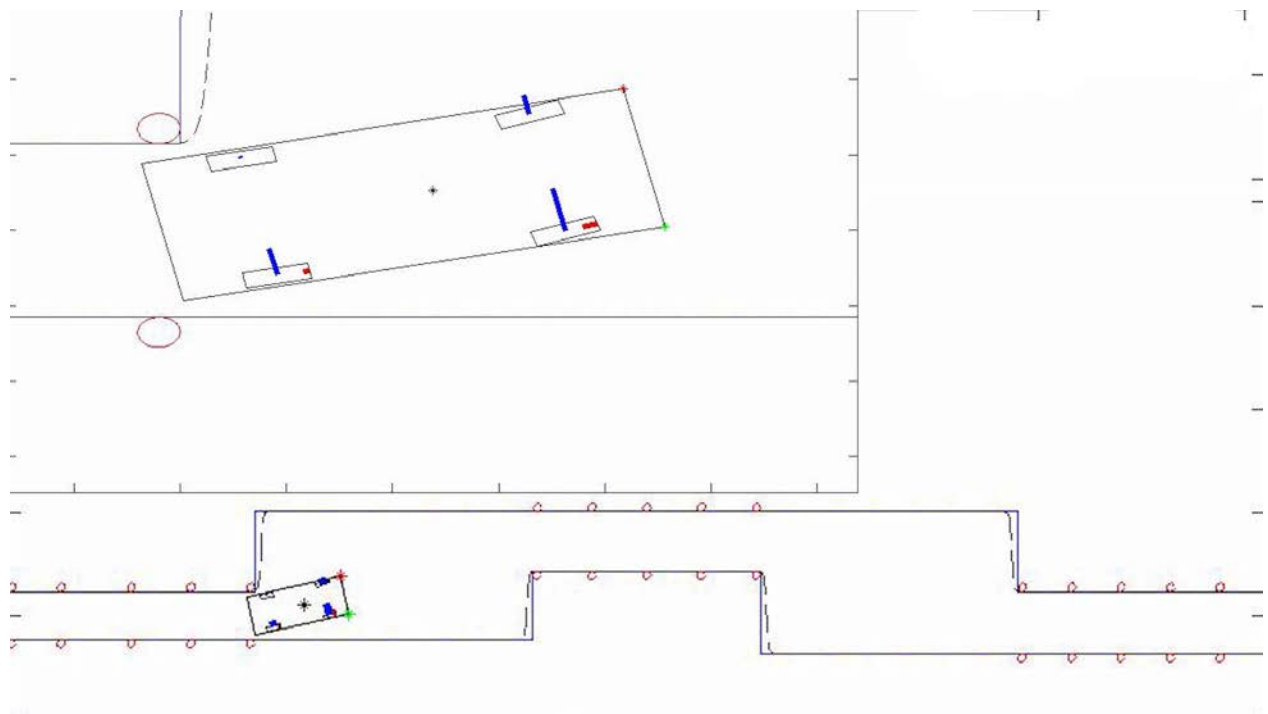


Figure 21. Vehicle animation along the double-lane change track with illustrated lateral forces as well as braking torque.

### 3.11 Steering robot test 1; driving procedure

After the vehicle dynamics model and the ESC implementation were built, physical tests were performed for estimating the vehicle's parameters as well as assessing the model's realism. The model featured four-wheel dynamics, roll kinematics and an optimal torque controller that was activated after 12 m. The late activation limitation was included to get characteristics closer to a real ESC, which would not brake as long as the vehicle is driving straight, while an optimal torque controller can brake even when travelling straight. During all manoeuvres, which will be described in this chapter, the recorded data consisted of the parameters listed in Table 14.

**Table 14. Recorded parameters during testing.**

Parameter	Accuracy
Time	Unknown
Steering robot angle	0.0008 °
Steering robot Torque	± 2 %
Steering robot Column Torque	± 2 %
X position	3 cm
Y position	3 cm
Forward velocity	0.05 km/h
Lateral velocity	2 %
Forward acceleration	0.01 m/s <sup>2</sup>
Lateral acceleration	0.01 m/s <sup>2</sup>
Vertical acceleration	0.01 m/s <sup>2</sup>
Roll angle	0.03 °
Pitch angle	0.03 °
Yaw angle	0.03 °
Roll velocity	0.01 °/s
Pitch velocity	0.01 °/s
Yaw velocity	0.01 °/s
Slip angle	0.15 °
Yaw acceleration	Unknown

Steady state cornering was performed both in a left and right turn. The calculated optimal path through the ISO-3888 track was then intended to be driven both with and without ESC activated. As a last step the car was also driven manually through the track; an indication of the validity of the optimal controller would be the comparison between the entry speed it achieved and the maximum entry speed achieved by a human driver. The controller would be expected to always achieve higher entry speeds.

The generated optimal steering angles were imported to the steering robot and by running the test at a lower speed it was possible to verify that the robot could perform the requested operations. In this case the steering angle rate showed to be faster than the robot could handle; the steering angle rate limit was then introduced in the model, but the new optimal solution then had larger steering angles than the car could handle which led to a correction of the model steering angle limit too.

### 3.11.1 Parameter estimation

As mentioned earlier, four circular driving tests with constant radius, and pseudorandom steering at constant speed were conducted during the first test run. These additional tests were performed for acquisition of data that would allow some post process as well as some vehicle parameter evaluation. The tests were performed both by a human driver and a

steering robot<sup>21</sup>. The parameters that needed to be calculated were the effective cornering stiffness for the front and rear axle, so that the  $B$ ,  $C$  and  $D$  parameters of the magic formula can be eventually calculated, and the vehicle's yaw moment of inertia [45].

Despite the performance of such tests though, the vehicle's parameters evaluation could not be conducted in the usual systematic manner described in section 2.9 in the case of this thesis. The reason for this is that the recorded lateral velocity and sideslip angle data from the circular driving tests could not be used as the IMU had not been set up correctly. For the interested reader Appendix H - Test 1 data illustration provides an illustration of the data that were recorded.

As the recorded steering wheel angle comes directly from the measurement of the steering wheel position while the recorded lateral velocity and sideslip angle come after a calculation that the IMU performs<sup>22</sup>, it becomes apparent that the lateral velocity and sideslip angle values could not be used. Since the recordings of the lateral velocity hindered the calculation of the axles' effective cornering stiffness another method was used to approximate those values. For the yaw inertia  $I_z$ , the empirical formula

$$I_z = 0.46 * m * L * t \cong 3500 \text{ kgm}^2 \quad \text{Eq. 127}$$

was used [51] with  $m$ ,  $L$  and  $t$  being the vehicle mass, wheelbase and track width respectively, with a 68% confidence level.

The magic formula's  $B$ ,  $C$  and  $D$  values for the S60's tires would be attempted to be found via curve fitting using the recordings from the double lane change manoeuvres.

Nine double lane change tests were conducted and recorded. The idea was to build a model, where the  $B$ ,  $C$  and  $D$  values could be modified. This model would be subjected to the longitudinal velocity  $V_x$  and steering angle  $\delta$  according to the recordings from the real vehicle tests. The model would output some results for the yaw rate and the lateral acceleration and these results would be compared with the recorded/real vehicle results. The  $B,C,D$  values of the model would then be modified accordingly such that the curves from the model and from the recordings fitted as close as possible.

---

<sup>21</sup> Volvo's test engineer Per Hesslund performed the tests. The steering robot used was an SR60 standard robot by Anthony Best Dynamics.

<sup>22</sup> The IMU used in the test records the output from accelerometers and gyroscopes and with the use of observers (Kalman filters) it calculates also other values, like the velocities [50]. This design though is sensitive to accumulating error from the integral action of the observer, which makes it unsuitable for this kind of test (circular driving). Instead, a twin-antenna GPS or a slip angle optical sensor could be used to obtain reliable values for the vehicle's slip angle and lateral velocity [51].

The model that was used for the fitting was a bicycle model with nonlinear tires and was built in Simulink. For simplicity only the lateral tire slip was included in the modelling. The input to the model was, as mentioned, the recorded longitudinal velocity and steering angle from the test. The output of the model, the yaw rate and lateral acceleration, was used in the curve fitting. The Simulink model is shown in Appendix I - Simulink bicycle model.

Before comparing the model results with the recorded results some filtering was needed for the recorded ones, since the measurements were noisy and as pure a curve as possible was desired<sup>23</sup>. The fitting process was approached as a nonlinear programming problem and Matlab's "*fmincon*" function was used. In the objective function the error between the model's output and the respective measured data was calculated and minimized. In order to avoid over fitting the total error of all the nine double lane change tests, rather than the error of an individual test, was calculated and used as a minimization objective. The total error for each iteration was the sum of the individual errors from each model.

### 3.12 Steering robot test 2; driving procedure

During the second test the main goal was to study the influence of the model features that were used in the prediction as well as to determine the accuracy of the estimated result. It was also of interest to assess the extent to which the real ESC could be approximated with the simple ESC implementation of this thesis. The vehicle was therefore driven through the track with optimized steering angles according to a vehicle model with ESC models that had different characteristics. Then it was also driven with optimized steering angles according to vehicle models of varying detail as well as the standard subjective test was performed. Characteristic values for each tested ESC as well as entry speed can be seen in the manoeuvre test list in Appendix D – Test 2 manoeuvre test list.

While the vehicle parameters were estimated from driving data during the first test (section 3.11), the second test was performed two months after the first one, and thus environmental changes were expected. In a case of a wet test track it was assumed that such conditions would lower the tire peak force capability by 30 %, though the tire cornering stiffness remained the same. Each tire setting as well as features that were implemented in the model during each test can be seen in Appendix D – Test 2 manoeuvre test list. During the testing day the asphalt was wet and the optimization results from both tire settings were used to perform the tests.

---

<sup>23</sup> For filtering the yaw rate and lateral acceleration a second order Butterworth low pass filter was used, with a normalized cut-off frequency of 0.2. The signal was filtered both in the forward and reverse direction for avoidance of phase shifting introduced by one-directional filtering.

# 4 Results

Except for the parameter study all results shown within this chapter are related to the Volvo S60 2013 given by Appendix B – Test vehicle, which was also used during the tests with a steering robot. The results from the parameter study show how robust the method used in this study is and hence give an indication of how much different a vehicle can be, compared to a Volvo S60 2013, in order to still be able to calculate the optimal steering angles. If not stated differently the nominal parameters for the vehicle model are assumed as:

- Two track model with yaw rate error controlled ESC
- No tire relaxation, no wheel kinematics and no suspension compliance (Negligible influence to the steering output)
- ESC yaw rate threshold of  $2^\circ$
- ESC activation torque of 200 Nm
- ESC torque increase factor of 5
- Vehicle parameters according to Appendix B – Test vehicle

#### 4.1 Optimal controller driving inputs

The optimal steering angles achieved when using different features in the model can be seen in Figure 22, making it obvious that the modelled features play a significant role in this kind of manoeuvre as the steering angle input difference between the cases can be  $10^\circ$ .

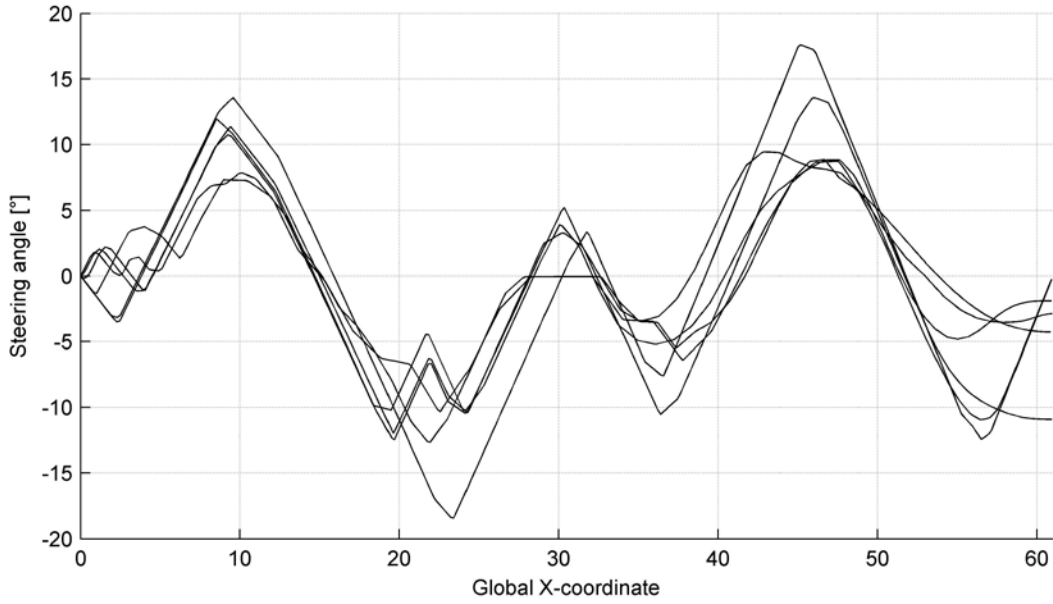


**Figure 22. Steering angles input calculated with different vehicle modelling features implemented.**  
The graph illustrate the scattering of the result.

The largest magnitude in Figure 22 derives from the linear bicycle model, since that model allows higher lateral force generation than the other models just by increasing the steering angle. The bicycle model with a magic formula tire model is however among the four lines in the figures that are closest to each other, being thus already a significantly improved model. Between  $X = 40$  and  $X = 50$  the differences are biggest between the different models, Figure 22 shows that part in detail.

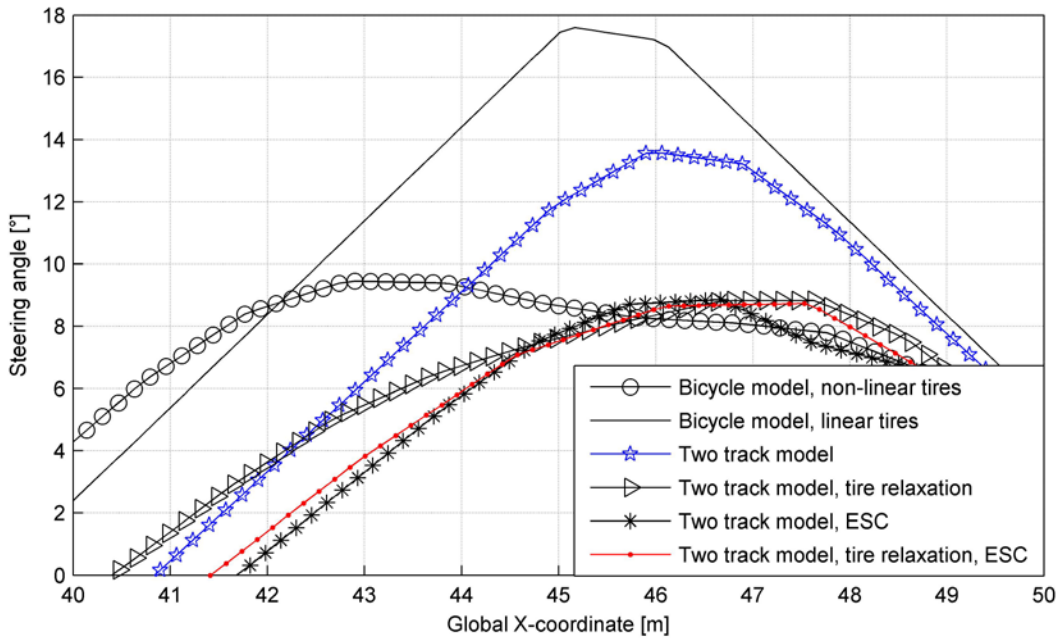


**Figure 23.** Optimal steering angles calculated with different models. In this figure non-linear tires refer to the magic formula and are used for all two track models. The ESC refer to the yaw rate error controlled ESC. It should be noted that the linear model also has half of the equivalent tire stiffness compared to the non-linear tires to make it behave more realistic as described in 3.4.1 Linear tire model.

It is seen that the bicycle model with non-linear tires is closer to the two track model, with tire relaxation, than the usual two track model at the position of the peak steering angles, but it is the opposite situation when not at the peak. That makes the tire relaxation an important part of the model when the ESC is not activated. When the ESC is present in the model there is however almost no difference between a model with or without the tire relaxation effect, thus it is not an important component of the model in that situation. If one also compares the maximum entry speeds that each model gives as a result, Table 15 is obtained.

**Table 15.** Maximum entry speed with different models. In this table non-linear tires refer to the magic formula tire model and are used for all two track models. ESC refers to the yaw rate error controlled ESC.

Model	Entry speed
Bicycle model, linear tires	69.1 km/h (90.7 km/h) <sup>(i)</sup>
Bicycle model, non-linear tires	68.5 km/h
Two track model	70.8 km/h
Two track model, tire relaxation	69.6 km/h
Two track model, ESC	73.6 km/h
Two track model, tire relaxation, ESC	72.5 km/h

(i) If the tire cornering stiffness is equivalent to the non-linear tire model cornering stiffness.

When comparing the entry speeds it is obvious that the linear bicycle model was unrealistic; thus the half equivalent tire cornering stiffness (resulting from the  $B$ ,  $C$ ,  $D$  product) was used. It can also be seen that the bicycle model with non-linear tires results in a speed closer to the two track model with tire relaxation, than the usual two track model, in a similar manner to how the peak steering angle was closer for the bicycle model. Tire relaxation lowers the entry speed with approximately 1 km/h in both the case of a model with ESC as well as without, something which was also seen for other specifications of the tires.

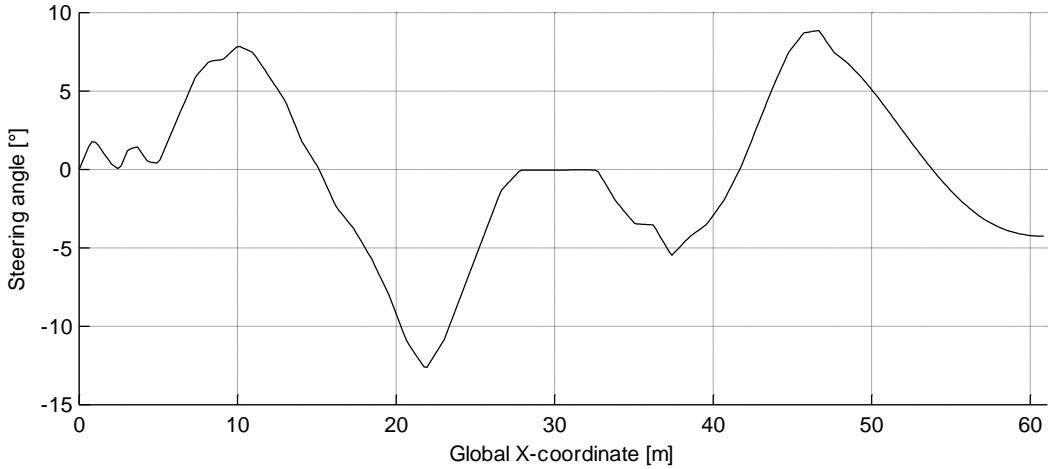


**Figure 24. Optimized steering angle input in the case of a nominal set-up.**

In Figure 24 the steering angles along the double-lane change track can be studied for the case of a nominal set-up.

## 4.2 Optimal trajectory

The case of implementing a bicycle model with linear tires, a bicycle model with Magic formula tires, a two track model with and without tire relaxation as well as a two track model with ESC with and without tire relaxation was studied in the same plot in Figure 25.

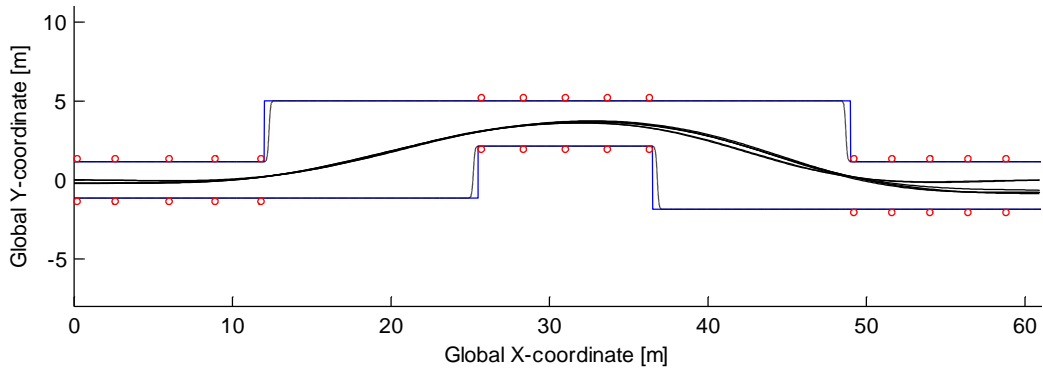


**Figure 25. Trajectory with different modelling implementations.**

As was seen in Figure 25 the optimal trajectory had the same general shape Independent of the modelled features. In Figure 26 it can be seen for the case of a nominal set-up.

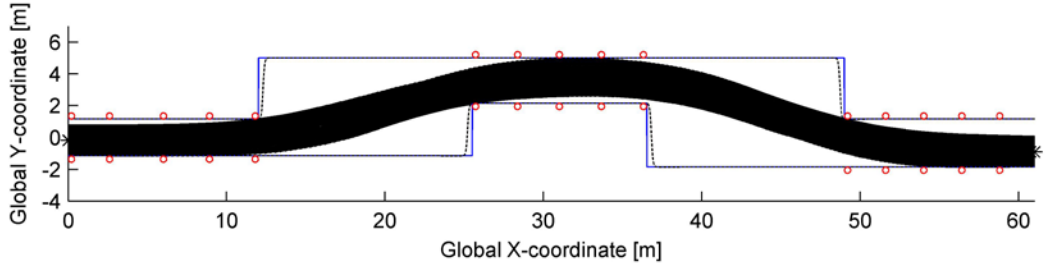


**Figure 26. Vehicle trail when the vehicle was set up with nominal values.**

The trajectory can be seen passing close to three of the cones in the track. Those parts were investigated by using the animation tool described in section 3.10 in which no boundary was violated.

### 4.3 ESC influence

Influence here refers to the difference between the results when an ESC model is used in the optimization algorithm and when it is not. Different ESC models had different influence, as the model was constructed in such a way that it is possible to use some ESC settings which would result in no influence at all; for this comparison the yaw rate error controlled ESC was used with a yaw rate error threshold of  $2^\circ$ , an initial torque upon activation of 200 Nm and a torque increase factor of 5 while the vehicle parameters were set according to Appendix B – Test vehicle. The reason to use that type of ESC is that it solves its equation set quickly with continuous functions. As discussed in section 4.2, there was almost no difference in the trajectory when using an ESC, compared to when not using it. The difference there was is therefore studied as the absolute lateral deviation between the two trajectories in Figure 27.

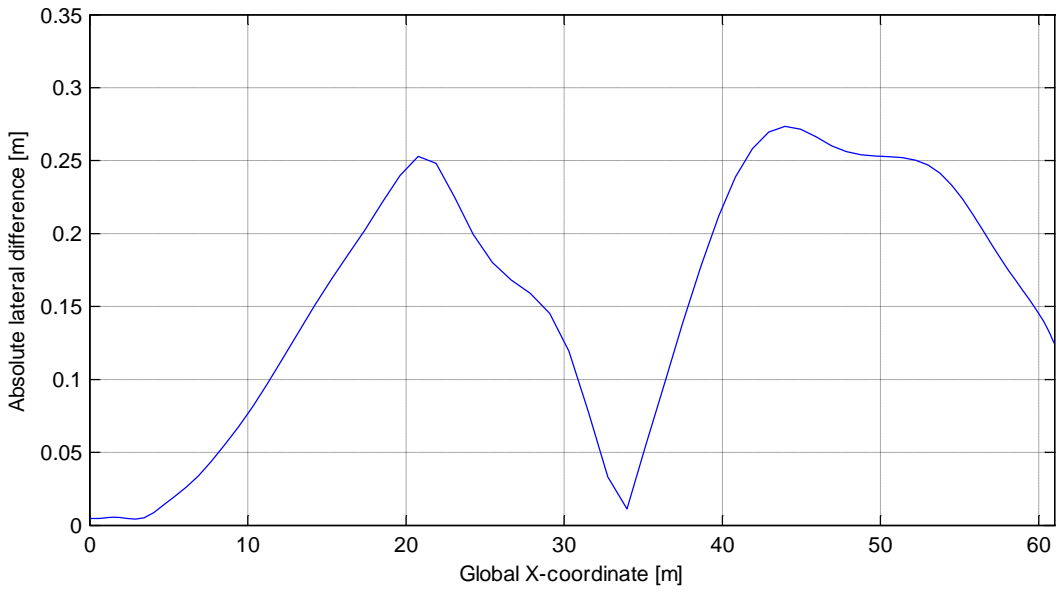


**Figure 27.** Absolute lateral difference between optimization with and without ESC present in the model.

It is shown in Figure 27 that the absolute lateral difference, when adding the ESC to the system, is normally less than 0.27 m along the track. The difference is largest at the same position as where the steering angles deviate the most, as seen in Figure 23. As there are two peaks, between which the difference almost reaches zero, the difference does not tend to increase by accumulating errors. The steering angles, which were shown to be more dependent upon the features that were modelled in section 4.1, can be seen with and without ESC present in the model in Figure 28.

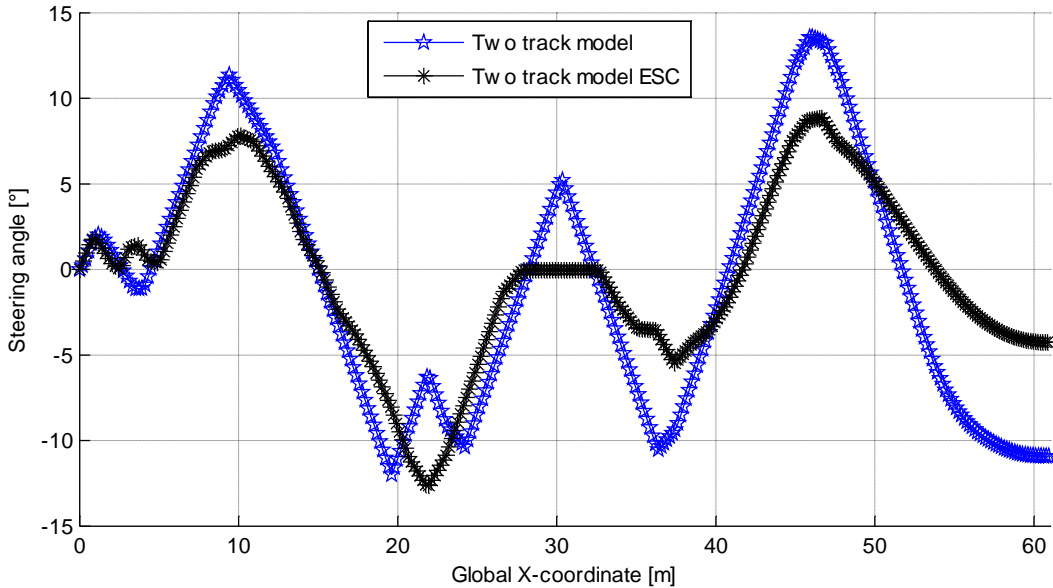


**Figure 28.** Steering angles with and without ESC present in the two track model.

From Figure 28 it is obvious that all steering angle peaks are lowered when the ESC is used, something which could be expected as steering motion is not only generated by the steering of the wheels but also from the braking torque on each wheel (which produces a yaw torque). Figure 29 shows the same comparison for the steering angle rate.

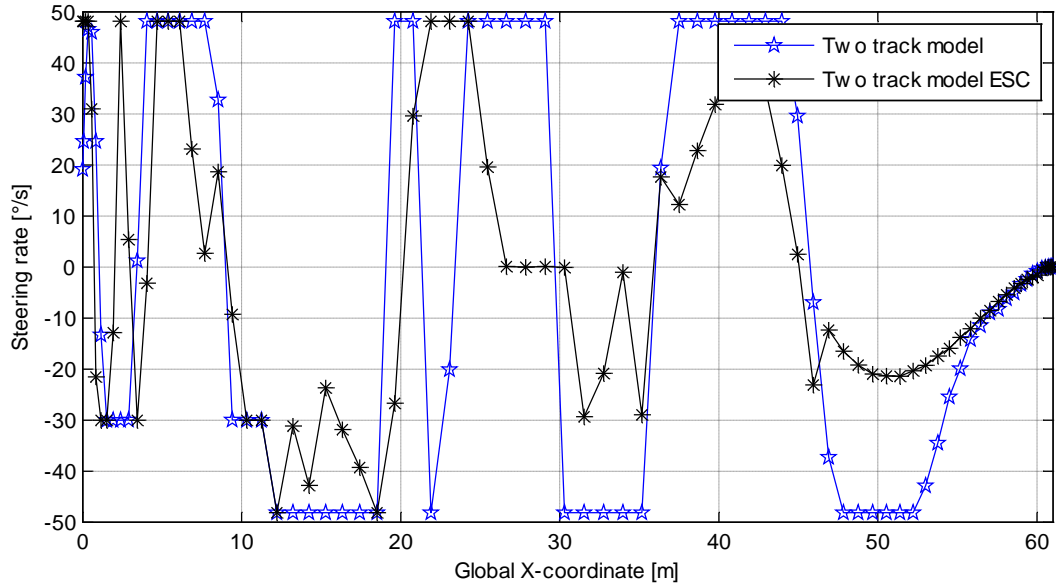


**Figure 29. Steering angle rate with and without ESC present in the model.**

One can see that the steering angle rate transition between different values is smoother when the ESC is used while the case without ESC has an abrupt change between a positive and negative rate at several positions along the track.

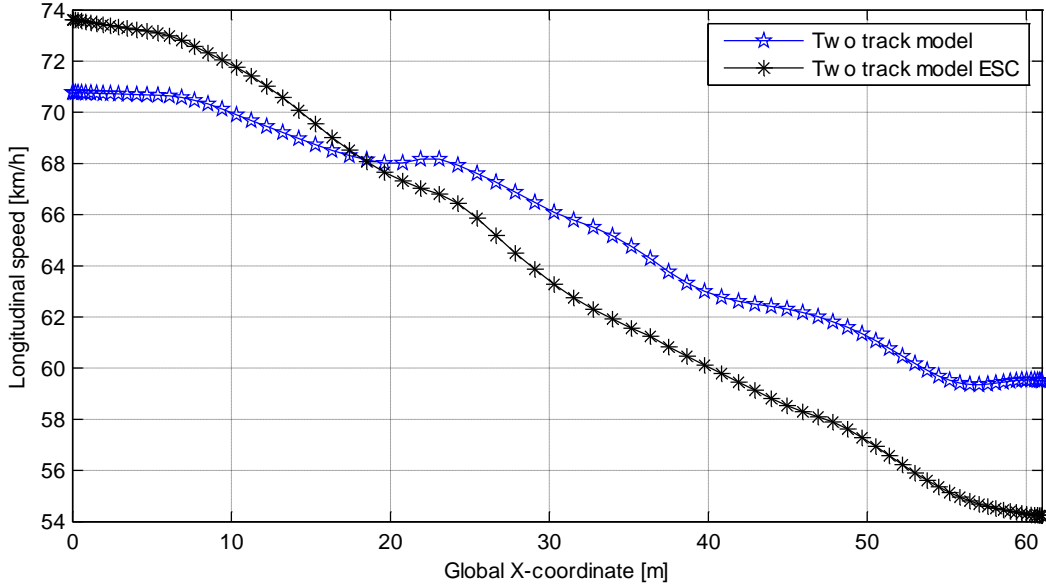


**Figure 30.** Longitudinal speed comparison between the two track model with and without ESC included in the optimization.

The slower changing steering angles and their lower amplitudes due to braking allow for higher entry speed, as seen in Table 15, but also a lower speed along a large part of the track compared to the model which does not include ESC as can be seen in Figure 30.

For the case of an ESC which would be activated at the yaw rate threshold specified, using the optimal braking torque for each wheel, the steering angle can be seen in Figure 31.

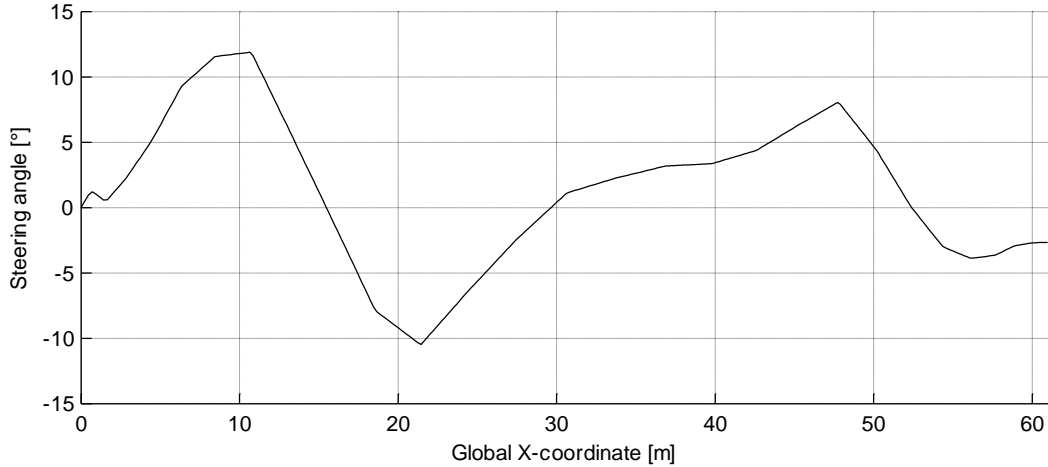


**Figure 31.** Steering angles resulting from an optimization with a Yaw rate error activated optimal torque controller.

Comparing the steering angles between Figure 31 and the nominal case (Figure 24) a smoother behaviour is observed for the former. The corresponding braking torque for each wheel is shown in Figure 32 for the front wheel and in Figure 33 for the rear wheels.

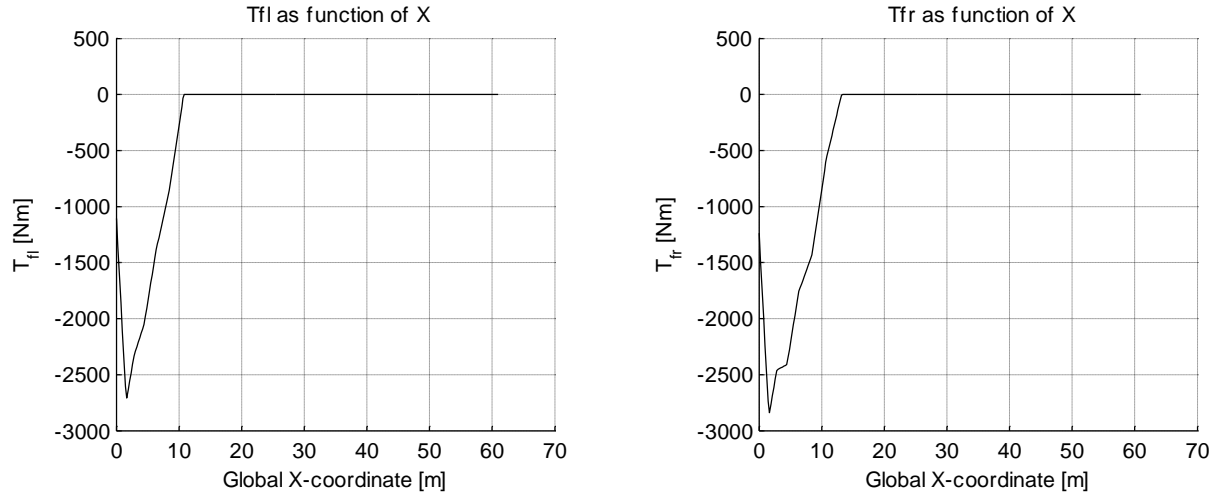


**Figure 32.** Braking torque in the case of a Yaw rate error activated optimal torque controller, to the left for the front left wheel and to the right for the front right wheel.

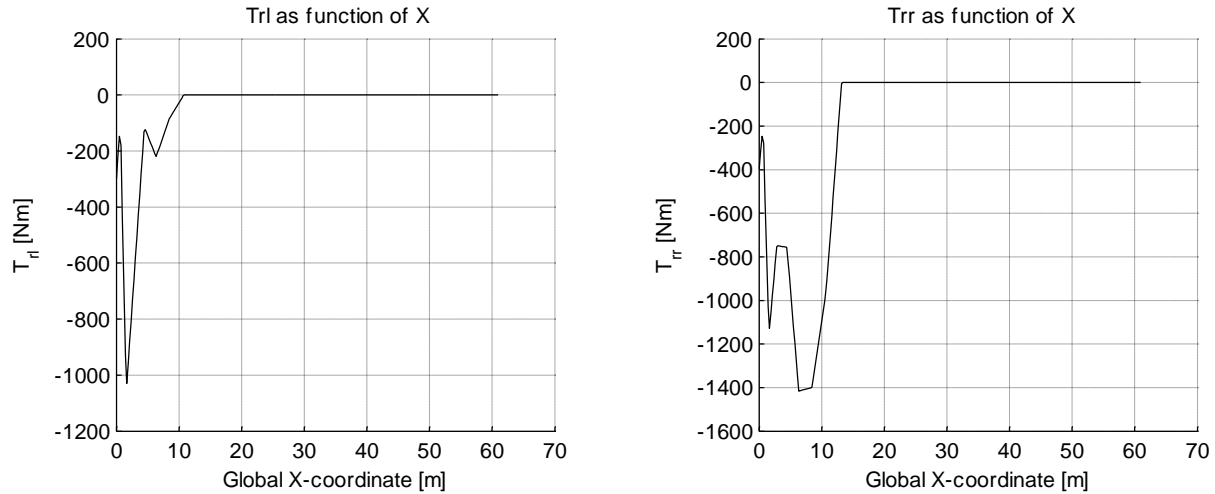


**Figure 33.** Braking torque in the case of a Yaw rate error activated optimal torque controller, to the left for the rear left wheel and to the right for the rear right wheel.

In Figure 32 and Figure 33 it can be seen that braking only occurs in the entry part of the track.

#### 4.3.1 Other ESC models investigated

For the sideslip angle controlled ESC a solution was found, despite inclusion of discontinuous functions, but even minor changes to the vehicle specifications, wheel torque proportional constants or ESC activation threshold made it impossible for the solver to converge towards one solution. For this reason it was regarded as unsuitable to use, as the optimization procedure is intended to be fully automated.

In the case of yaw rate error and sideslip angle controlled ESC a second optimization problem needs to be solved within the ESC equation set, as each contact force due to ESC

interaction is optimized individually in such a case. Thus it would require many more iterations for a numerical solver and within the time frame of this study it was not possible to investigate the solution of this further.

#### 4.4 Steering robot test 1

From the robot driven double-lane change tests the measured lateral acceleration, yaw rate and longitudinal speed were used; the estimated front magic formula coefficients ( $B$ ,  $C$  and  $D$ ), were found as 7.5318, 1.4897 and 1.1233 respectively with a yaw inertia of  $3500 \text{ kgm}^2$ .

The generated optimal steering angles from the simulation were inserted to the steering robot and by running the test at a lower speed it was possible to verify that the robot could perform the requested operations. In this case the steering angle rate showed to be faster than the robot could handle; the steering angle rate limit was then introduced in the model, but the new optimal solution had larger steering angles than the car could handle which led to a correction of the model's steering angle limits as well. The performance of the controller during the first driving test can be seen in Appendix C – Measured data part 1. An illustration of the steering robot set-up can be seen in Figure 34 while Figure 35 and Figure 36 show the vehicle during testing with that robot. The vehicle is also shown during a manual driven test through the double-lane change cone track in Figure 37.



Figure 34. SR60 standard robot by Anthony Best Dynamics mounted on the vehicle.



Figure 35. Entry of the double-lane change track where the vehicle is driven by the steering robot.



Figure 36. Middle section of the double-lane change track where the vehicle is driven by the steering robot.

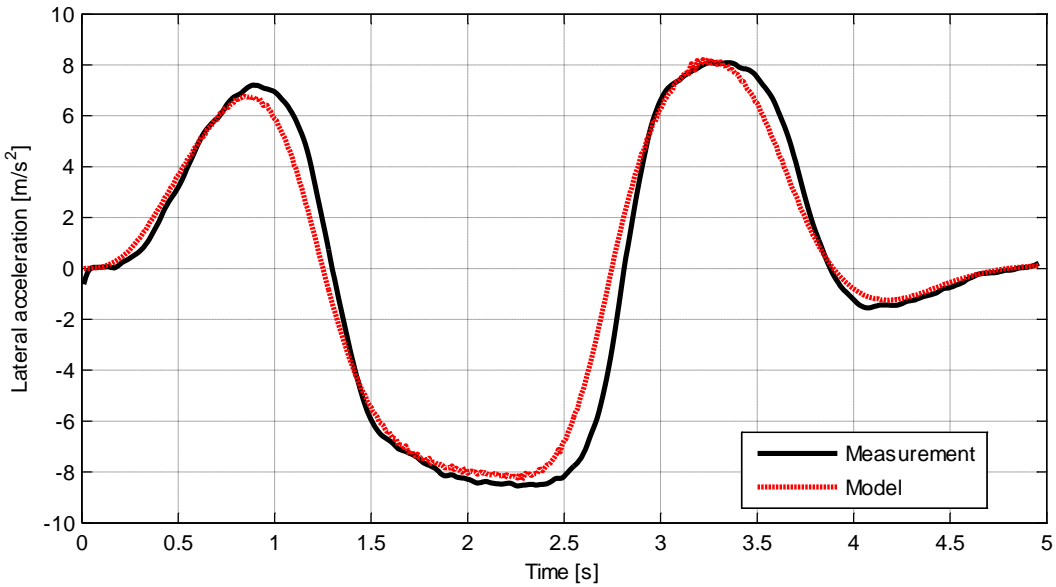


Figure 37. Manual driven vehicle through the double-lane change track.

#### 4.4.1 Parameter estimation

Starting from different initial guesses, the curve fitting procedure using the double-lane change recordings would converge to some different set of values for  $B$ ,  $C$  and  $D$ , though all of these values were close. This indicates that several local optima could be found with this

approach. But, since it is an approximate rather than a systematic and accurate method, such a result was expected.



**Figure 38 - Fitting between the measured and the calculated lateral acceleration.**

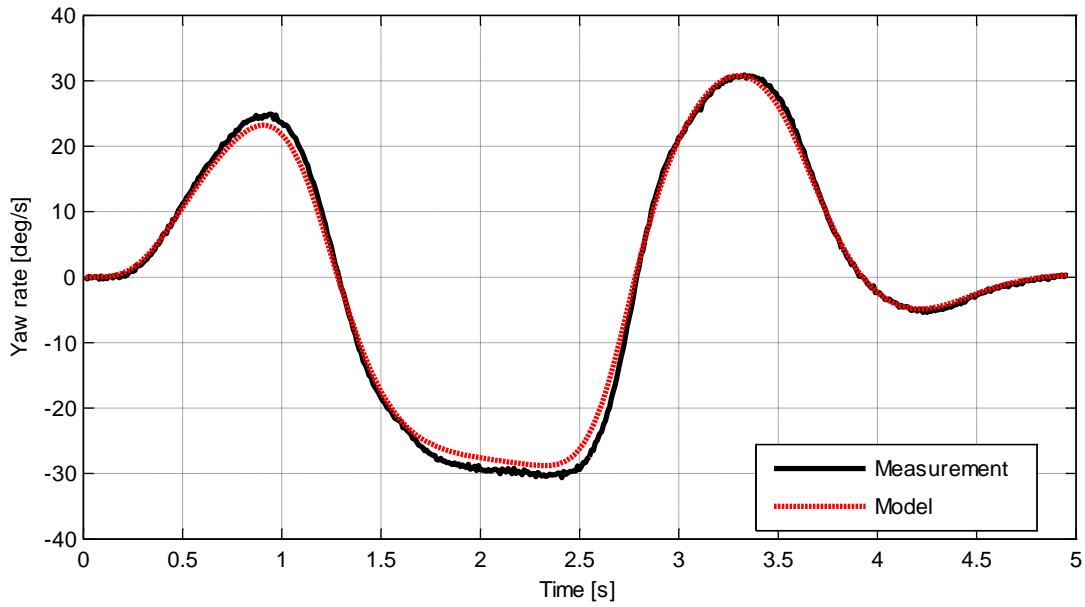


**Figure 39 - Fitting between the measured and the calculated yaw rate.**

An example of the results is shown in Figure 38 and Figure 39; the output of the model is plotted along the respective recorded values. Also, the curve of the tire model, that this approach resulted in, can be seen in Figure 40.

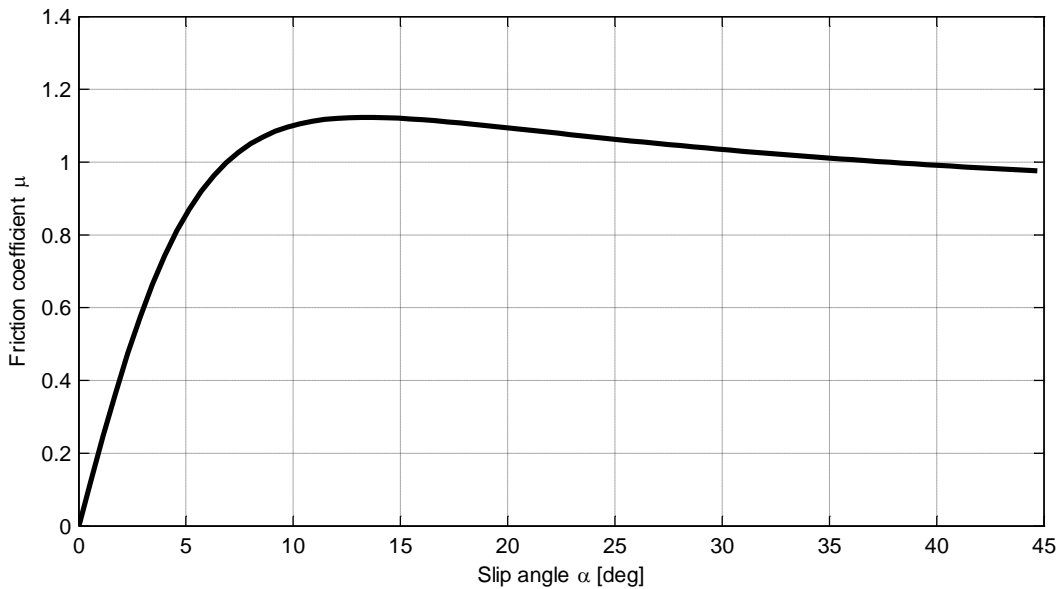


Figure 40 - Tire curve for the values found by curve fitting.  $D=1.1233$ ,  $C=1.4897$ ,  $B=7.5318$

#### 4.5 Steering robot test 2

During all of the tests the asphalt was wet and during a few tests it was raining. Each test was carried out with two different tire models; the tire model that was estimated with a dry surface from the first test and is called “dry model,” and the model with reduced peak force capability, called “wet model”. Figure 41 and Figure 42 show the vehicle during testing with the robot, which already has been shown in Figure 34 above.



Figure 41. Entry of the double-lane change track where the vehicle is driven by the steering robot.



**Figure 42. Middle section of the double-lane change track where the vehicle is driven by the steering robot.**

The results from the second test vary significantly when outputs from cases, with various implemented features in the model, were tested. The input was the steering angle calculated by the optimization process. Input steering angles, simulated positions and positions at the double-lane change test track are shown for the nominal vehicle set-up for wet conditions in Figure 43-Figure 45 while the same is shown for dry conditions in Figure 46-Figure 48. All of the test cases can be found in the Appendix E – Measured data part 2. The legend in each figure denotes the code name of each test. As every model was tested twice, i.e. every test was run two times, two plots can be seen in each figure.

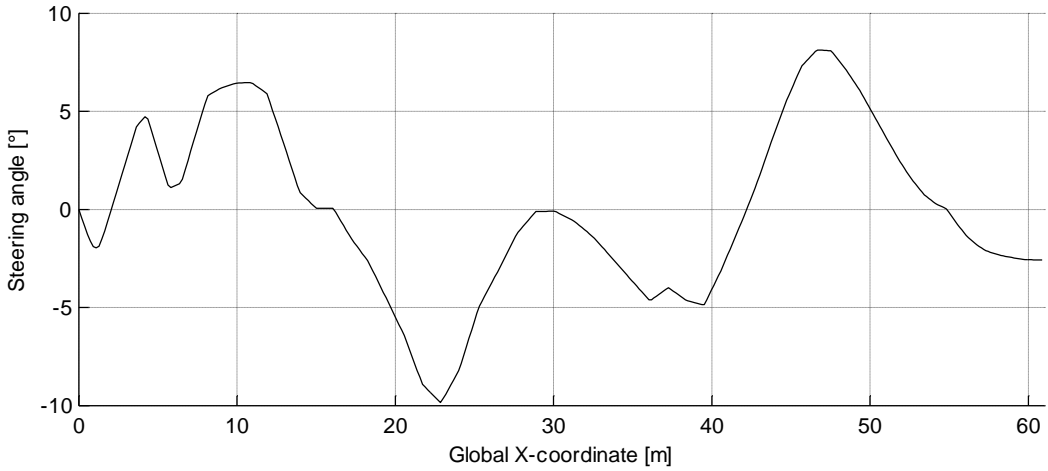


Figure 43. Steering angle simulation output along the double-lane change track for a model with nominal parameters in wet conditions.

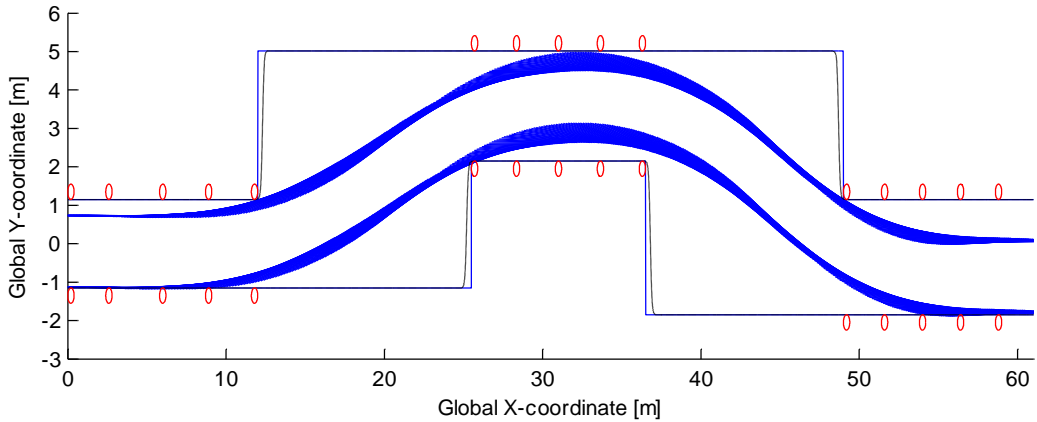


Figure 44. Simulation trajectory in the double-lane change track for a model with nominal parameters in wet conditions, also corresponding to the steering angles shown in Figure 43.

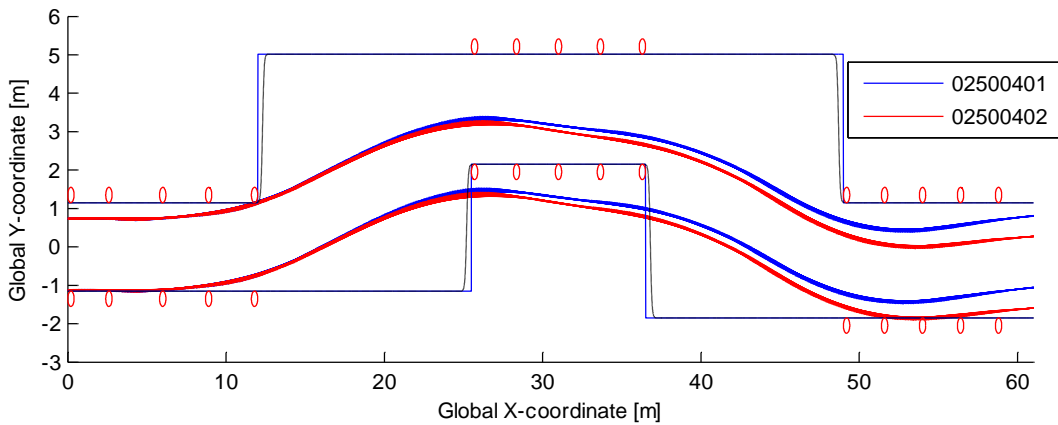


Figure 45. Real vehicle trajectory in the double-lane change track for a model with nominal parameters in wet conditions, also corresponding to the steering angles shown in Figure 43.

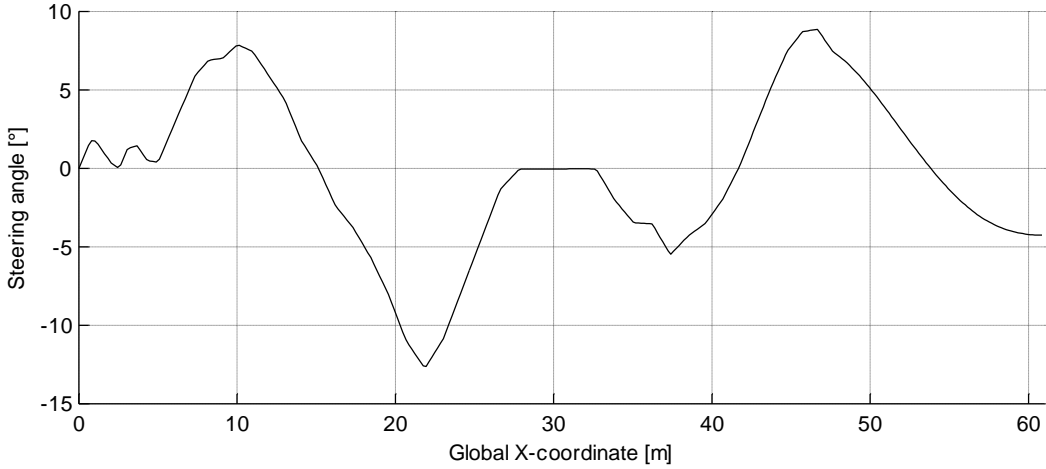


Figure 46. Steering angle simulation output along the double-lane change track for a model with nominal parameters in dry conditions.

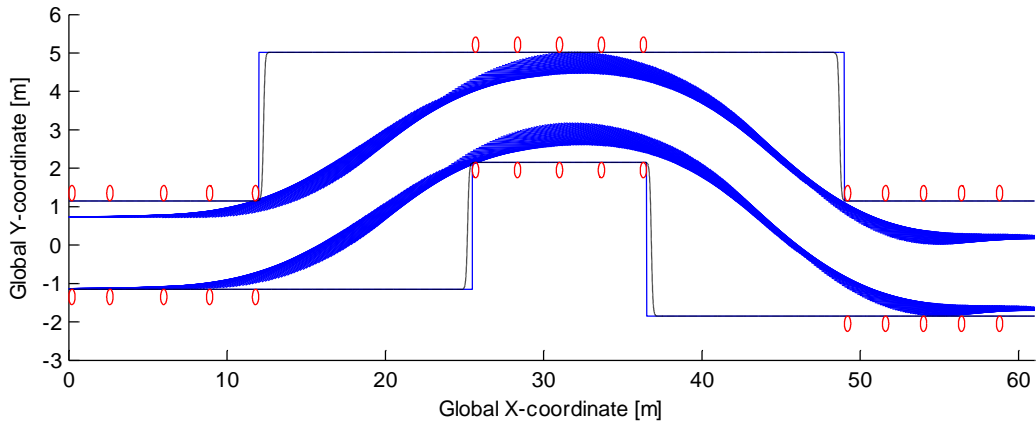


Figure 47. Simulation trajectory in the double-lane change track for a model with nominal parameters in dry conditions, also corresponding to the steering angles shown in Figure 45.

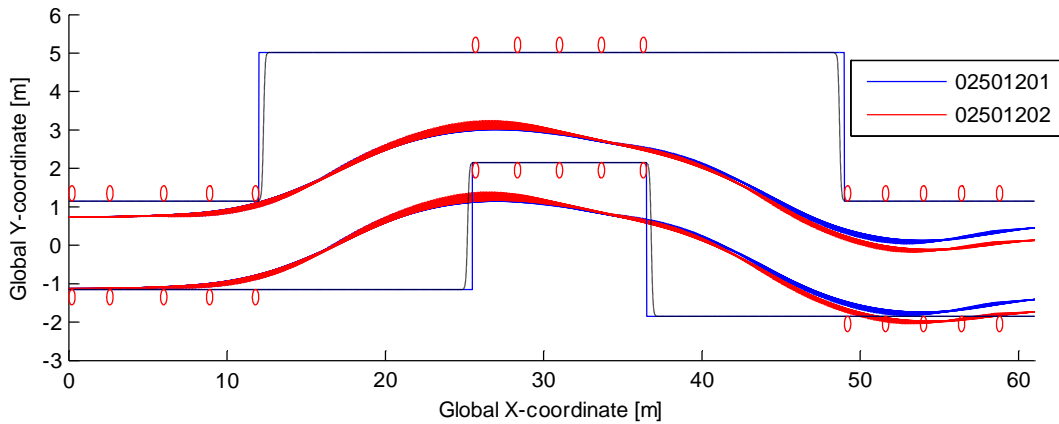


Figure 48. Real vehicle trajectory in the double-lane change track for a model with nominal parameters in dry conditions, also corresponding to the steering angles shown in Figure 45.

Since each figure depicts the same test run twice, it would be expected that the two curves, originating from the same control inputs (steering and initial travelling speed), would coincide; this is not the case. While the same steering inputs and travelling speed were fed to the robot, the vehicle was not on the same position on the track in every run. This indicates that the friction between the tires and the ground was varying. As it is shown in the figures, all of the passes regarded as most successful manage to clear the entry and the exit lane of the track, while crossing the lower part of lane B. A possible reason for such a phenomenon can be inappropriately modelled tires as well as an erroneous estimation of the yaw inertia. The vehicle does not turn as much as the model predicts both entering as well as exiting the second lane. This can be the case when the vehicle model assumed tires with higher cornering stiffness, and thus higher lateral force generation capability for the same steering angles, than the real ones. In addition, too low a yaw inertia in the model can also be responsible for such a behaviour.

In all of the cases of the most successful tests though, the fact that the vehicle passes the first and last lane of the track indicates a symmetry to the vehicle's trajectory, meaning that an appropriate correction to the steering angle's magnitude will approach the desired trajectory. This correction can result both from an improved tire model and/or by a more exact yaw inertia value.

## 4.6 Parameter study

Steering angles, possible maximum entry speeds and robustness, as it was defined in 3.9 Parameter study, for different scenarios are the main results that are presented for each parameter variation.

### 4.6.1 Mass

In Figure 49 below the dependency of the entry speed on the vehicle mass is shown. This study was performed by increasing the mass in steps while keeping every other parameter constant. It is clear that the entry speed tends to increase the larger the mass gets. At first, this might seem counterintuitive, since the mass is known to negatively affect the handling of a vehicle in general. The mass is the only parameter altered here, with everything else held constant; larger mass means that the normal forces on the wheels are greater and hence their ability to generate lateral forces is also increased. As the lateral force generation ability of the tires is of crucial importance in this double lane change manoeuvre, the increased mass has a positive effect on the vehicle's entry speed in the manoeuvre.

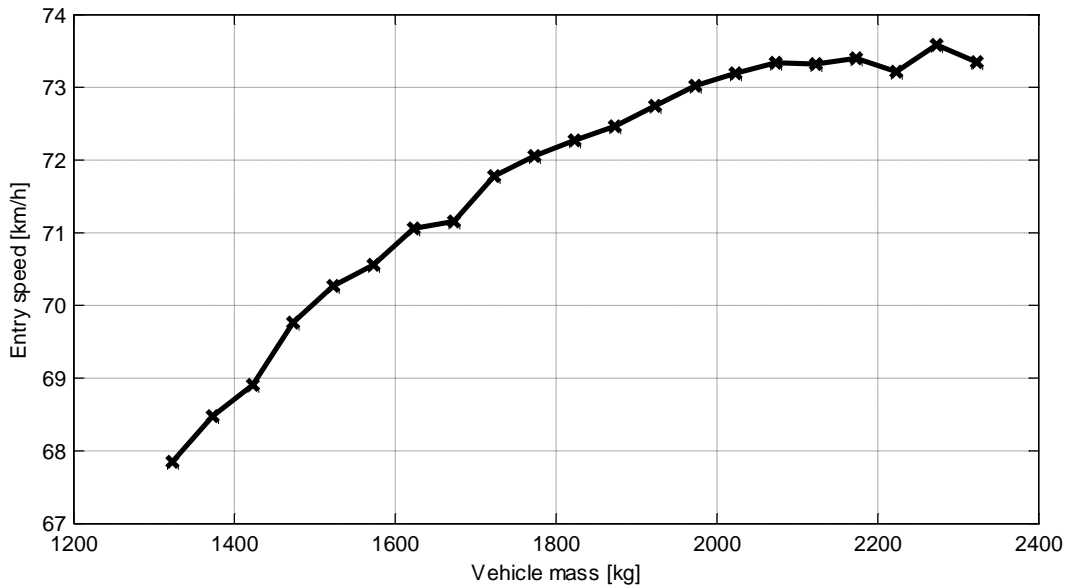


**Figure 49.** The effect of the vehicle's mass on its entry speed to the DLC test. The actual mass of the S60 was 1823kg.

In reality, vehicles with higher mass have usually higher moments of inertia, which practically means less agility. This happens because the increased mass is distributed among different parts of the vehicle. But in the case of this study, the mass, being the only parameter altered, is considered as if it is added only at the vehicle's centre of gravity (or it is distributed in such a way that the vehicle's moments of inertia remain unaffected), which means that the vehicle does not actually become less agile. The increased mass, with everything else being constant, has a positive effect on the vehicle's entry speed in the manoeuvre.

#### 4.6.2 Yaw inertia

The effect of the vehicle's yaw inertia on its entry speed at the manoeuvre is depicted in the Figure 50. In a similar manner with the mass study, the yaw inertia study was performed by increasing the yaw inertia value while keeping every other parameter at its nominal value. The tendency of the entry speed to get lower with increased yaw inertia is clear from the figure. Higher inertia means in practice that the vehicle tends to be less agile, and thus its ability to violently change direction is decreased. This results in a lower maximum possible entry speed.

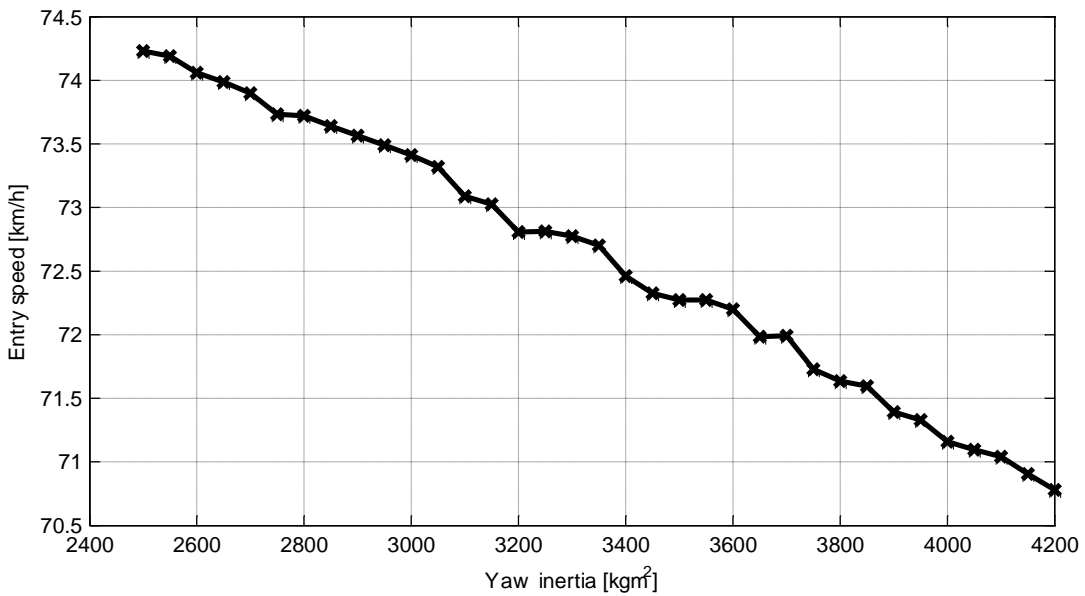


**Figure 50.** The effect of the vehicle's yaw inertia on its entry speed to the DLC test. The actual yaw inertia of the S60 was  $3500\text{kgm}^2$ .

Altering the yaw inertia without affecting any other vehicle parameter means that the mass, though remaining the same in total, is distributed in different ways. A lower value for the yaw inertia would mean that the mass concentrates more toward the vehicle's centre of gravity, while a higher value would mean the opposite. An example of different mass distributions as a means to alter the vehicle's moment of inertia is the various powertrain layouts. The most common layout, used in the majority of passenger cars, is the front-engine and front wheel drive vehicle that in general has a high yaw inertia value. Another layout, used often by more sporty cars, is the mid-engine rear wheel drive one that has a lower inertia value, which adds to the vehicle's agility.

Mass distribution is of crucial importance for the vehicle's handling characteristics, since, except for its effect on the vehicle's agility, it dictates its centre of gravity position, its understeer or oversteer behaviour, and hence its predictability and safety.

#### 4.6.3 Body width and length

The study of the effect of the body width and length of the vehicle on its entry speed resulted in entry speeds given by Figure 51 and Figure 52. From the graphs it is apparent that an increased vehicle width or length has a negative effect on its entry speed in the track.

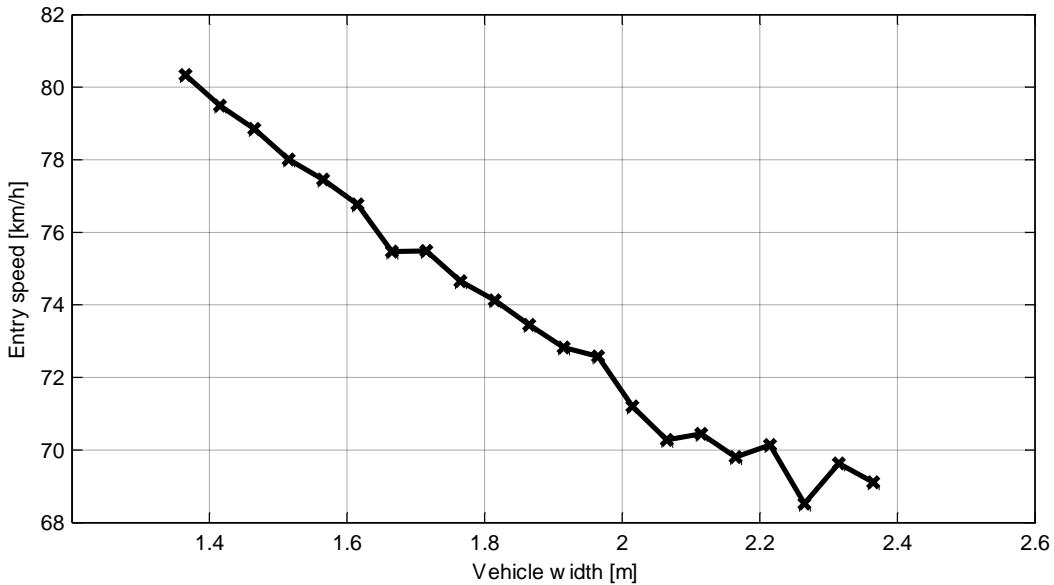


Figure 51. The effect of the overall vehicle width on the entry speed. The actual overall width for the S60 is 1.865m, without the rear view mirrors.

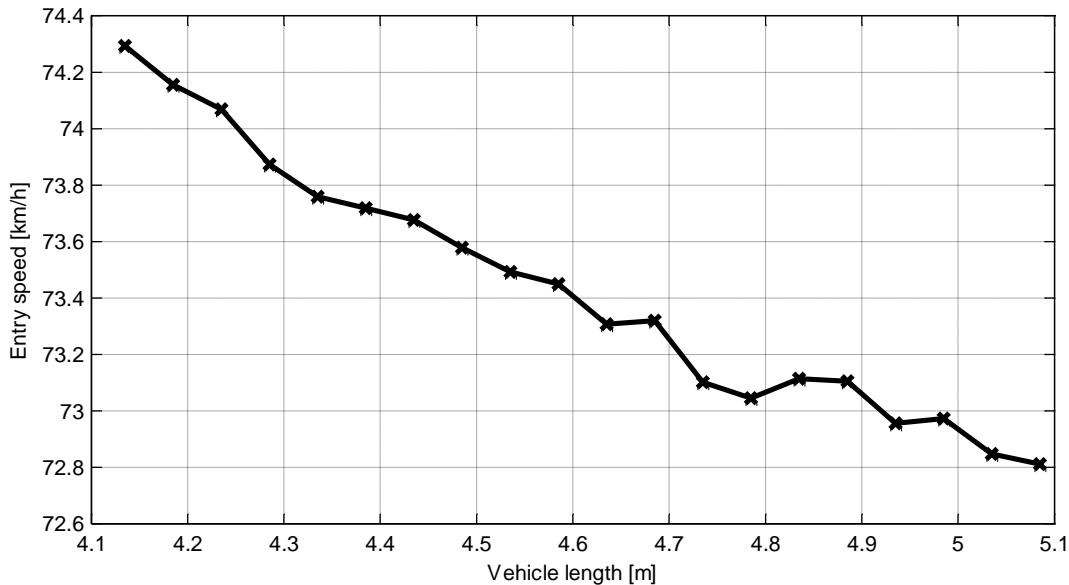
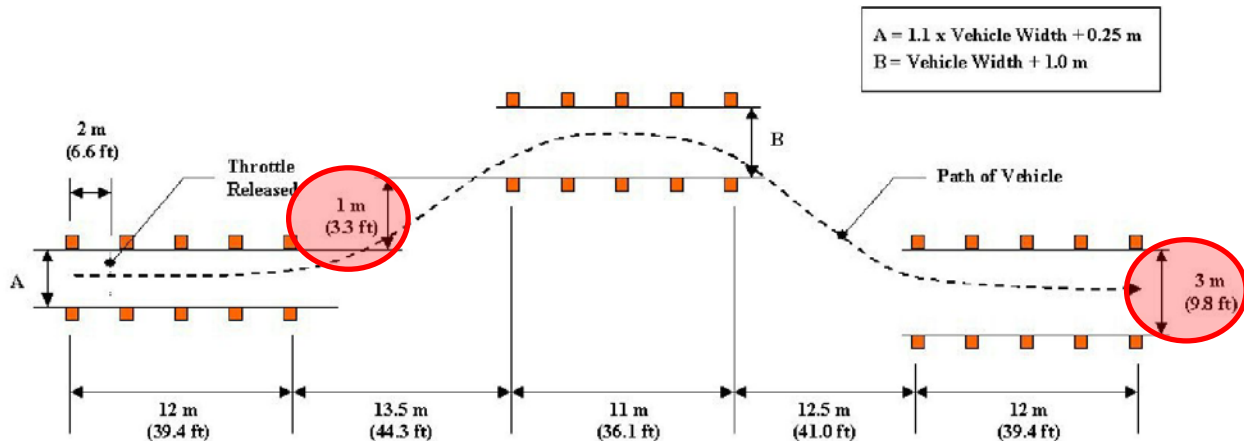


Figure 52. The effect of the overall vehicle length on the entry speed. The actual overall length for the S60 is 4.635m.

This result can be explained by the fact that a wider or longer vehicle has less space to move through when performing the manoeuvre. While this is clear for the case of the length, a closer look might be needed for the case of width, since a change in the track geometry takes place according to the vehicle's width (specifically the change in the first and second lane widths).

The lanes that are affected by the vehicle's body width are the A and B lane as named in Figure 53. Even though these lanes become wider for a wider vehicle, their in-between distance remains the same, which makes the transition from lane A to lane B and from lane B to lane C harder for a wider vehicle. In addition, lane C is always 3 meters wide, posing another restraint to the wider vehicles.



**Figure 53.** Wider and longer vehicles perform worse in regards of entry speed. Even though the width of lanes A and B becomes larger for wider vehicles, their in-between spacing remains the same. This also holds true for the spacing between lanes B and C. Additionally, lane C is always kept at 3 meters wide. The parts that pose those restrictions are marked in circles.

#### 4.6.4 Roll stiffness

The effect of roll stiffness was also studied by altering the front roll stiffness and the rear roll stiffness while keeping everything else in their nominal values. In Figure 54 the effect of the front roll stiffness on the entry speed can be seen and in Figure 55 the related steering wheel angles can be seen.

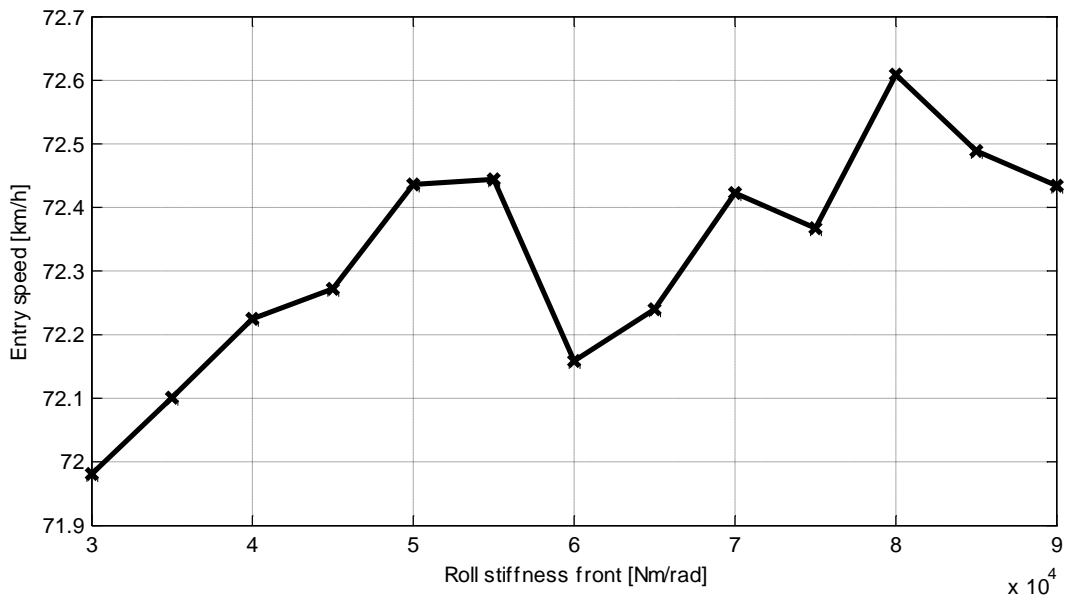


Figure 54. The effect of the front roll stiffness on the entry speed. The actual front roll stiffness used in this study was 45kNm/rad.

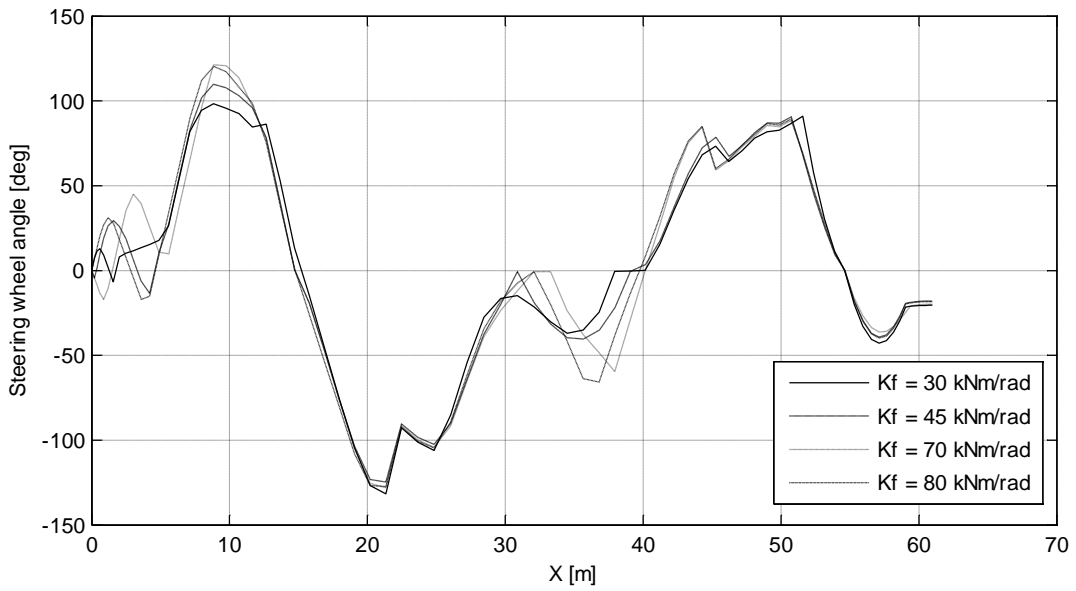


Figure 55. Steering wheel angle profiles for different front roll stiffness values.

Altering the front or rear roll stiffness does not seem to have a significant effect to the entry speed of the vehicle as one also studies Figure 56, which shows the effect of the rear roll stiffness on the entry speed, as well as Figure 57, which shows the corresponding steering wheel angles.

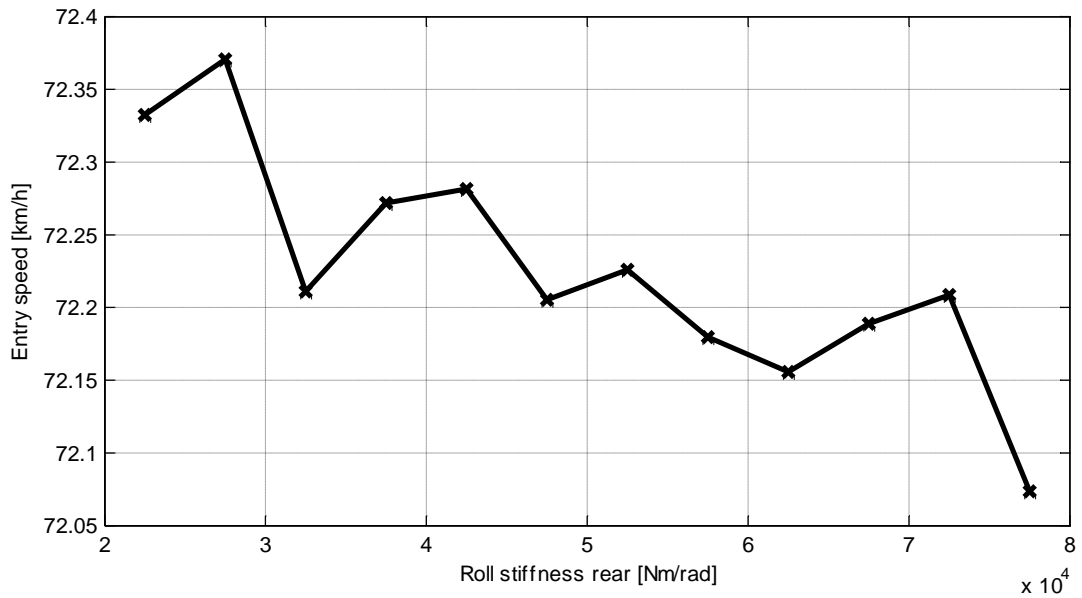


Figure 56. The effect of the rear roll stiffness on the entry speed. The actual rear roll stiffness used in this study was 37.5kNm/rad.

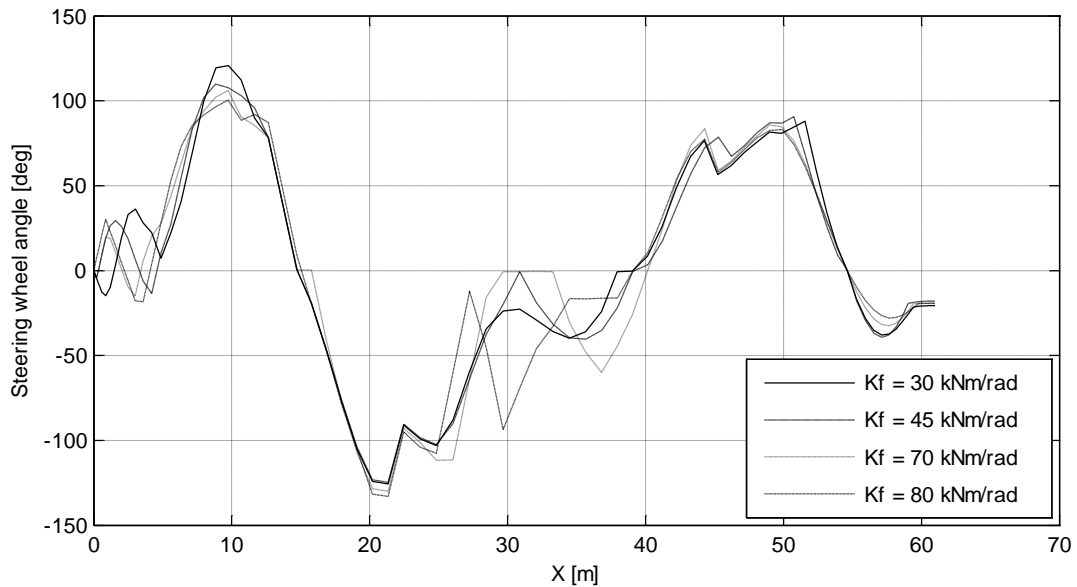


Figure 57. Steering wheel angle profiles for different rear roll stiffness values.

For reference, the corresponding steering wheel angle profiles are also plotted for some values of the roll stiffness. The biggest differences in the generated steering wheel angle profiles are observed around  $X = 0\text{--}2\text{ m}$ ,  $X = 10\text{ m}$ ,  $X = 30\text{--}35\text{ m}$  for both the cases of the front and rear roll stiffness studies. These areas define the entry to the double-lane change

track, the preparation for exit from the first lane (part A), and the middle/preparation for exit from the second lane (part B) respectively.

The entry part of the double-lane change track allows for some small steering action that can be utilized for braking by steering and this is a possible reason for which every steering angle profile begins with steering at the beginning. But the direction towards which this initial steering occurs affects the dynamics of the vehicle and therefore its future behaviour. The exit-from-the-first-lane and the middle/exit-from-the-second-lane parts are the parts where the vehicle is subjected to high lateral accelerations and corrections towards the desired path afterwards. During these parts the vehicle's roll stiffness distribution front/rear plays an important role since it affects its understeer or oversteer behaviour and therefore it should be handled differently, hence the differences in the steering wheel angle profiles.

As mentioned, the roll stiffness distribution has an effect on the vehicle's oversteer or understeer behaviour. In general, the end (front or rear) with the higher roll stiffness tends to lose traction earlier than the end with the lower roll stiffness. A vehicle with much higher roll stiffness on the rear will be oversteer while a vehicle with much higher roll stiffness on the front will be understeer. As an oversteer vehicle is unstable it is considered more unsafe for the driver and thus is generally undesired [24] [19]. According to the results of this roll stiffness study though, the vehicle's entry speed in the manoeuvre remains almost unaffected whether it is configured to be understeer or oversteer. This indicates that the controller is able to compensate for understeering or oversteering behaviour.

#### 4.6.5 Tire property changes

These results refer to changes of the magic formula's  $B$ ,  $C$  and  $D$  components and in Figure 58 all possible maximal entry speeds can be seen for all 47 successfully tested cases. In total 54 different cases were tested which implies that the optimization algorithm robustness for tire changes is 87 %.

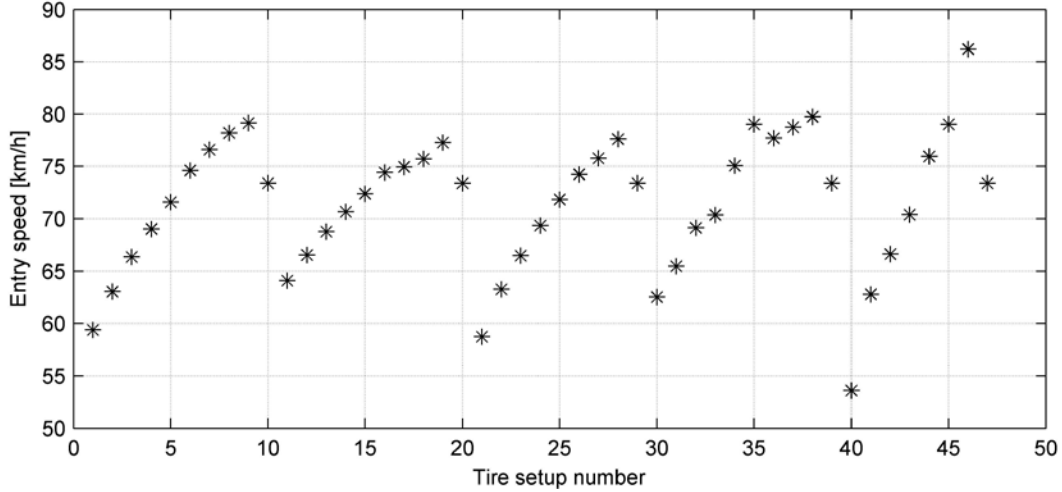


**Figure 58.** Maximal entry speed for all tested tire properties. Tire setup numbers 1-10 correspond to an equal relative increase of each tire parameter ( $B, C, D$ ), 11-20 correspond to a relative increase of  $B$ , 21-29 correspond to a relative increase of  $C$ , 30-39 correspond to a relative increase of  $D$  but with constant product  $B*C*D$  and 40-47 correspond to a relative increase of  $D$ . The range for each test is between 50-150 % of the parameter's nominal value.

It can be seen that all test cases except setup number 40 and 46 are in the same interval, meaning that an increase of the product  $B*C*D$  has approximately the same influence on the maximum entry speed that can be achieved as when changing only parameter  $B$  or  $C$ . Setups 40 and 46 both had a change of only the parameter  $D$  which implies that  $D$  has a larger impact on the result, something which could be expected as the vehicle should drive on its friction limits and  $D$  dictates the peak value for the tires. With a 50 % increase of  $D$  the entry speed increased 17.5 %, resulting in an entry speed of 86.2 km/h. If instead  $D$  decreased with 50 % the entry speed decreased with 27 %, resulting in an entry speed of 53.6 km/h. Steering angles corresponding to changes of parameter  $D$  can be seen in Figure 59.

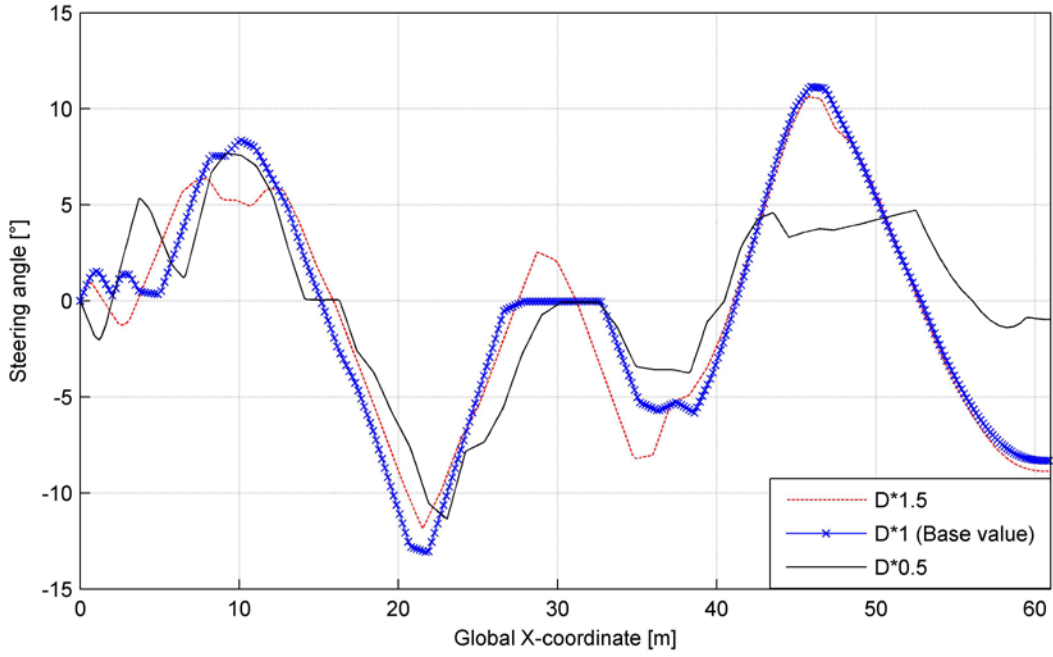


**Figure 59.** Steering angles in the case of the minimal, maximal and normal value for the parameter  $D$  in the tire magic formula.

At the parts of the track where the largest steering angles were present in the nominal case and in the case with extra high  $D$  value it can be seen that the low  $D$  value results in much lower steering magnitudes. A possible explanation for these lower magnitudes is the fact that the vehicle is also forced to drive slower and the whole manoeuvre becomes violent. It should also be noted that the steering angles are very equal between the normal case and a case of a 50% higher  $D$  value, thus for high enough  $D$  values the entry speed increases but the steering angles remain. That is also still the case if the total  $B*C*D$  product is held constant while  $D$  is changed, as can be seen in Figure 60.

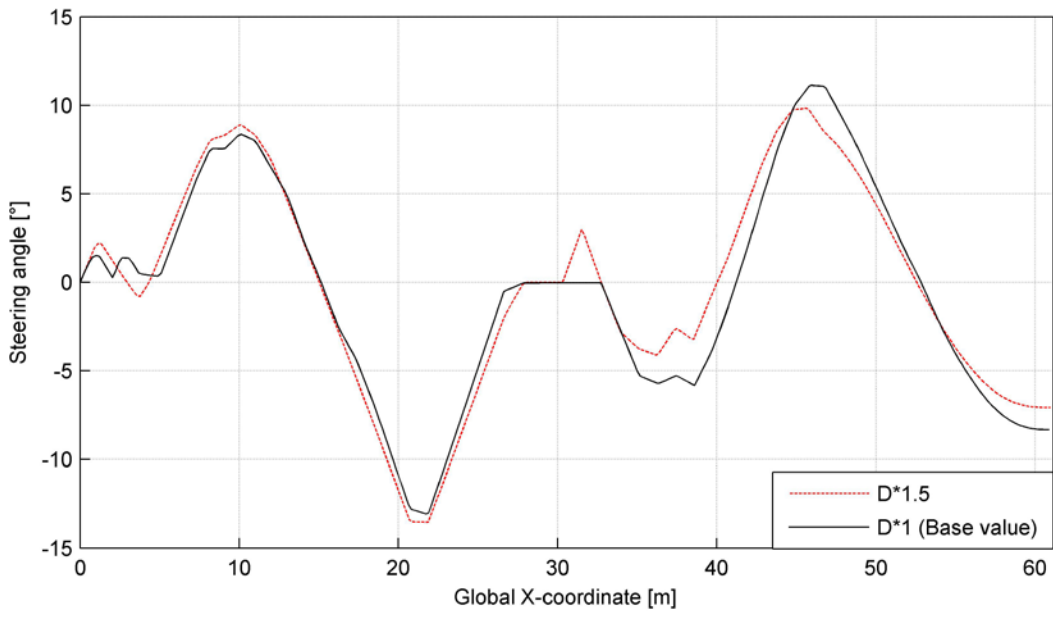


**Figure 60. Constant  $B*C*D$  product while changing  $D$ .**

There is even less difference between the maximum  $D$  value and the nominal case when the product  $B*C*D$  is held constant. No coupling can be seen between the  $D$  value and the magnitude of the steering angle as the line, that has the largest magnitude, is not always the same for all X-coordinates.

#### 4.6.6 ESC-characteristics variations

In total 600 different ESC characteristics were used, of which 52 cases could not be solved without lowering the increase of collocation points between two consecutive iterations, resulting in an ESC model robustness of 91 %. The entry speed, which could be achieved with each of these cases, can be seen in Figure 61.

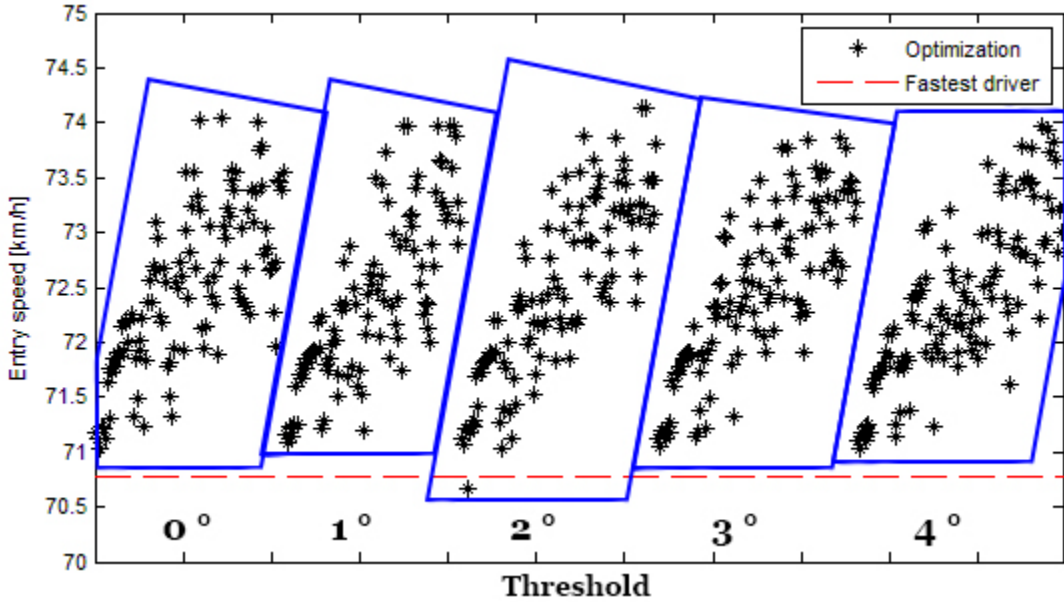


**Figure 61.** Illustration of the scattering in the maximum entry speeds that were achieved by the simulation for each of the five different groups. Each group corresponds to a different yaw rate error threshold for the ESC activation. For every group the activation torque and torque increase factor were varied and the result above was obtained.

In Figure 61 the resulting entry speeds are grouped; the difference between those groups is the yaw rate error threshold and although it does not have a high influence in the tested interval some differences can be seen. The threshold is  $0^\circ$  to the left and increasing  $1^\circ$  per group to the right; the  $2^\circ$  group is then found to be both the best and the worst<sup>24</sup>. The best, as well as the worst, ESC characteristics can be seen in Figure 62.

<sup>24</sup> “Best” is defined as the case where the highest entry speed is achieved while “worst” is defined as the opposite.

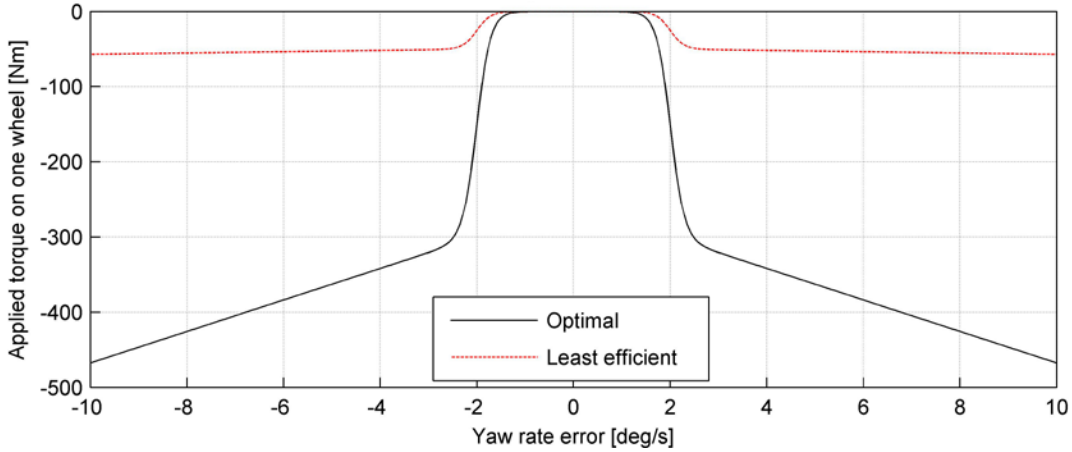


Figure 62. Best and least efficient ESC torque characteristics of those tested in this study. The optimal settings are a yaw rate error threshold of  $2^\circ$ , an activation torque of 300 Nm and a torque increase factor of 4. The least efficient ESC settings are a yaw rate error threshold of  $2^\circ$ , an activation torque of 50 Nm and a torque increase factor of 1. An infinite amount of combinations are possible to test.

An entry speed in the case of the best ESC settings, shown in Figure 62, was 74.1 km/h while the least efficient ESC settings implied that the entry speed could not be higher than 70.7 km/h which is 0.1 km/h less than without ESC. One may argue that the accuracy is not high enough to consider 0.1 km/h as a lower speed but it should be noted that there is a possibility as well that an ESC with the wrong settings is worse than not having it at all. Also the influence on the optimal steering angles can be seen by studying Figure 63. It can be seen in which sections the ESC was influencing the most by detecting the position where the difference is largest between the lowest and highest steering angles in the Figure 63.

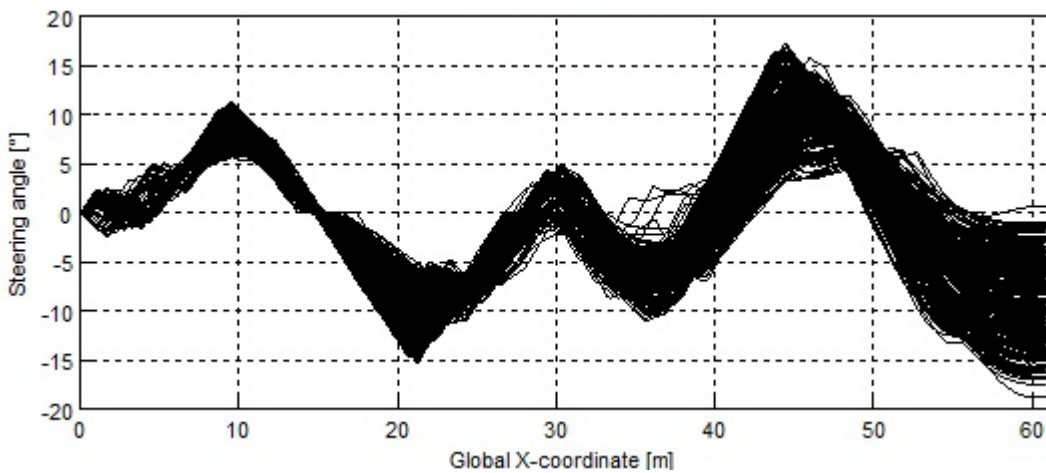
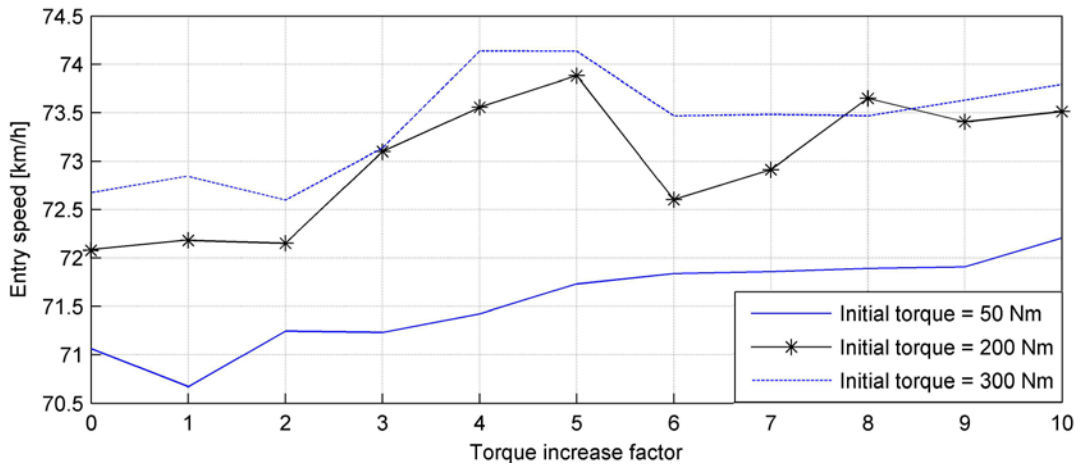


Figure 63. Resulting optimal steering angles for the 548 successful ESC combinations.

Note that some solutions have negative steering angles while other solutions have positive steering angles right after the start, but within the same magnitude interval. As the vehicle

just drives straight through that section it would be useful to reduce the speed before the cornering starts and as steering manoeuvres reduce the speed a steering angle in any direction of the same magnitude would produce a braking force. Depending on the ESC characteristics that were used, different yaw rate errors may be resulting in optimal braking torque on each wheel; the controller then compensates the steering angles in such a way that this yaw rate error is generated. Other ESC characteristic parameters were held at their nominal values while changing the torque increase factor for a few different initial torque values which resulted in the maximal entry speeds as given by Figure 64.



**Figure 64. Maximal entry speed as function of torque increase factor for three different values of initial torque at a yaw rate threshold of  $2^\circ$ .**

One can see the connection between the maximum entry speed that can be achieved and the ESC initial torque for most values of torque increase factor. The same was done for a few different yaw rate error threshold values instead of initial torque values in Figure 65.

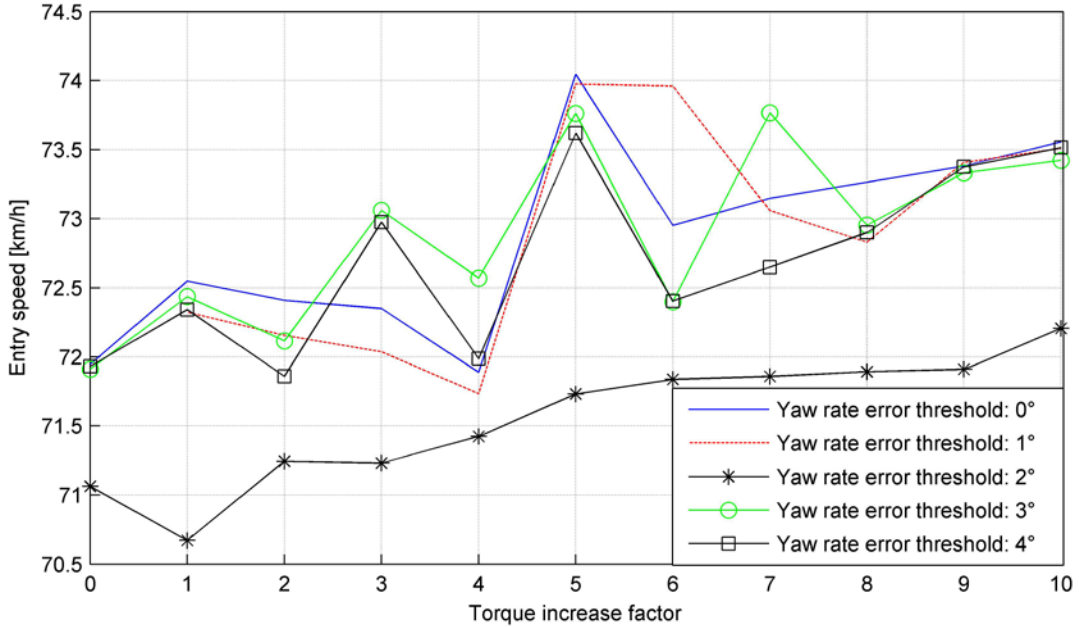


**Figure 65. Maximum entry speed as function of torque increase factor for yaw rate error thresholds between 0-5° at an initial torque of 200 Nm.**

It is clear that a yaw rate error threshold of 2° is the least efficient choice when the ESC is setup with an initial torque of 200 Nm but as was seen in Figure 61 one will be able to achieve the highest entry speed with a yaw rate threshold of 2°. That speed corresponds to the best ESC, which can be seen in detail in Figure 62.

#### 4.6.7 Influence of discretization

Optimal steering angles were calculated for a bicycle model with non-linear tires for different resolutions of the discretization, resulting in Figure 66.

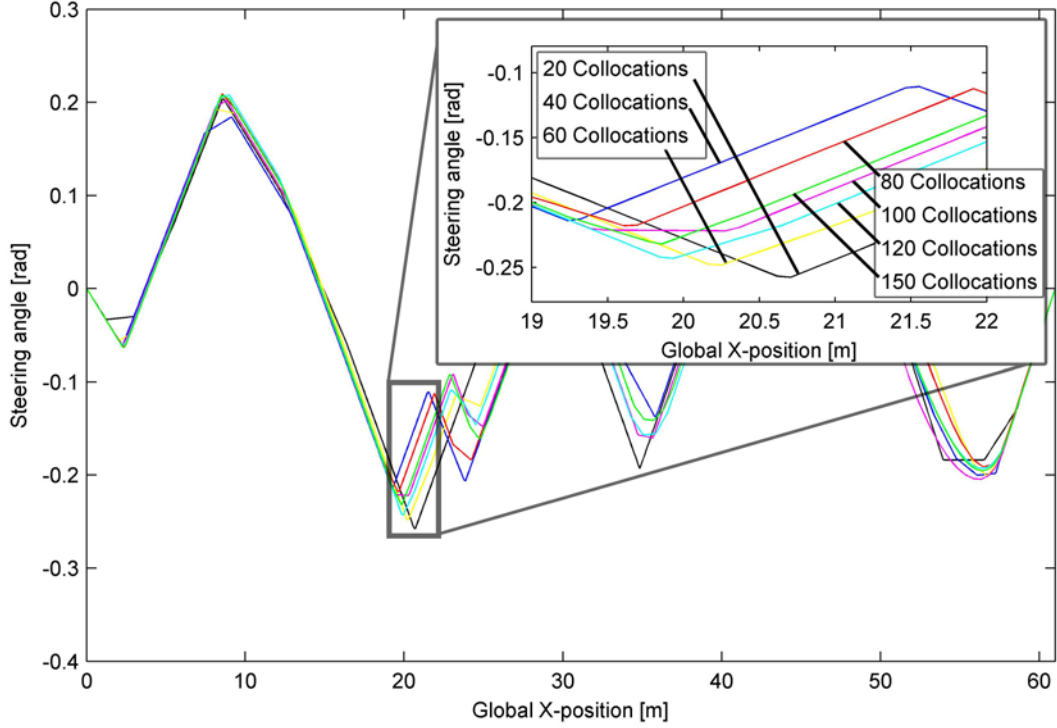


**Figure 66.** Optimized steering angle inputs with different number of collocation points. The magnification window shows a part of the result where the difference between the solutions is biggest.

One can see that the result coming from the discretization with the lowest resolution, 20 collocation points, is furthest away from the solution with 150 collocation points. Too few collocation points result in a solution which may miss to place a point where a steering angle change should occur in an ideal and continuous solution; in the beginning of the figure, at  $X = 2 \text{ m}$ , the 20 collocation points solution deviates from the others because there is no collocation point there. If the 150 collocation points' solution ( $\delta_{150}$ ) is set as reference the relative accumulated absolute error (Err), given by Eq. 127, for each of the other solutions can be studied in Figure 67.

$$Err = 1 - \frac{\int |\delta|}{\int |\delta_{150}|} \quad \text{Eq. 128}$$

w

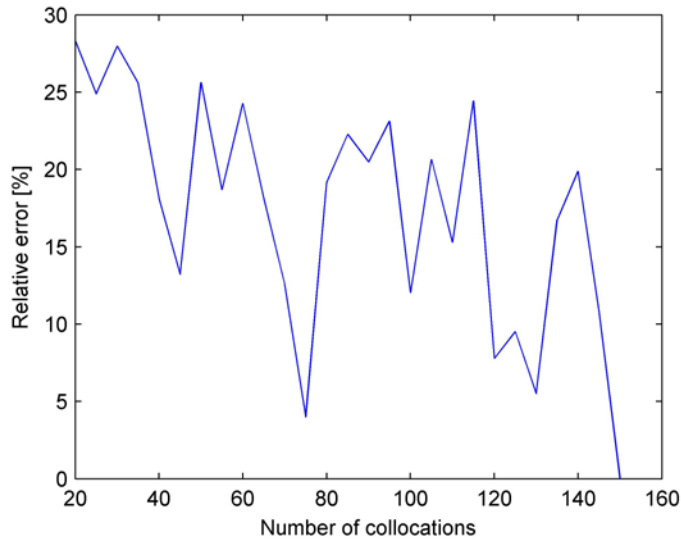


**Figure 67.** Relative accumulated absolute steering angle error for solutions with 20-150 collocation points in step of 5 collocation points. The 150 collocation point solution was set as the reference.

A decrease of the error can be seen the more collocation points are used, but the error is not always lower for each added collocation point. In the same manner as before, this can be explained by the distribution of the collocation points along the  $X$ -position in space. In the  $X$ -direction there might be some points where a change in the steering angle is critical, like for example the  $X = 2 \text{ m}$  position in Figure 66. If the distribution of the collocation points by the solver does not include these critical points, then the relevant important change in the steering angle will not be predicted, and therefore the error would be negatively affected. That “miss” of the important instants is declining the more collocation points are used, since the probability to miss the crucial parts decreases with more points, and will tend to zero as the collocation points tend to infinity, i.e. a continuous rather than a discrete solution. While the increase in the collocation points is therefore expected in general to decrease the error, it cannot serve as an absolute metric for the quality of the solution.

# 5 Discussion

This thesis investigated the generation of the optimal steering control input that facilitates the maximization of a vehicle's entry speed in the double-lane change manoeuvre. A two-track vehicle model was built in Matlab, where also various vehicle dynamics features were implemented. Also an ESC implementation was presented and was integrated into the vehicle model. The model, including the ESC, was subjected to an optimization process to obtain the corresponding optimal steering angles, using the optimization tool Tomlab.

During this study simplifications were made to a few of the modelled parts of the vehicle as well as the result was studied with various features implemented in the model. The possibility to use the suggested approach to solve the problem with other vehicles than the test vehicle was also investigated. These aspects of the study are discussed briefly in this chapter, providing our view on the process of creating a tool for an early development phase of a vehicle.

## 5.1 Vehicle dynamics and ESC modelling

The vehicle's dynamics were modelled by a two-track vehicle model which included features as roll stiffness, roll steer and camber gain. The effect of those features was studied and it was found that the controller is able to compensate for various stiffness and suspension compliance setups. For the tire modelling a simplified Magic formula was used and tire relaxation phenomena were also implemented. Obtaining accurate values for those features' parameters can be a cumbersome task, but a proper implementation of the tire model is of crucial importance when performing vehicle dynamics studies, especially on the vehicle's handling limits.

An ESC logic was constructed, which was demonstrating discontinuous behaviour that was needed to be approximated by a continuous one. A method for such an approximation was suggested and this method has also the potential to be used for the real vehicle's ESC. Such an application of the method would be an interesting continuation of this work. It would also be possible to investigate the ESC characteristics that are the optimal to use, as the short investigation in the parameter study shows. It is also of interest to optimize the ESC characteristics, not just for the case of this double-lane change manoeuvre, but also consider other scenarios as well.

## 5.2 Results

The trajectory deriving from the optimization process implies that the vehicle travels close to the first, second and fourth inner corner while being further out from the third corner. In sections A and C, as noted in Figure 53, the car travels as close as possible to the lower track boundary while the rear part of the car also travels as close to the upper track boundary as

possible in section B as was seen in Figure 26. Consequently, a simple model as the bicycle model might be enough if the trajectory is the searched result. Such a simple model can be solved fast and may even be used to calculate a new optimal trajectory even while the car is driving, implying potential real-time usage. However, Figure 23 showed that the bicycle model would be insufficient to predict the correct steering wheel angle inputs. An interesting fact is that an increasing number of collocation points can increase the accuracy but does not necessarily do so when comparing the accuracy done with two arbitrary numbers of points.

### 5.3 Parameter study and method robustness

The thesis evaluated the influence of different vehicle settings on the maximum entry speed for the double-lane change test. Parameters as the mass, the tires' cornering stiffness and the  $D$  value of the magic formula have a direct positive effect on the entry speed. On the other hand, parameters like the vehicle's body width and length and its yaw inertia have the opposite effect. The vehicle's roll stiffness on the front and rear axle did not seem to influence its ability to perform in the test, as the controller was able to compensate for understeer or oversteer behaviour.

ESC parameters that were studied were the yaw rate error activation threshold, the torque increase factor and the activation torque. No direct influence on the entry speed from one parameter alone, while keeping the others unchanged, was found. An increase or decrease to one parameter would invoke an increase or decrease to the entry speed depending on the values of the other two parameters.

Robustness of the optimization algorithm has been tested by performing the optimization with more than 780 different parameter settings with a total robustness of 92.3 %, without decreasing iteration steps manually. The method of manually changing the increase of the collocation points between two consecutive iterations was tested for solving a few random chosen cases out of the ones which did not converge, so as to also reach to an optimal solution. The confidence level to always solve the problem, for passenger cars and light commercial vehicles, is high if the solver is allowed to start with one of the solved cases as a guess and then make small changes to each parameter to reach the solution. The optimal method has though limitations; it cannot be guaranteed that it will converge for any vehicle, as there are more than  $10^{16}$  cases to solve if the parameters describing the vehicle are only changed between 10 values.

# 6 Recommendations

A few recommendations can be considered, deriving from the results from the optimization and from physical testing. Those are:

- **Vehicle dynamics model complexity;** can differ depending on the situation; if one would only be interested in the optimal trajectory it is recommended to use the bicycle model with non-linear tires. If the steering angle inputs are of interest the most time efficient solution without losing accuracy has been found to be the use of the two track model with an ESC present but without tire relaxation and instead lower the entry speed with 1 km/h due to the effect is was supposed to have.
- **New parameter estimation;** it was performed by curve fitting. More accurate methods, where standardized tests are performed for this purpose, exist. It is important to retrieve reliable information about the tire properties, preferably for various friction conditions (dry, wet, etc...). The tires play a significant role in the behaviour of the vehicle and a proper implementation is crucial for the model to have validity.
- **Appropriate physical testing;** should be done in conditions where the tire properties are estimated. The new results could then be used to either prove the model to be accurate enough or provide information about what happened when the model prediction was incorrect.
- **ESC implementation;** a more sophisticated ESC model which captures a “more” realistic ESC logic could be studied. The current ESC logic is a simple implementation of a basic ESC algorithm, where only one wheel at a time is braked. Production ESC systems can brake more than one wheel simultaneously in order to achieve some desired result. Also, it is possible to implement other control methods such as sideslip control into the ESC model [22].

# 7 Future Work

The current study depicted interesting areas for future research. A few suggestions for future work and continuation of this study are:

- **Improved vehicle model with constrained trajectory;** it was found that the *CoG* trajectory could be regarded as solved with only a bicycle model. Subsequently, it may be possible to solve the more complex model with that predetermined path, which would reduce the boundaries for the problem. The solution time may get shorter but more important; the robustness can increase if there would be less local minima in the solution space.
- **Real ESC integration;** two alternatives to optimize the problem with a real ESC are proposed.
  - Change the ESC algorithm in the vehicle to the same as in the optimal controller.
  - Use the method developed in this study to convert the real, discontinuous, ESC equations to equivalent continuous functions.
- **Close the loop;** the way the vehicle is driven in this thesis is open loop. The steering inputs are predetermined by an optimization process and then are fed to a steering robot to perform the manoeuvre. This method is prone to accumulating error. Discrepancies between the model and the real vehicle, as well as the testing surface, induce some errors at some points and these errors are transmitted to the rest of the future points in the trajectory. Any error induced accumulates, and the final result might be far from the model output. This kind of error can be dealt with by feeding back the output to a controller, which would then act appropriately in order to reduce it. This controller could be either a driver model included in the loop, or a software controller, which would act on top of the optimized steering input and add corrections to the steering angles in real time.
- **Expand the tool's functionalities;** upon successful extension of the vehicle model, to a degree where it actually produces high fidelity results, other dynamic manoeuvres recreating testing scenarios can be included. This way, a more complete view of the vehicle's dynamic and handling characteristics can be obtained, since the number of different tests gives a higher likelihood to capture the vehicle's capabilities (and mainly weaknesses). Such manoeuvres could be the ISO 3888 Part 1 test, slalom tests, or

manoeuvres where the objective would be the minimization of the traveling time in a track.

- **Reduction of solution time;** depending on the situation the user will use the optimization algorithm in, it may be necessary to improve the speed of the calculations. Since the same solver, SNOPT, was always called by the Tomlab optimization environment, one may call the solver manually to avoid the automated symbolic processing. Other programming languages, such as C/C++, could be used but require programming of the optimization algorithm used by Tomlab.

# 8 Nomenclature

Symbol	Description	Symbol	Description
$a$	Smoothness	$F$	Force
$T$	torque	$b$	Distance of rear axle from CoG
$m$	mass	$CoG$	Centre of gravity
$Y$	Global lateral coordinate	$f$	Distance of front axle from CoG
$X$	Global longitudinal coordinate	$I$	Moment of inertia
$\psi$	Yaw angle	$C_a$	Cornering stiffness
$\varphi$	Roll angle	$\alpha$	Slip angle (For the tires)
$\theta$	Pitch angle	$\beta$	Sideslip angle
$x$	Local longitudinal coordinate	$L$	Wheelbase
$y$	Local lateral coordinate	$K$	Roll stiffness
$z$	Local and global vertical coordinate	$e$	Roll centre height
$v$	Local velocity	$h_e$	CoG height over roll axis
$a_y$	Lateral acceleration	$a_x$	Longitudinal acceleration
$\omega$	Rotational speed	$r$	Wheel radius
$W$	Distance from CoG to side	$B$	Magic formula stiffness factor
$C$	Magic formula shape factor	$D$	Magic formula peak factor
$\mu$	Friction coefficient	$s$	Resultant tire slip
$\tau$	Relaxation time constant	$L_{relax}$	Relaxation length
$\varepsilon$	Camber angle	$\gamma$	Inclination angle
$C_\gamma$	Camber stiffness	$R$	Turn radius
$M$	Yaw torque	$A$	Area
$K_{us}$	Understeer gradient	$J$	Objective function
$t$	Time	$W_\delta$	Weighting factor for steering rate influence on objective function

<b>Index</b>	<b>Description</b>	<b>Index</b>	<b>Description</b>
<i>tb</i>	Track boundary	<i>i</i>	Front and Rear
<i>fr</i>	Front right	<i>j</i>	Left and Right
<i>fl</i>	Front left	<i>x</i>	Longitudinal direction
<i>rr</i>	Rear right	<i>y</i>	Lateral direction
<i>rl</i>	Rear left	<i>z</i>	Vertical direction
<i>init</i>	Initial value	<i>r</i>	right
<i>if</i>	Increase factor	<i>l</i>	left
<i>tr</i>	track	<i>eff</i>	effective
<i>d</i>	desired	<i>w</i>	Brake disc
<i>g</i>	Initial guess value		

# 9 References

- [1] "How is ESC tested," Euroncap, [Online]. Available: <http://www.euroncap.com/Content-Web-Page/bf07c592-4f87-404e-bb06-56f77faee5a2/esc.aspx>. [Accessed 6 November 2013].
- [2] ISO Copyright Office, "International Standard, ISO 3888-2 manual," Geneve, 2002.
- [3] D. Katzourakis, "Optimal Steering Control Input Generation for Vehicle's Entry speed Maximization in a Double-Lane," Volvo car corporation PVV, Göteborg, 2013.
- [4] J. A. Snyman, Practical mathematical optimization, p.2-5, Springer Science+Business Media, inc, 2005.
- [5] J. Nocedal and S. J. Wright, Numerical Optimization, New York: Springer Science+Business Media, Inc, 1999.
- [6] P. E. Rutquist and M. M. Edvall, "PROPT - Matlab Optimal Control Software," Tomlab optimization, Västerås, 2010.
- [7] TESIS DYNAware GmbH, "TESIS DYNAware," TESIS DYNAware GmbH, 2013. [Online]. Available: <http://www.thesis-dynaware.com/en.html>. [Accessed 17 June 2013].
- [8] VI-grade engineering software & services, "VI-GRADE VI-car realtime," VI-grade engineering software & services, 7 May 2013. [Online]. Available: [http://www.vi-grade.com/index.php?pagid=vehicle\\_dynamics\\_carrealtime](http://www.vi-grade.com/index.php?pagid=vehicle_dynamics_carrealtime). [Accessed 3 July 2013].
- [9] Modelon AB, "Jmodelica.org," [Online]. Available: <http://www.jmodelica.org/faq/18>. [Accessed 22 November 2013].
- [10] Mathworks, "MATLAB The Language of Technical Computing R2013a," Mathworks, 8 March 2013. [Online]. Available: <http://www.mathworks.se/products/matlab/>. [Accessed 3 July 2013].
- [11] Tomlab Optimization, "TOMLAB Optimization," Tomlab Optimization, 8 August 2012. [Online]. Available: <http://tomopt.com/tomlab/>. [Accessed 3 July 2013].
- [12] K. Holmström, "The TOMLAB Optimization Environment in Matlab," Mälardalen

University, Västerås, 1999.

- [13] P. E. Gill, W. Murray and M. A. Saunders, "User's Guide for SNOPT Version 7: Software for Large-Scale Nonlinear Programming," Stanford University, Stanford, 2008.
- [14] MSC Software, "ADAMS/Car," MSC Software, 29 January 2013. [Online]. Available: <http://www.mscsoftware.com/product/adamscar>. [Accessed 3 July 2013].
- [15] Esteco SpA, Esteco SpA, 4 March 2013. [Online]. Available: <http://www.esteco.com/modefrontier>. [Accessed 3 July 2013].
- [16] Mathworks, "Documentation Center Optimization Toolbox," Mathworks, 8 March 2013. [Online]. Available: <http://www.mathworks.se/help/optim/>. [Accessed 3 July 2013].
- [17] Tomlab Optimization, "Matlab Symbolic Optimization Modeling," Tomlab Optimization, 8 August 2012. [Online]. Available: <http://tomsym.com/index.html>. [Accessed 3 July 2013].
- [18] K. L. Dmitrey, "OpenOpt," 15 June 2013. [Online]. Available: <http://openopt.org>Welcome>. [Accessed 17 June 2013].
- [19] Royal Institute of Technology, vehicle engineering department, "Vehicle Dynamics Course Compendium," Lars Drugge, Stockholm, 2011.
- [20] G. Rill, Road Vehicle Dynamics: Fundamentals and Modeling, Bosa Roca: CRC Press, 2011.
- [21] M. Mitschke and H. Wallentowitz , Dynamik der Kraftfahrzeuge, 4. Auflage., Berlin and Heidelberg: Springer, 2004.
- [22] R. Rajamani, "Vehicle Dynamics and Control," New York, Springer Science+Business Media, Inc, 2006, pp. 221-256.
- [23] Royal Institute of Technology, vehicle engineering department, "Vehicle Components KTH Course Compendium," Lars Drugge, Stockholm, 2010.
- [24] W. F. Milliken and D. L. Milliken , "Race vehicle dynamics," *Society of Automotive Engineers International*, 1995.

- [25] D. I. Katzourakis, Writer, *Automotive Crash Safety; Active and Passive Safety Systems - Lecture 6: Electronic Stability Control*. [Performance]. Delft University of Technology Biomechanical Engineering, 2009.
- [26] H. B. Pacejka, Tire and Vehicle Dynamics, Society of Automotive Engineers, 2002.
- [27] E. Bakker, L. Lidner and H. Pacejka, "A New Tire Model with an Application in Vehicle Dynamics Studies," *Society of Automotive Engineers*, no. 890087, 1989.
- [28] E. Velenis, D. Katzourakis, E. Frazzoli, P. Tsiotras and R. Happée, "Steady state drifting stabilization of RWD vehicles," *Control Engineering Practice*, no. 19, pp. 1363-1376, 2011.
- [29] E. Bakker, L. Nyborg and H. Pacejka, "Tyre modelling for use in vehicle dynamics studies," *Society for Automotive Engineers*, no. 870421, 1987.
- [30] Modified, "Modified - Tech Articles - Performance Tire Buyers Guide - Photo 20," [Online]. Available: [http://www.modified.com/tech/modp-0906-performance-tires-buyers-guide/photo\\_20.html](http://www.modified.com/tech/modp-0906-performance-tires-buyers-guide/photo_20.html). [Accessed 7 November 2013].
- [31] T. D. Gillespie , "Fundamentals of vehicle dynamics," *Society of Automotive Engineers*, 1992.
- [32] J. C. Dixon, Tires, Suspension, and Handling, 2:nd Edition, Society of Automotive Engineers, 1996.
- [33] J. Jerrelind, J. Edrén, S. Li, M. M. Davari, L. Drugge and A. Stensson, "Exploring active camber to enhance vehicle performance and safety," *The International Association for Vehicle System Dynamics*, 2013.
- [34] I. J. M. Besselink, A. J. C. Schmeitz and H. B. Pacejka. , "An improved Magic Formula/Swift tire model that can handle inflation pressure changes," *Vehicle System Dynamics*, vol. 48, no. 1, pp. 337-352, 2010.
- [35] H. J. Forster, "Der Fahrzeugfuhrer als Bindeglied Zwischen Reifen," *Fahrwerk und Fahrbahn, VDI berichte*, no. 916, 1991.
- [36] A. T. Van Zanten, R. Erhardt, G. Pfaff, F. Kost, H. Uwe and T. Ehret, "Control Aspects of the Bosch-VDC," *Proceedings of the International Symposium on Advanced Vehicle Control*, vol. 1, pp. 573-608, 1996.
- [37] S. V. Drakunov, B. Ashrafi and A. Rosiglioni, "Yaw Control Algorithm via Sliding Mode

- Control," *Proceedings of the American Control Conference*, pp. 580-583, 2000.
- [38] K. Uematsu and J. C. Gerdes, "A Comparison of Several Sliding Surfaces for Stability Control," *Proceedings of the International Symposium on Advanced Vehicle Control (AVEC)*, 2002.
- [39] K. Yi, T. Chung, J. Kim and S. Yi, "An Investigation into Differential Braking Strategies for Vehicle Stability Control," *Proceedings of the Institution of Mechanical Engineers, Part D: Journal of Automotive Engineering*, vol. 217, pp. 1081-1093, 2003.
- [40] T. Yoshioka, T. Adachi, T. Butsuen, H. Okazaki and H. Mochizuki, "Application of Sliding Mode Control to Control Vehicle Stability," *Proceedings of the International Symposium on Advanced Vehicle Control (AVEC)*, pp. 455-459, 1998.
- [41] J. J. E. Slotine and W. Li, *Applied Nonlinear Control*, Prentice Hall, 1991.
- [42] H. E. Tseng, B. Ashrafi, D. Madau, T. A. Brown and D. Recker, "The Development of Vehicle Stability Control at Ford," *IEEE/ASME Transactions on Mechatronics*, vol. 4, no. 3, pp. 223-234, 1999.
- [43] Y. Fukada, "Slip Angle Estimation for Vehicle Stability Control," *Vehicle Systems Dynamics*, vol. 32, pp. 375-388, 1999.
- [44] Y. A. Ghoneim, W. C. Lin, D. M. Sidlosky, H. H. Chen, Y. K. Chin and M. J. Tedrake, "Integrated Chassis Control System to Enhance Vehicle Stability," *International Journal of Vehicle Design*, vol. 23, no. 1/2, pp. 124-144, 2000.
- [45] B. Niessen, S. Jansen, I. Besselink, A. Schmeitz and H. Nijmeijer, "An enhanced generic single track vehicle model and its parameter identification for 15 different passenger cars. AVEC paper," in *The 11th International Symposium on Advanced Vehicle Control*, Seoul, 2012.
- [46] J. T. Betts, *Practical Methods for Optimal Control Using Nonlinear Programming*, Philadelphia: Society for Industrial and Applied Mathematics (SIAM), 2001.
- [47] D. Katzourakis, Driver steering support interfaces near the vehicle's handling limits., Delft: CPI Koninklijke Wöhrmann, 2012.
- [48] A. Nozad, M. Lidberg, T. Gordon and M. Klomp, "Optimal path recovery from terminal understeer," in *The International Association for Vehicle System Dynamics*, 2011.

- [49] J. H. Yung-Hsiang and J. C. Gerdes. , "The Predictive Nature of Pneumatic Trail: Tire Slip Angle and Peak Force Estimation using Steering Torque," *Advanced Vehicle Control*, 2008.
- [50] P. Sundström, M. Jonasson, J. Andreasson, A. Stenson Trigell and B. Jacobson, "Path and control optimisation for over-actuated vehicles in two safety-critical maneuvers," in *Advanced Vehicle Control*, Loughborough, 2010.
- [51] D. D. MacInnis, W. E. Cliff and K. W. Ising , "A Comparison of Moment of Inertia Estimation Techniques for Vehicle Dynamics Simulation," *Society of Automotive Engineers*, no. 970951, 1997.
- [52] H. B. Pacejka, "Tyre Models for Vehicle Dynamics Analysis," Delft, 1993.
- [53] Volvo Cars, "Volvo S60 vehicle Kinematics and Compliance Datasheet," Volvo Cars, Gothenburg, 2009.
- [54] H. B. Pacejka, *Tyre and Vehicle Dynamics*, 2:nd edition, Oxford: Society of Automotive Engineers International, 2005.
- [55] Robert Bosch GmbH, *Bosch Automotive Handbook* 7th edition., Society of Atomotive Engineers, 2007.
- [56] "RT3000 Family," OXTS Inertial + GPS, [Online]. Available: <http://www.oxts.com/products/rt3000-family> . [Accessed 6 November 2013].
- [57] D. I. Katzourakis, E. Velenis, D. A. Abbink, R. Happee and E. Holweg, "Race-Car Instrumentation for Driving Behavior Studies," *IEEE Transactions on Instrumentation and Measurement*, vol. 61, no. 2, 2012.
- [58] W. F. Milliken, D. L. Milliken and M. Olley, "Chassis Design: Principles and Analysis," *Society of Automotive Engineers*, 2002.
- [59] ISO Copyright Office, "ISO 3833:1977 Road vehicles -- Types -- Terms and definitions," Geneve, 2002.

# A – ISO 3888 description

The ISO 3888 Part 2-Obstacle avoidance is a dynamic process during which the vehicle is driven closed loop in a severe lane change manoeuvre such that high alternate lateral accelerations will be produced. It concerns passenger cars and light commercial vehicles up to 3500kg and involves rapidly driving from an initial lane to another parallel lane and then back to the initial one, so to recreate an obstacle avoidance scenario. During the manoeuvre no cone marking the track should be displaced for the pass to be considered as valid. The results of this test serve as a subjective evaluation of the vehicle's lateral dynamics and road holding ability. The test track that defines the manoeuvre can be seen below.

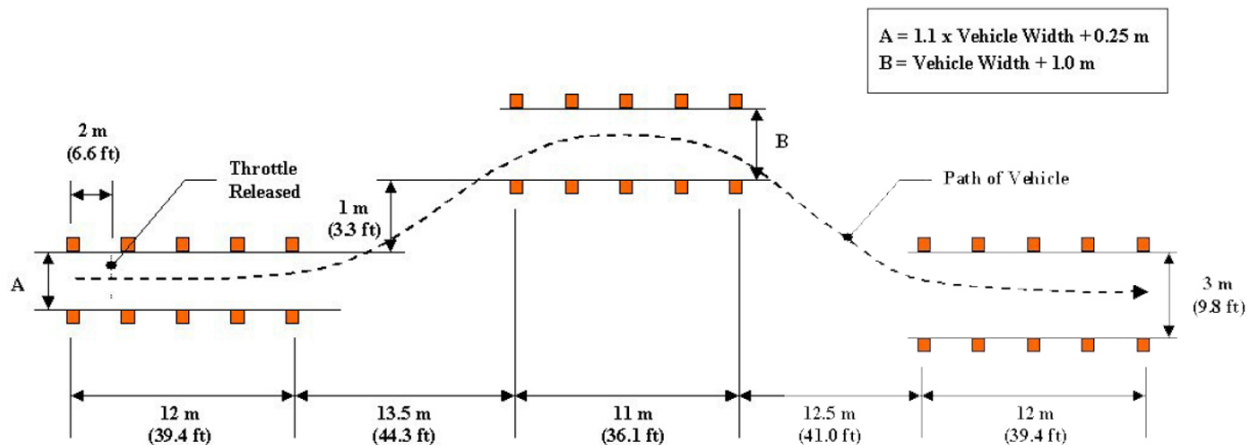


**Figure A 1. ISO 3888 part 2 double-lane change track illustration.**

The track sizing is vehicle dependent as can be seen above where the width of the initial lane A and the second lane B is calculated, as noted in the figure's legend. The value of *VehicleWidth* is the tested vehicle's overall width without the rear-view mirrors. The geometry differs only in regards of the lane widths though, as the length of the lanes and their in-between spacing remains the same.

Driving should be performed with the highest gear that guarantees a minimum of 2000rpm of engine speed and vehicles with automatic gearbox should have the selector placed in the drive (D) position. The vehicle enters the track in lane A and after a distance of 2m the throttle is released<sup>25</sup> where after the remainder of the track is driven in the throttle release

<sup>25</sup> While the ISO 3888 Part 2 document does not make any direct reference to whether the clutch should be disengaged or not, one may argue that since there is a reference to the engine speed at the entry point, it is implied that the clutch should remain engaged. In that case some engine braking is expected. In this thesis though, no such phenomenon is modelled, and the test is simulated as if the clutch is disengaged, i.e. no powertrain effects at all. This allows a clearer picture of the vehicle's dynamic behaviour that comes from its chassis and ESC setup since it isolates it from external (i.e. powertrain) influences.

position, without any braking action. Only the steering wheel is being controlled by the driver and the vehicle's longitudinal speed is measured at the end of section A, that is at  $X = 12\text{ m}$  in the track.

It should be noted that this is a test that best suits subjective rather than objective evaluation of the vehicle's lateral dynamics characteristics. This is due to the fact that different drivers, with different skills, choose different paths and strategies to drive through the track so the measured speeds are considerably scattered, in spite of the velocity measurement taking place at the end of section A as a means of reducing this effect.

# B – Test vehicle

The vehicle used during all physical testing and as an example when performing the optimization of the steering angles is described below.

**Table B 1. Test vehicle nominal parameters.**

Parameter description	Value
Model name	Volvo S60 T5 automat, year model 2009
Weight during testing (driver + equipment)	1823 kg
Curb weight (Standard equipment, full tank of fuel and no driver)	1635 kg
Gross weight	2060 kg
Yaw moment of inertia	2500 kgm <sup>2</sup>
Width (excluding mirrors)	1865 mm
Length	4635 mm
Distance of front wheel from mass centre	1854 mm
Distance of rear wheel from mass centre	2781 mm
Distance to the right track from mass centre	793.5 mm (Estimated to mass in middle)
Body length in front of the front wheels	929.5 mm (Estimated to equal as in the rear)
Front wheels track width	1588 mm
Rear wheels track width	1586 mm
Height of centre of mass	500 mm
Front roll centre height	120 mm
Rear roll centre height	240 mm
Front roll stiffness	45 000 Nm/rad
Rear roll stiffness	37 500 Nm/rad
Rolling friction coefficient	0.013
Air drag coefficient	0.28
Frontal area	2.27 m <sup>2</sup>
Maximum steering angle	31 °
Maximum steering angle rate	720 °/s
Steering ratio	14.95
Front roll steer coefficient	0.123
Rear roll steer coefficient	0.007
Pneumatic trail a linear range	1/30 m
Wheel radius	316 mm
Wheel width	200 mm
Magic formula, B	7.5418
Magic formula, C	1.4887
Magic formula, D	1.1233
Tire relaxation length	300 mm

## C – Measured data part 1

Despite that the robot couldn't perform the manoeuvre exactly in the way specified it performed a part of the manoeuvre at an entry speed of 74.3 km/h when the ESC was activated, which can be seen in Figure C 1.

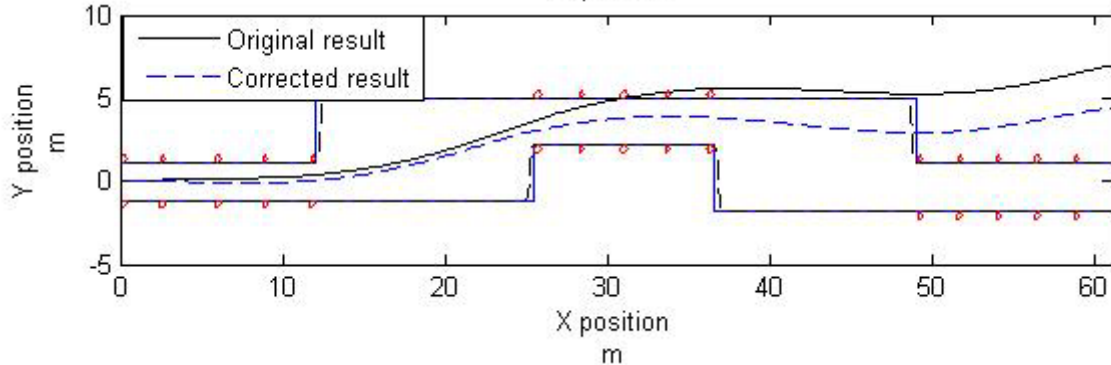


Figure C 1. Resulting coordinates for the vehicle's centre of gravity along the track when the model demanded larger steering angles as well as higher steering angle rates than was physically possible with the test vehicle. The solid line use the start of the measurement as zero position while the dashed line has a corrected coordinate system with  $-2.8^\circ$  and 2.11 m shifted X-position zero point; a correction which was based on where the steering wheel started to move compared to the input signal.

Below follows measured steering angles, yaw angles and speed for the first physical testing, which was carried out to validate the model. The position of the reference cones was not recorded during the measurement, for this reason all the results are presented both with the start of the recording as reference position as well as a correction based on a comparison of the steering angle input and the actual steering angle as shown in Figure C 2.

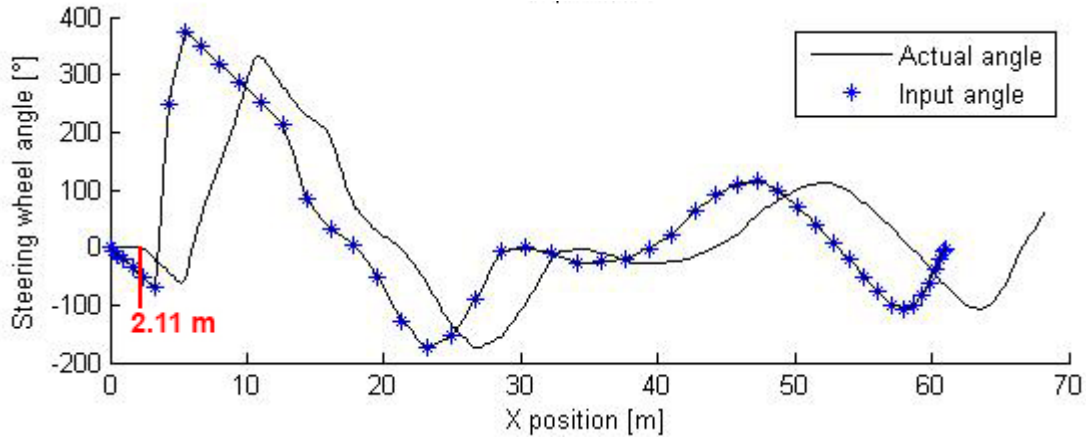


Figure C 2. Input steering wheel angle and actual performed steering wheel angle.

The corrections made for Figure C 3 and Figure C 4 are a shift of -2.11 m of the X-position as well as turning the coordinate system  $-2.8^\circ$  to make the actual yaw angle match the expected yaw angle at the initial position.

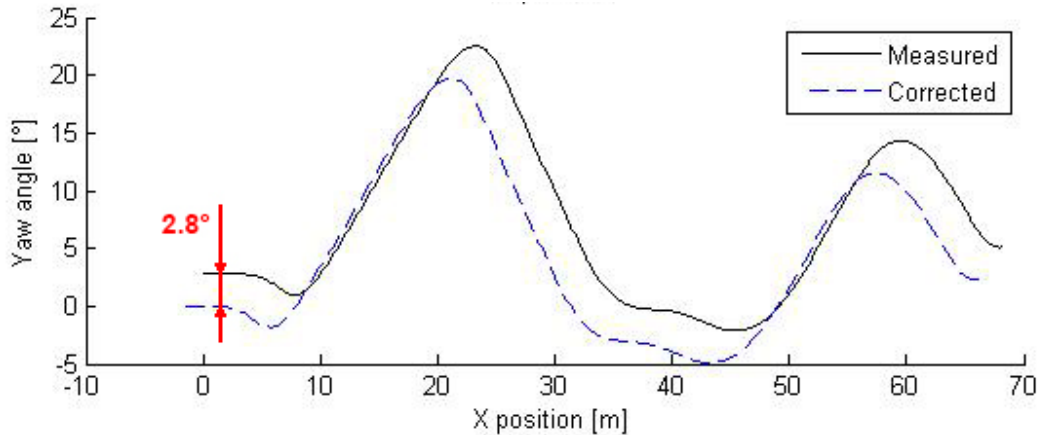


Figure C 3. Measured and corrected yaw angle.

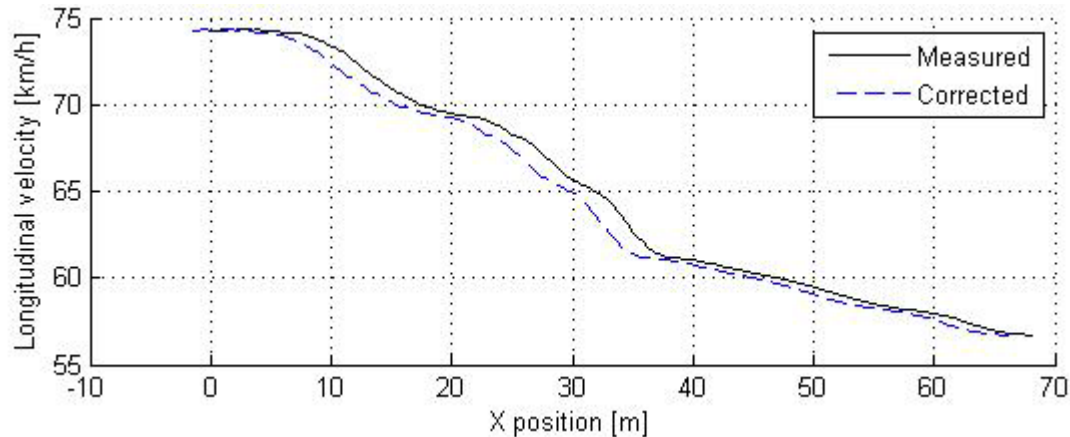


Figure C 4. Longitudinal velocity and corrected longitudinal velocity.

# D – Test 2 manoeuvre test list

These testing scenarios were performed, in total 24 robot driven scenarios and 2 human driven scenarios. Each robot driven test was performed twice and was carried out at approximately the same position at Volvo Hälleröd proving ground brake and handling track.

1. Measured vehicle weight, 1836 kg.
2. Activated ESC tests with steering robot
  - a.  $\dot{\psi}_t = 2$ ,  $T_{gain} = 200\text{Nm}$ ,  $T_{if} = 5$ , Entry speed= 72.8 km/h No tire relaxation, Entry speed = 73.6 km/h
  - b.  $\dot{\psi}_t = 2$  ,  $T_{gain} = 200\text{Nm}$ ,  $T_{if} = 10$ , Entry speed= 73.6 km/h No tire relaxation, Entry speed = 73.6 km/h
  - c.  $\dot{\psi}_t = 2$  ,  $T_{gain} = 100\text{Nm}$ ,  $T_{if} = 5$ , Entry speed= 72.3 No tire relaxation, Entry speed = 72.3 km/h
  - d.  $\dot{\psi}_t = 0$  ,  $T_{gain} = 200\text{Nm}$ ,  $T_{if} = 5$ , Entry speed= 73.8 km/h No tire relaxation, Entry speed = 74.1 km/h

2.1 Wet alternative (In case of wet asphalt D is reduced by 30% but BCD is the same)

- a. No tire relaxation, Entry speed = 65.9 km/h
- b. No tire relaxation, Entry speed = 66.0 km/h
- c. No tire relaxation, Entry speed = 64.9 km/h
- d. Yaw-threshold 0 degree model,  $T_{gain} = 200\text{Nm}$ ,  $T_{if} = 5$ , Entry speed= 66.5 km/h No tire relaxation, Entry speed = 67.0 km/h

3. Deactivated ESC tests with steering robot

- a. Most detailed model, Entry speed = 69.5 km/h
- b. Skip tire relaxation and wheel kinematics, Entry speed = 70.8 km/h
- c. Bicycle model with magic formula, Entry speed = 68.5 km/h

3.1 Wet alternative (In case of wet asphalt D is reduced by 30% but BCD is the same)

- a. Most detailed model, Entry speed = 62.7 km/h

- b. Skip tire relaxation and wheel kinematics, Entry speed = 63.1 km/h
  - c. Bicycle model with magic formula, Entry speed = 60.4 km/h
4. Human driver, deactivated ESC, cone track
    - a. Record the first left and last left cone, the distance should be long between the cones in order to get high track angle accuracy
    - b. Measure the track width in each section
    - c. Note in which maximum entry speed a driver could go through the track without hitting any cone.
  5. Human driver, activated ESC, cone track
    - a. Note in which maximum entry speed a driver could go through the track without hitting any cone.

# E – Measured data part 2

In this appendix a figure for the resulting position along the track for each of the tests can be seen. Figure E 1-Figure E 8 show results with the approximated wet tire model as described in 4.5 Steering robot test 2 while Figure E 9-Figure E 18 show results when using the normal model.

## *Wet tests*

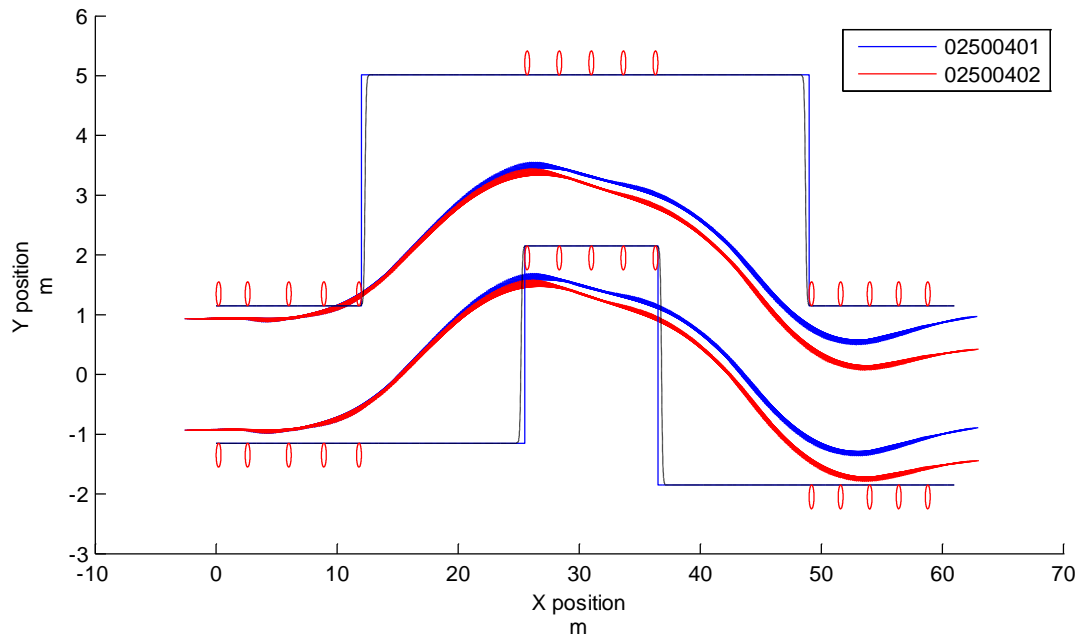
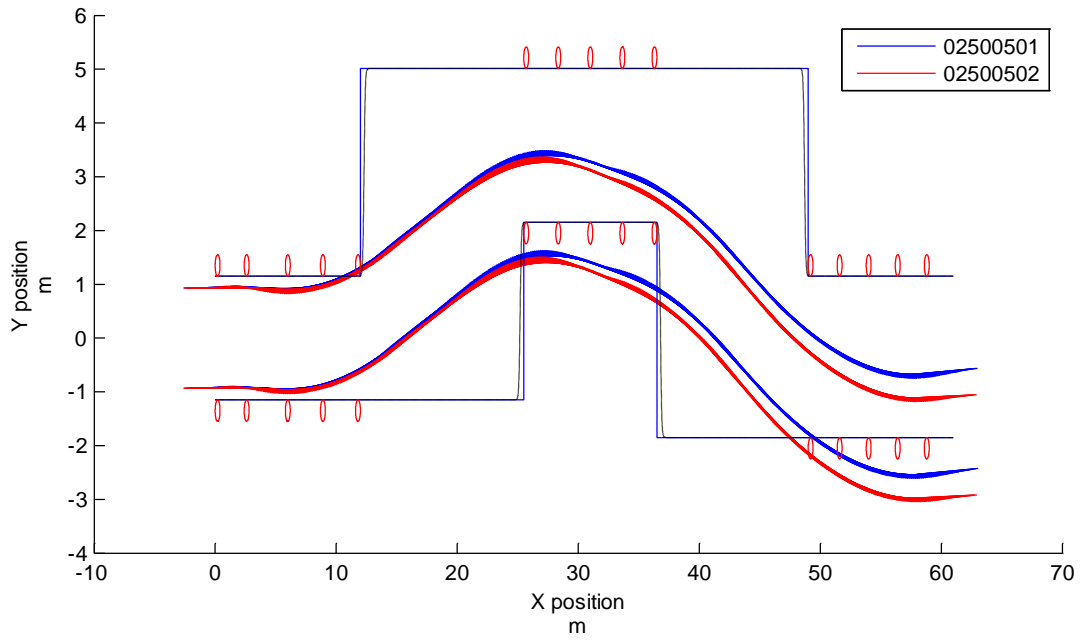
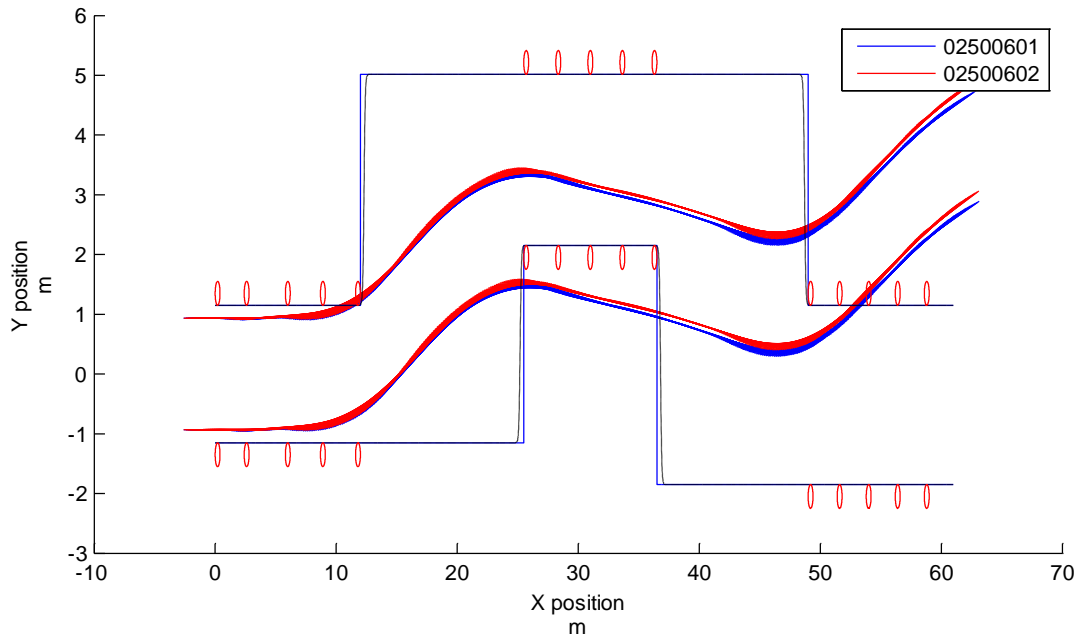


Figure E 1. Two track model with ESC implemented; threshold of  $2^\circ$ , activation torque of 200 Nm and torque increase factor of 5. The vehicle parameters were set to their nominal values.



**Figure E 2.** Two track model with ESC implemented; threshold of  $2^\circ$ , activation torque of 200 Nm and torque increase factor of 10. The vehicle parameters were set to their nominal values.



**Figure E 3.** Two track model with ESC implemented; threshold of  $2^\circ$ , activation torque of 100 Nm and torque increase factor of 5. The vehicle parameters were set to their nominal values.

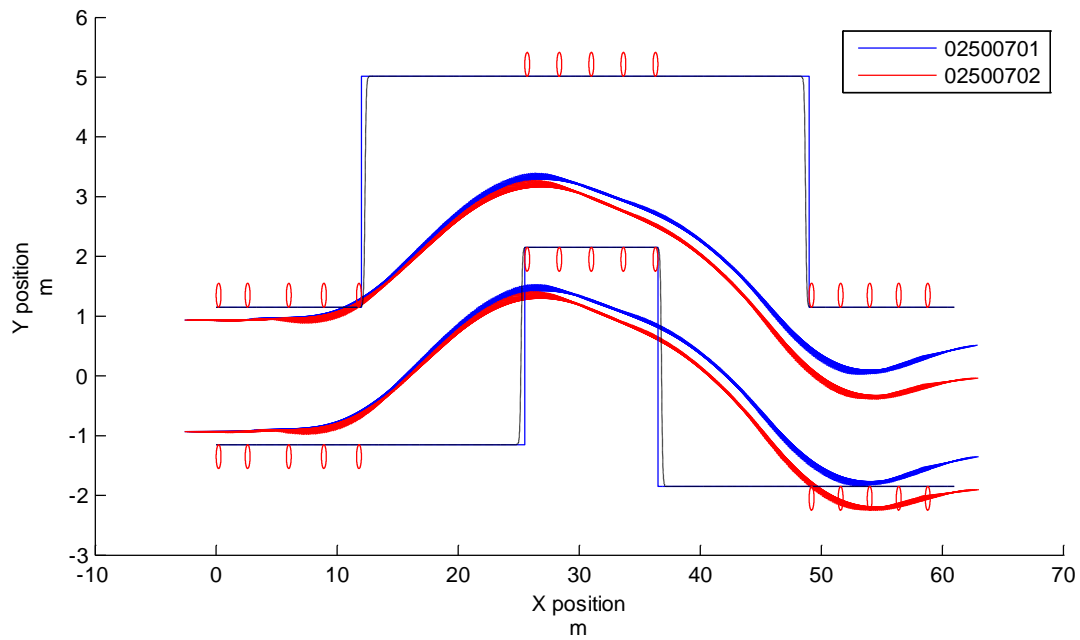


Figure E 4. Two track model with ESC implemented; threshold of  $0^\circ$ , activation torque of  $200 \text{ Nm}$  and torque increase factor of  $5$ . The vehicle parameters were set to their nominal values.

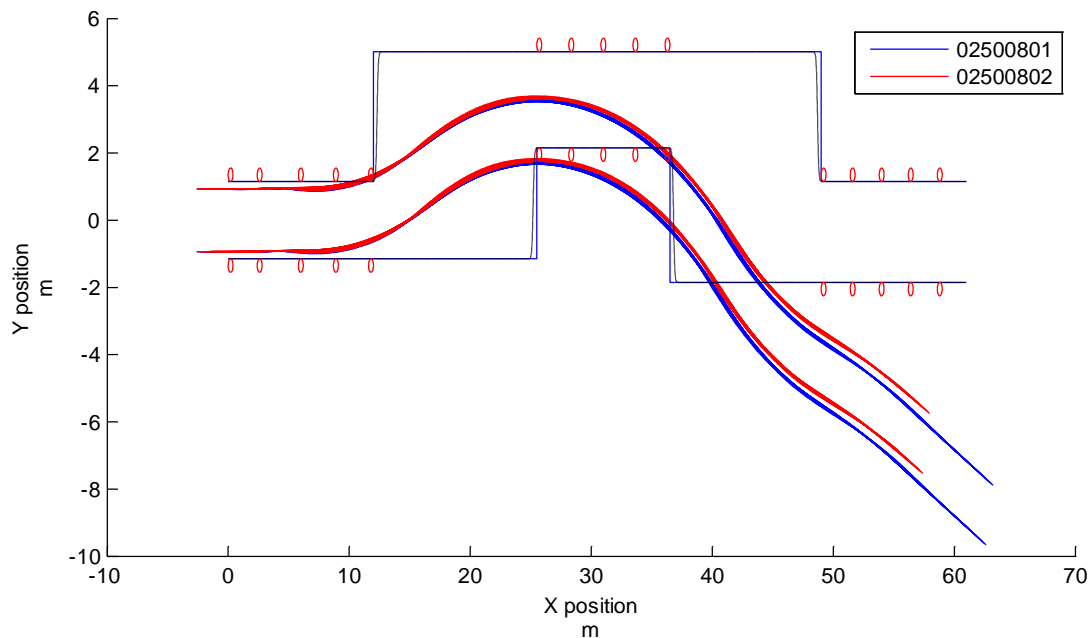
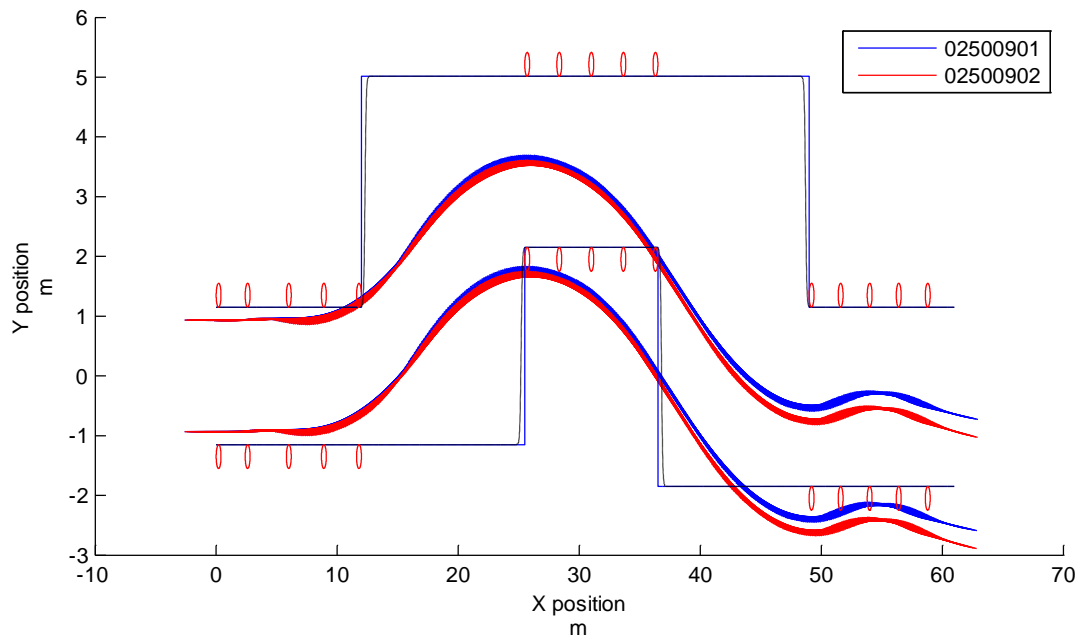
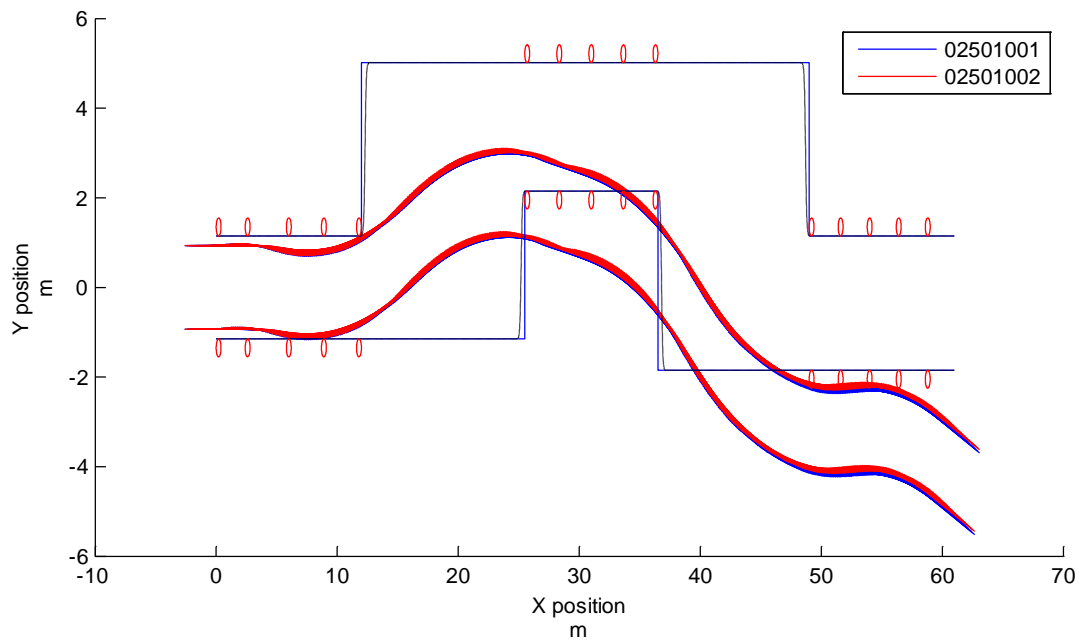


Figure E 5. Two track model with wheel kinematics, tire relaxation and no ESC, the vehicle parameters were set to their nominal values.



**Figure E 6.** Two track model with wheel kinematics and no ESC, the vehicle parameters were set to their nominal values.



**Figure E 7.** Bicycle model with Magic formula tires, the vehicle parameters were set to their nominal values.

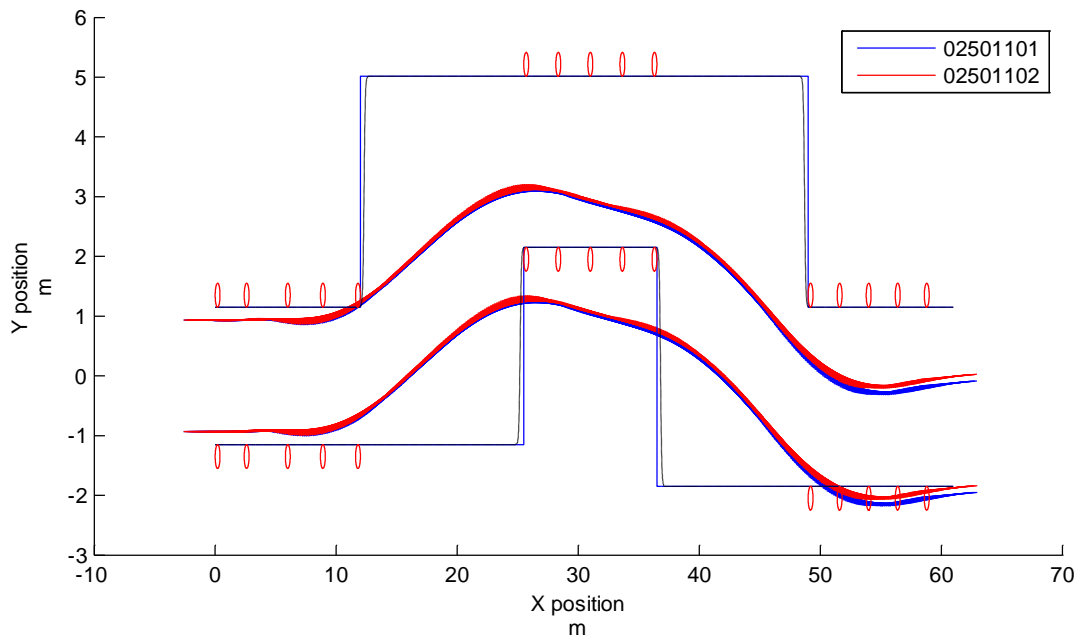


**Figure E 8.** Two track model with tire relaxation and ESC implemented; threshold of  $0^\circ$ , activation torque of 200 Nm and torque increase factor of 5. The vehicle parameters were set to their nominal values.

#### Dry tests

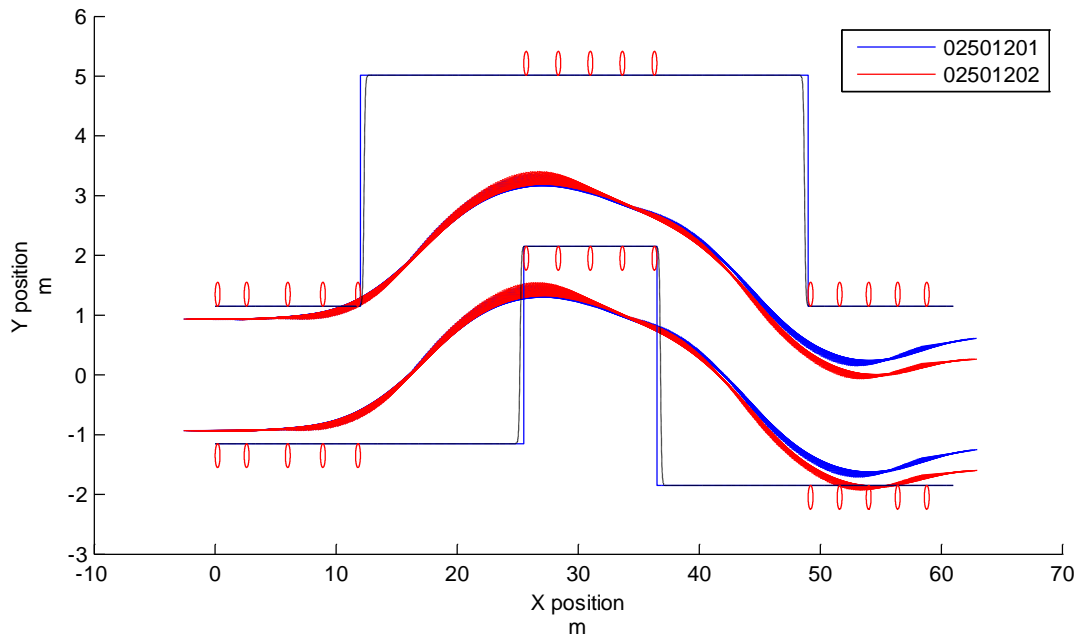


**Figure E 9.** Two track model with ESC implemented; threshold of  $2^\circ$ , activation torque of 200 Nm and torque increase factor of 5. The vehicle parameters were set to their nominal values.

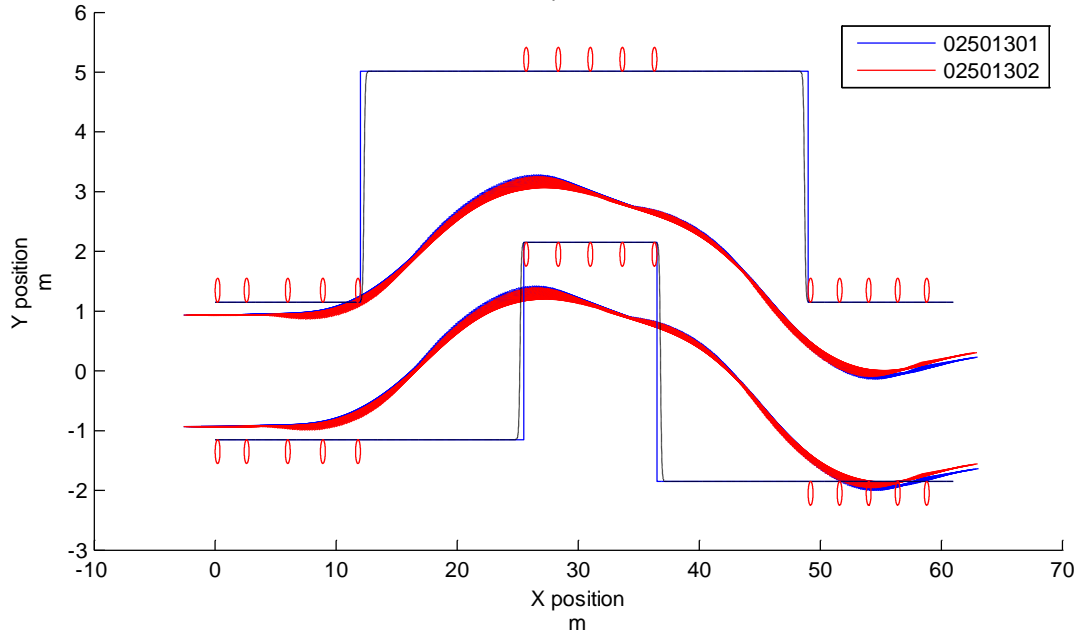


**Figure E 10.** Two track model with tire relaxation and ESC implemented; threshold of  $2^\circ$ , activation torque of 200 Nm and torque increase factor of 5. The vehicle parameters were set to their nominal values.

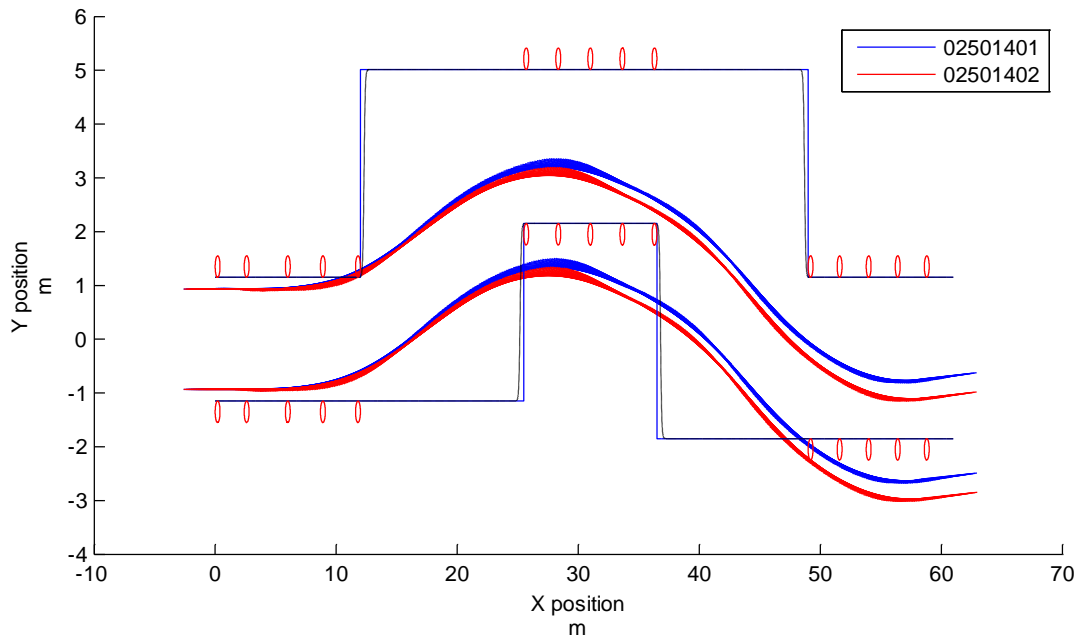


**Figure E 11.** Two track model with ESC implemented; threshold of  $2^\circ$ , activation torque of 200 Nm and torque increase factor of 10. The vehicle parameters were set to their nominal values.

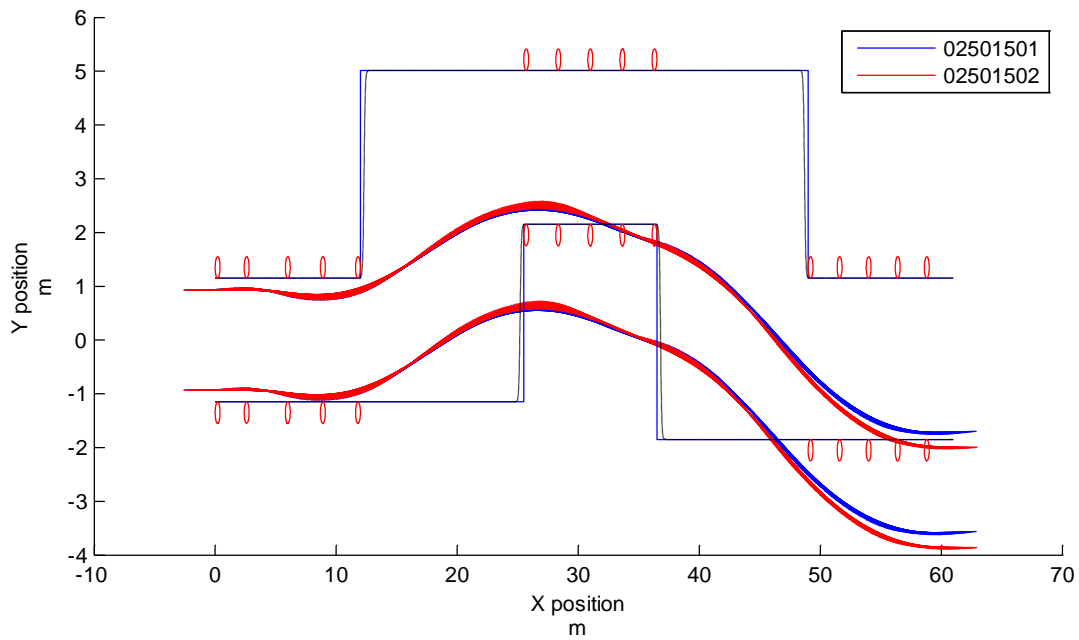


**Figure E 12.** Two track model with tire relaxation and ESC implemented; threshold of  $2^\circ$ , activation torque of 200 Nm and torque increase factor of 10. The vehicle parameters were set to their nominal values.

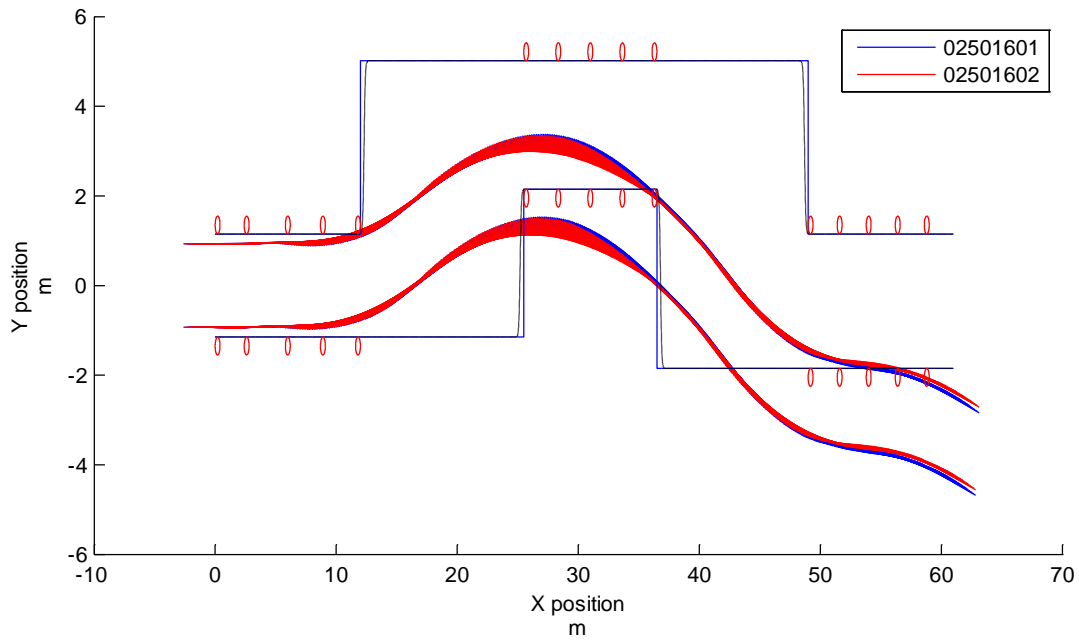


**Figure E 13.** Two track model with ESC implemented; threshold of  $2^\circ$ , activation torque of 100 Nm and torque increase factor of 5. The vehicle parameters were set to their nominal values.

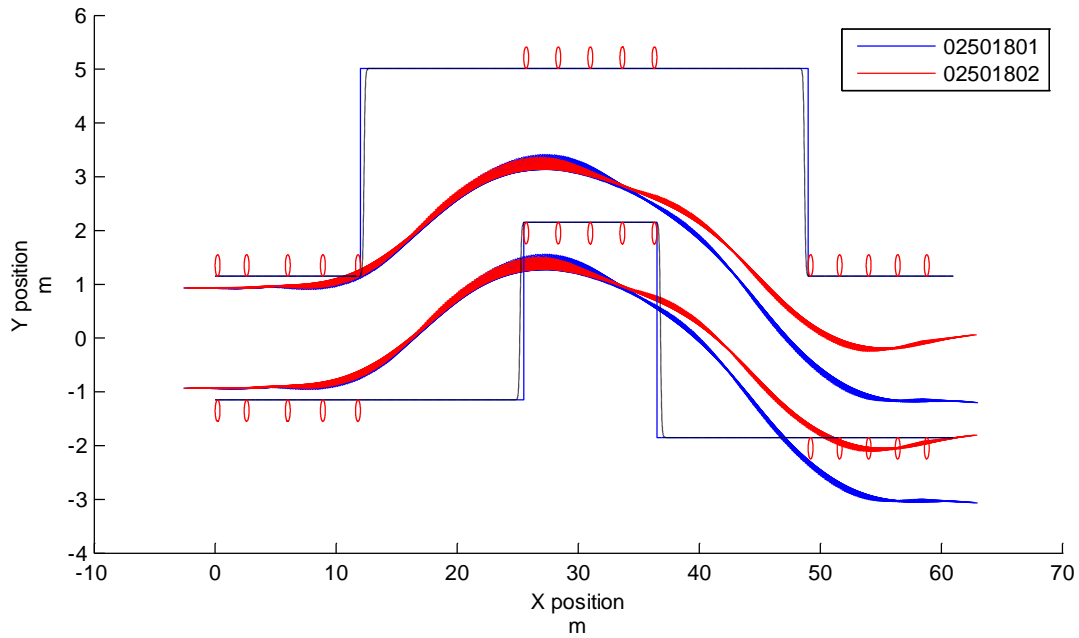


Figure E 14. Two track model with ESC implemented; threshold of  $0^\circ$ , activation torque of 200 Nm and torque increase factor of 5. The vehicle parameters were set to their nominal values.

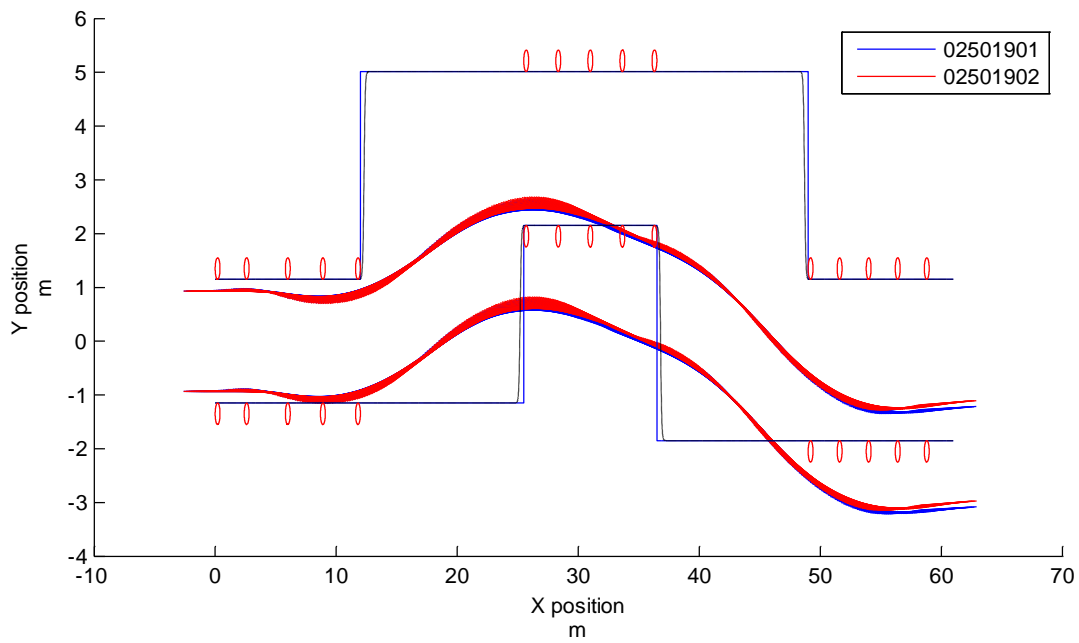
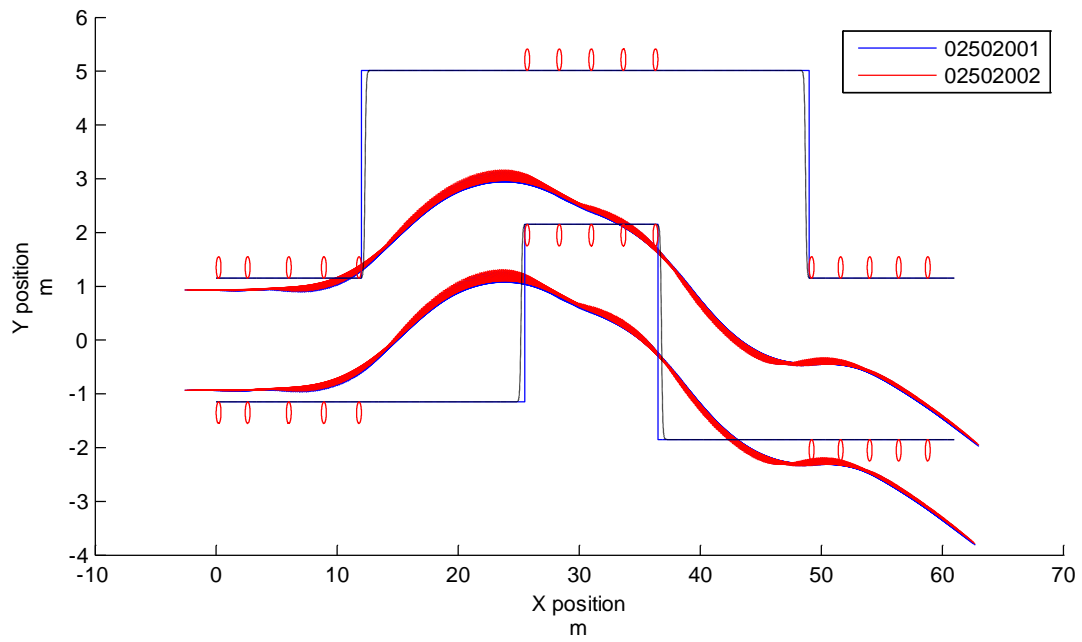
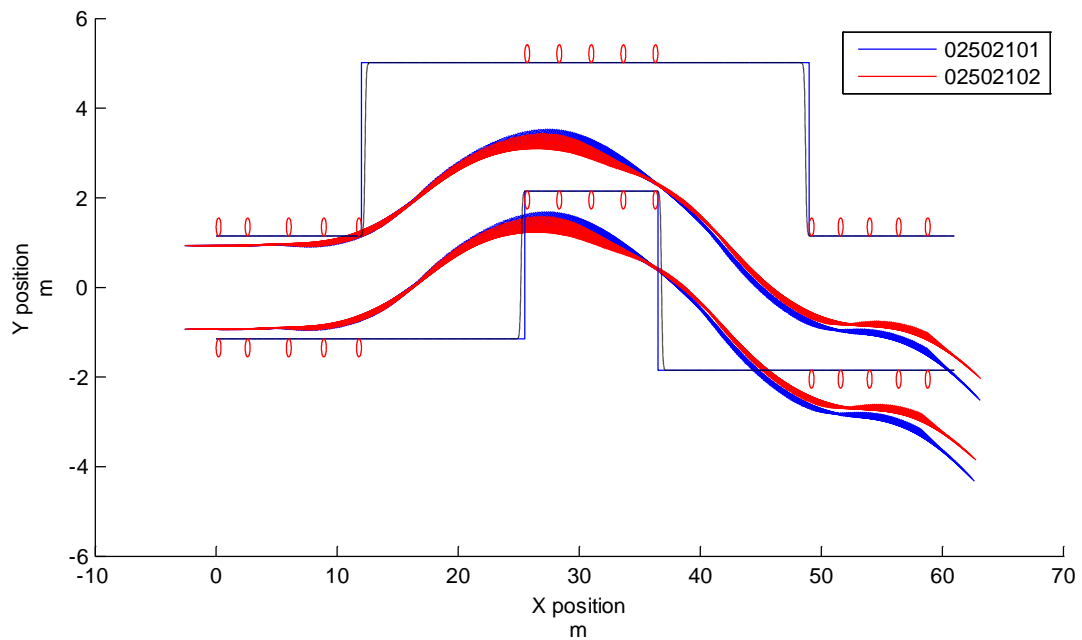


Figure E 15. Two track model with tire relaxation and ESC implemented; threshold of  $0^\circ$ , activation torque of 200 Nm and torque increase factor of 5. The vehicle parameters were set to their nominal values.



**Figure E 16.** Two track model with tire relaxation, wheel kinematics and no ESC implemented. The vehicle parameters were set to their nominal values.



**Figure E 17.** Two track model with no ESC implemented. The vehicle parameters were set to their nominal values.

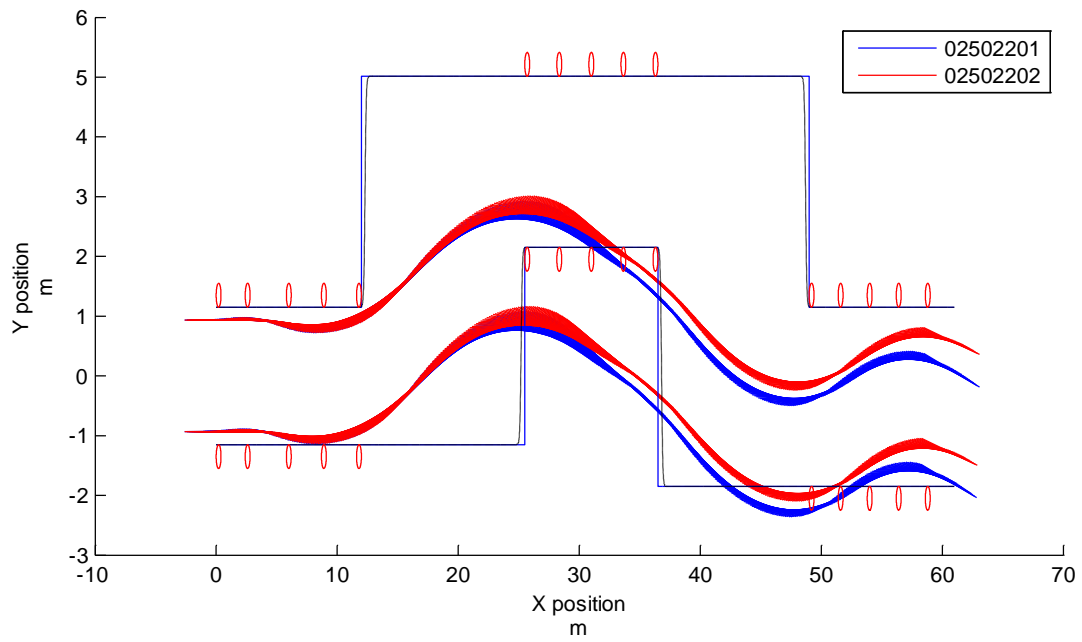


Figure E 18. Bicycle model with Magic formula tires. The vehicle parameters were set to their nominal values.

# F – Code structure

Before the Tomlab solver is called the following need to be coded:

- Phases to use in the solver with start and end time as well as number of collocation points
- Define state variables
- Define control variables
- Initial guess (All states need a guess)
- General boundary conditions (The solution will be within these), optional but facilitates convergence
- Initial boundary conditions (in this case at  $t = 0$ ), optional but facilitates convergence
- Final boundary conditions (in this case at  $t = final\ time$ ), optional but facilitates convergence
- Differential equations
- Additional constraints (A selectable margin for error is allowed)
- Objective function definition

The solver outputs one result variable and optionally a structure in which information about the solver used can be found.

# G – Kinematics & compliance

From Kinematics and Compliance, Volvo S60, Y283 datasheet

## *Roll steer phenomena*

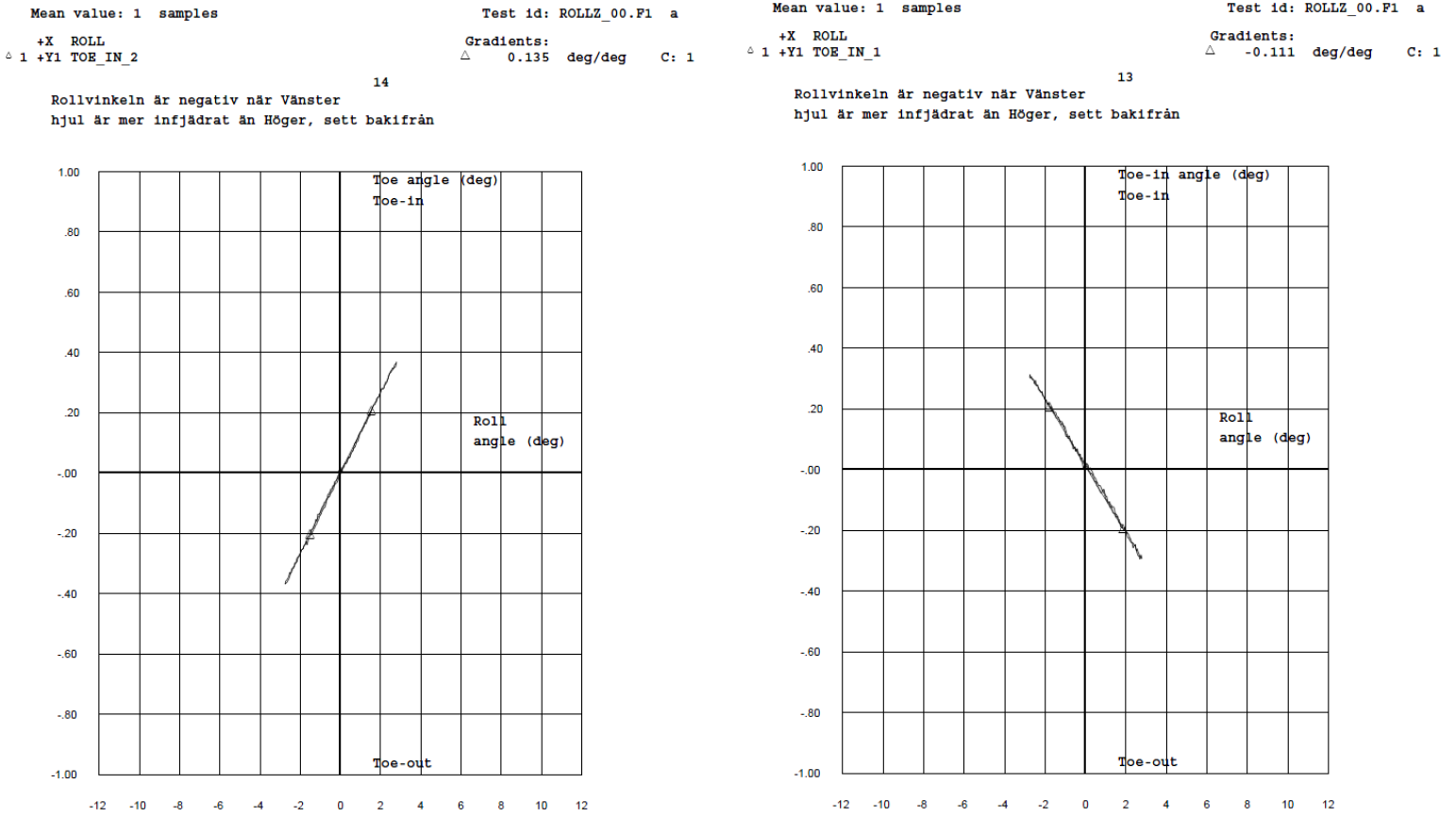
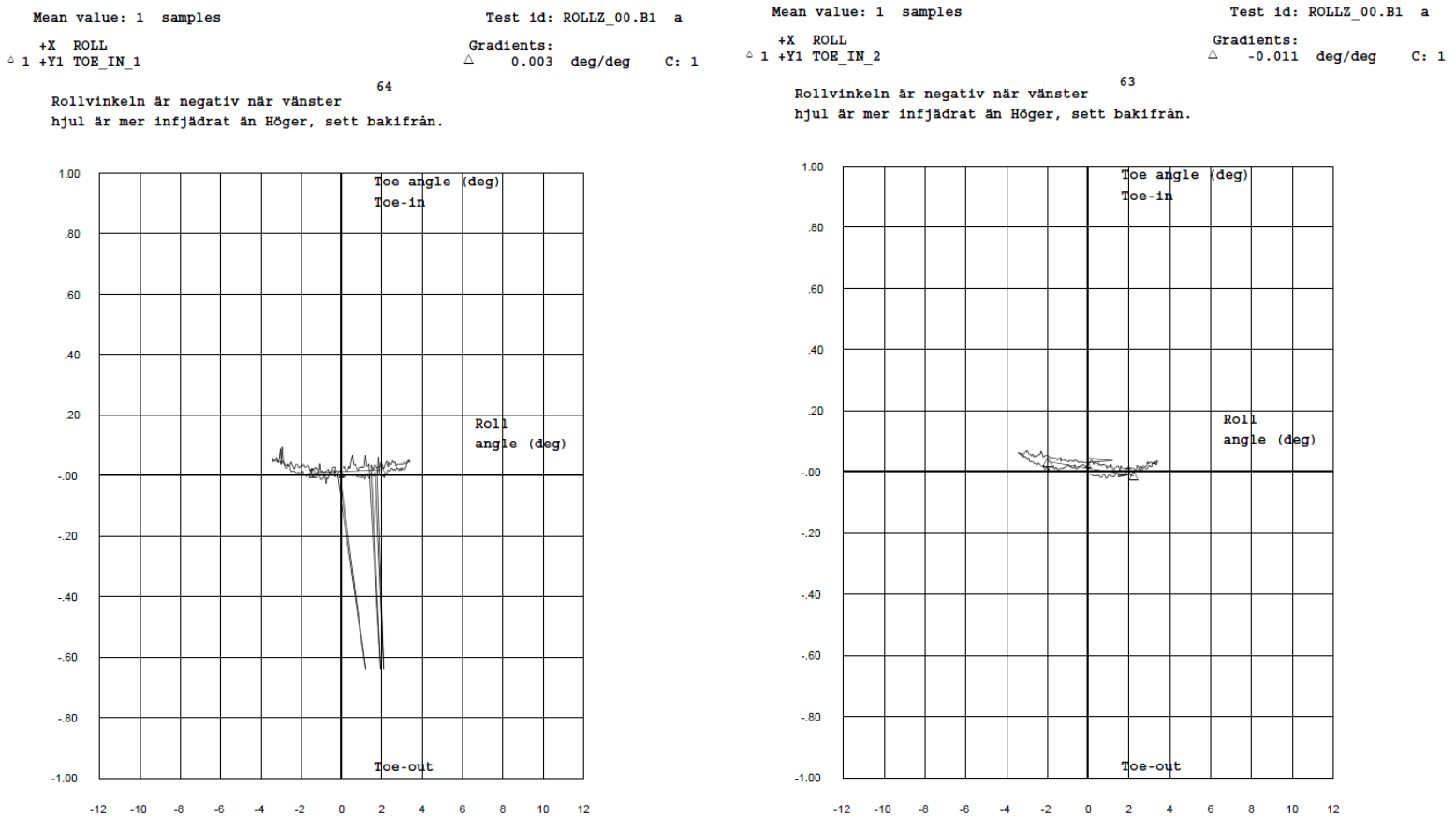


Figure G 1. Toe-in angle at double-sided roll movement. Left Front and Right Front wheel shown in the left and right picture respectively.



**Figure G 2.** Toe-in angle at double-sided roll movement. Left Rear and Right Rear wheel shown in the left and right picture respectively.

### Lateral force compliance steer phenomena

Lateral force applied at ground level (GL), at the middle of the tire-road contact patch ( $X=0m$ ):

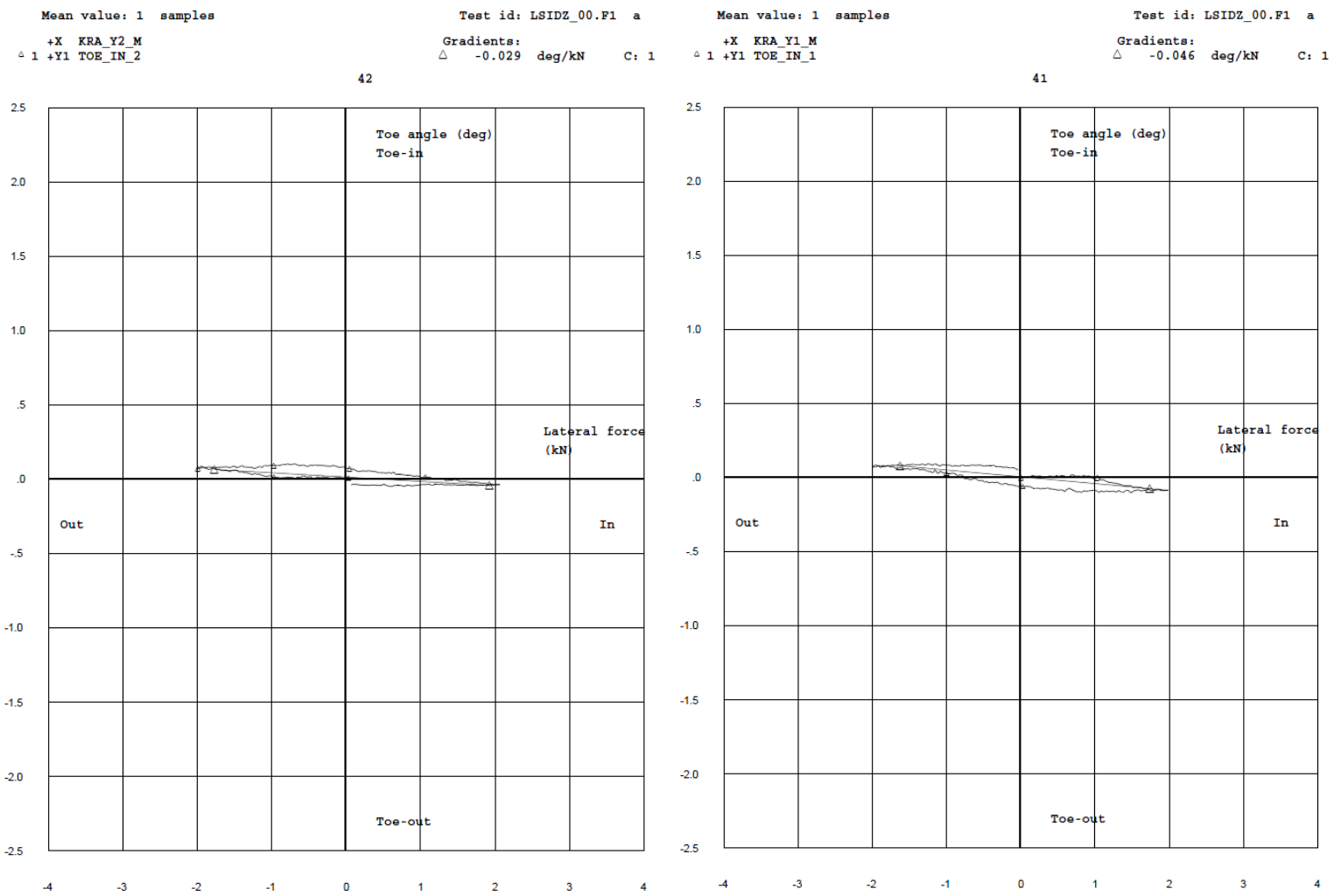


Figure G 3. Toe-in angle at lateral force, GL. Force LH+RH unidirectional at  $X = 0mm$ . Left Front and Right Front wheel shown at the left and right picture respectively.

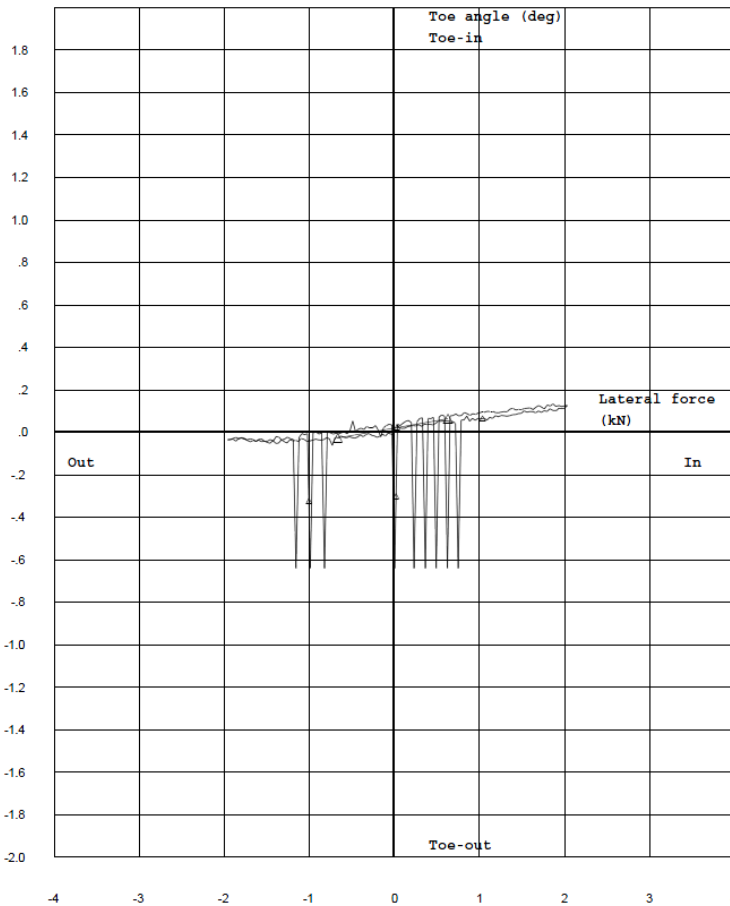
Mean value: 1 samples

+X KRA\_Y1\_M  
△ 1 +Y1 TOE\_IN\_1

Test id: LSIDZ\_00.B1 a

Gradients:  
△ 0.070 deg/kN C: 1

92



Mean value: 1 samples

+X KRA\_Y2\_M  
△ 1 +Y1 TOE\_IN\_2

Test id: LSIDZ\_00.B1 a

Gradients:  
△ 0.065 deg/kN C: 1

91

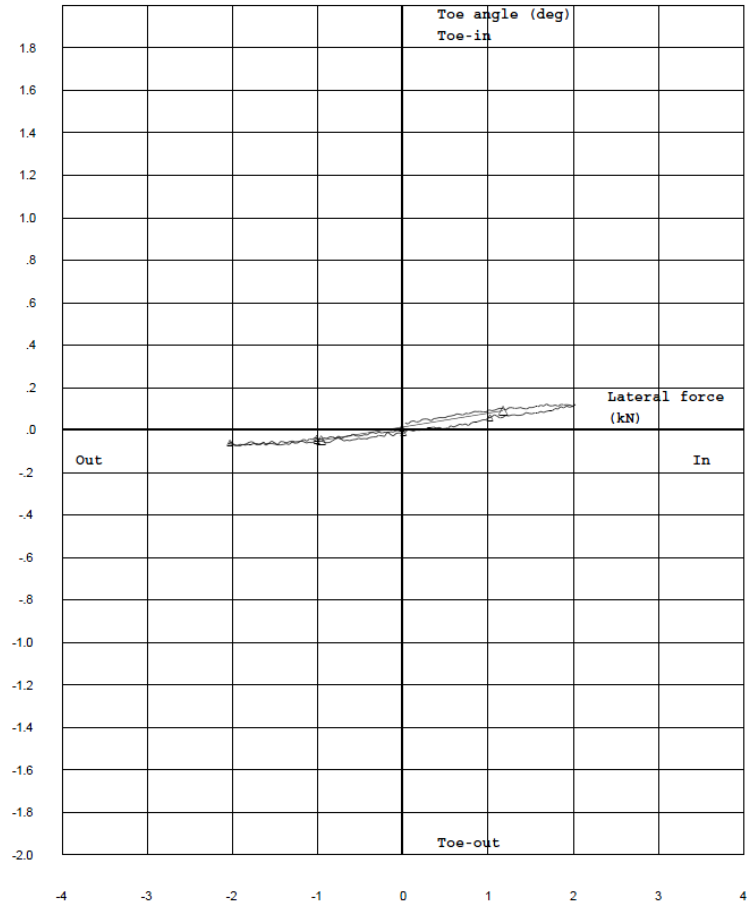


Figure G 4. Toe-in angle at lateral force, GL. Force LH+RH unidirectional at X = 0mm. Left Rear and Right Rear wheel shown at the left and right picture respectively.

*Lateral force applied at ground level (GL), at approximately the distance of the pneumatic trail for low slip angles ( $X=30mm$ ):*

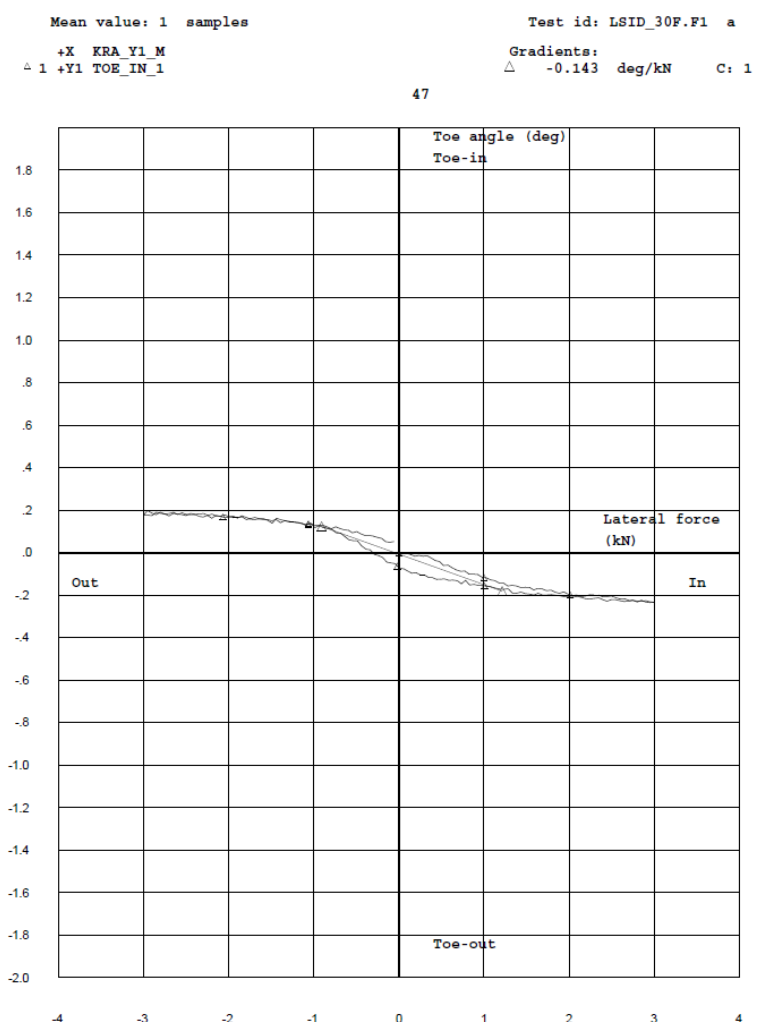
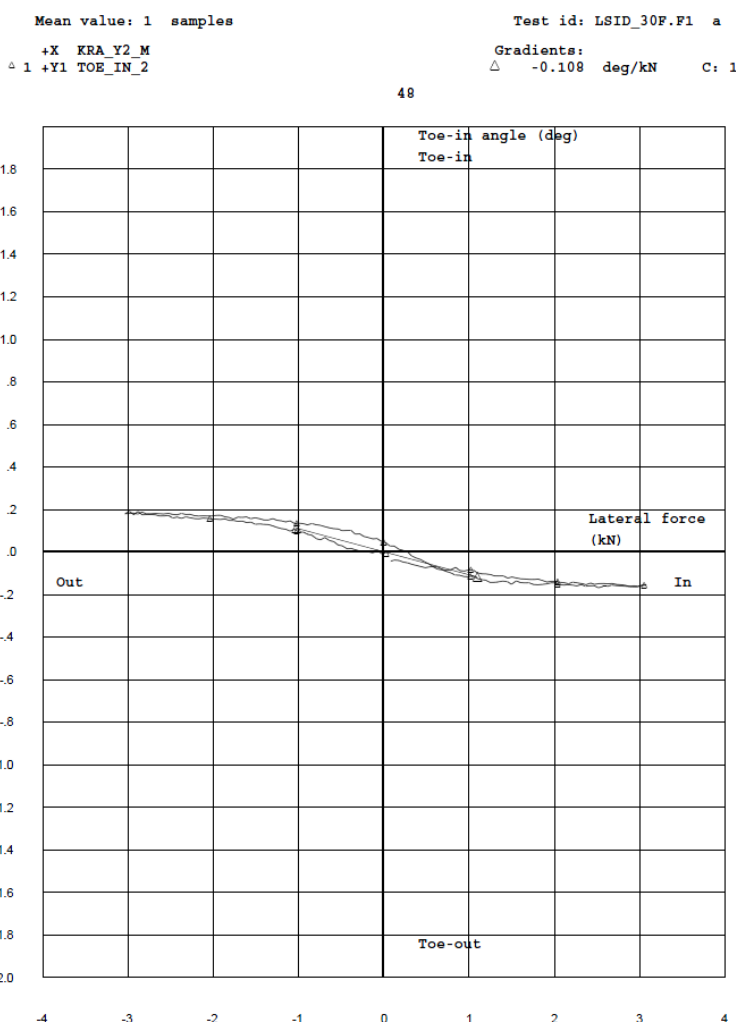


Figure G 5. Toe-in angle at lateral force, GL. Force LH+RH unidirectional at  $X = 30mm$ . Left Front and Right Front wheel shown at the left and right picture respectively.

Mean value: 1 samples

+X KRA\_Y1\_M  
△ 1 +Y1 TOE\_IN\_1

98

Test id: LSID\_30B.B1 a

Gradients:  
△ 0.016 deg/kN C: 1

Mean value: 1 samples

+X KRA\_Y2\_M  
△ 1 +Y1 TOE\_IN\_2

97

Test id: LSID\_30B.B1 a

Gradients:  
△ 0.018 deg/kN C: 1

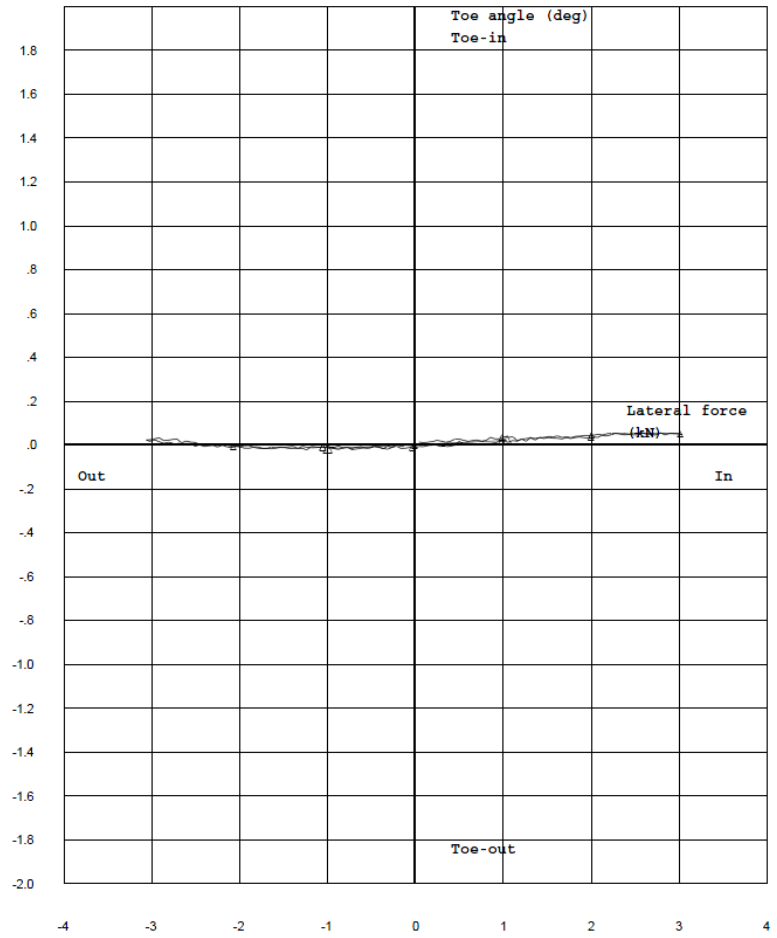
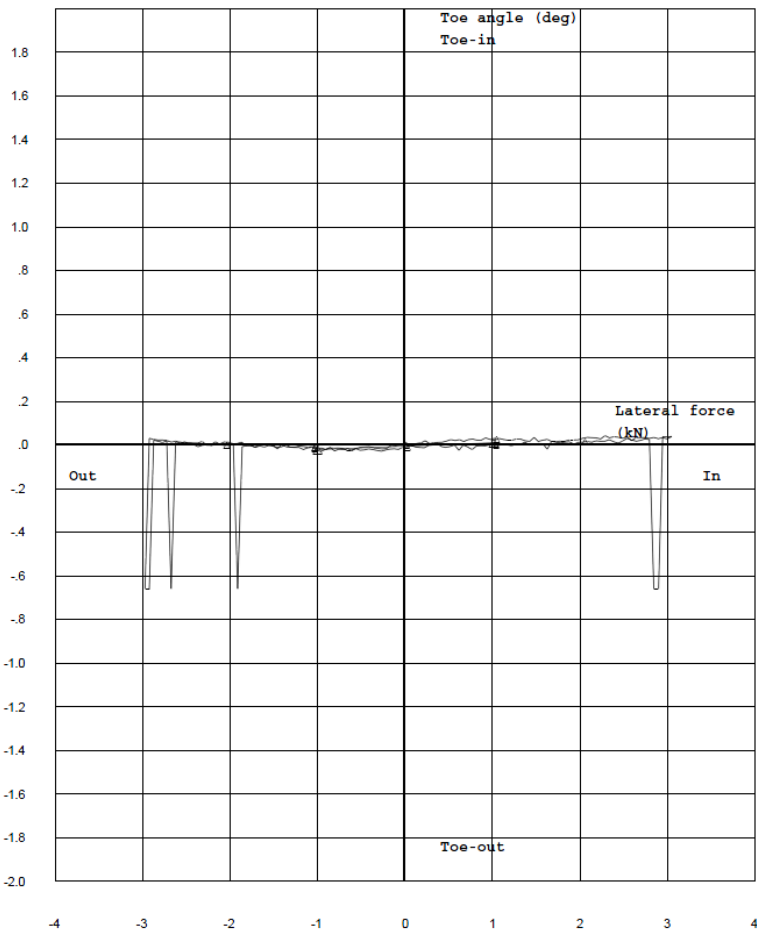


Figure G 6. Toe-in angle at lateral force, GL. Force LH+RH unidirectional at X = 0mm. Left Rear and Right Rear wheel shown at the left and right picture respectively.

## Camber gain due to roll

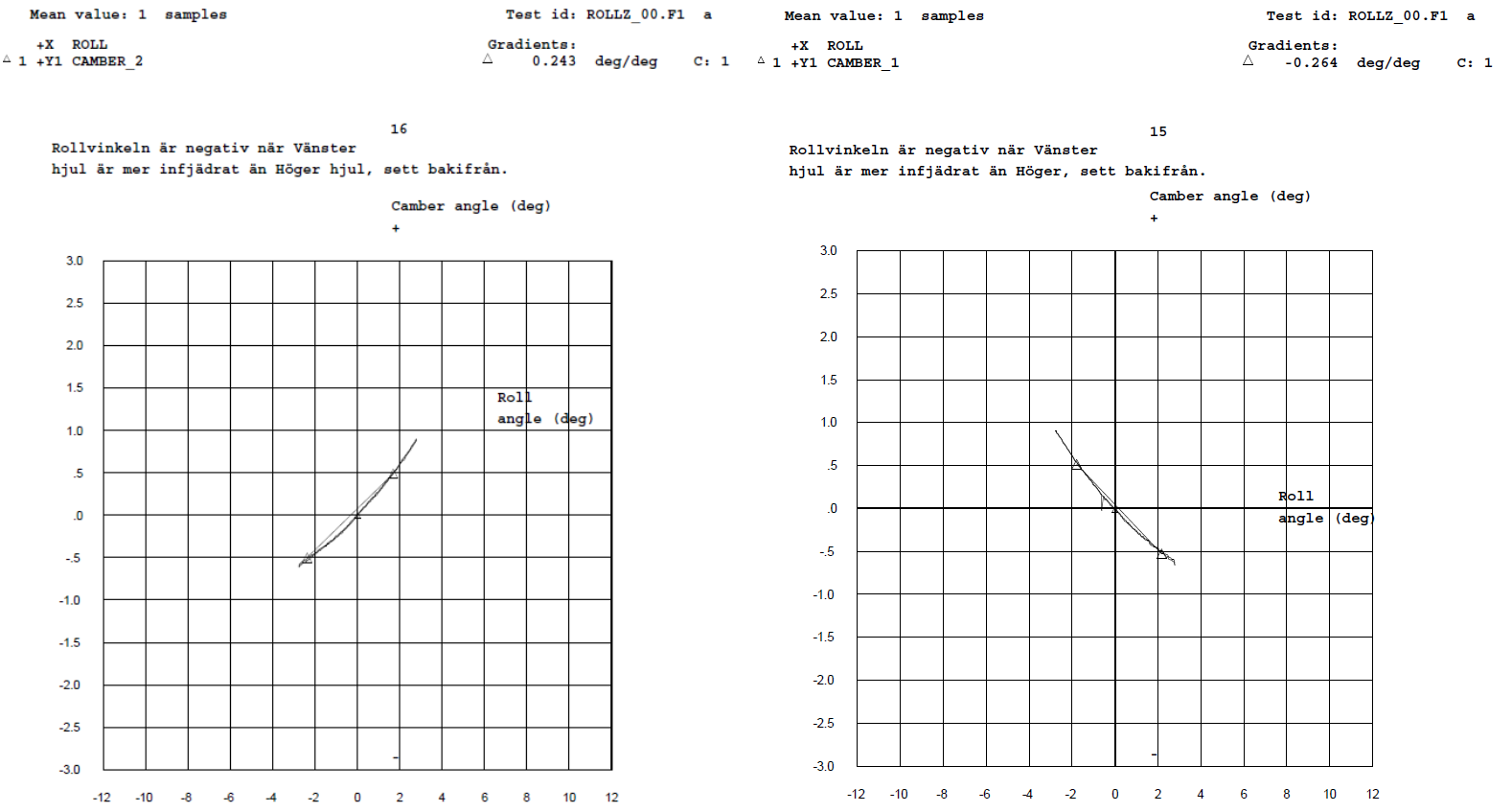


Figure G 7. Camber angle at double-sided roll movement. Left Front and Right Front wheels are shown in the left and right picture respectively.

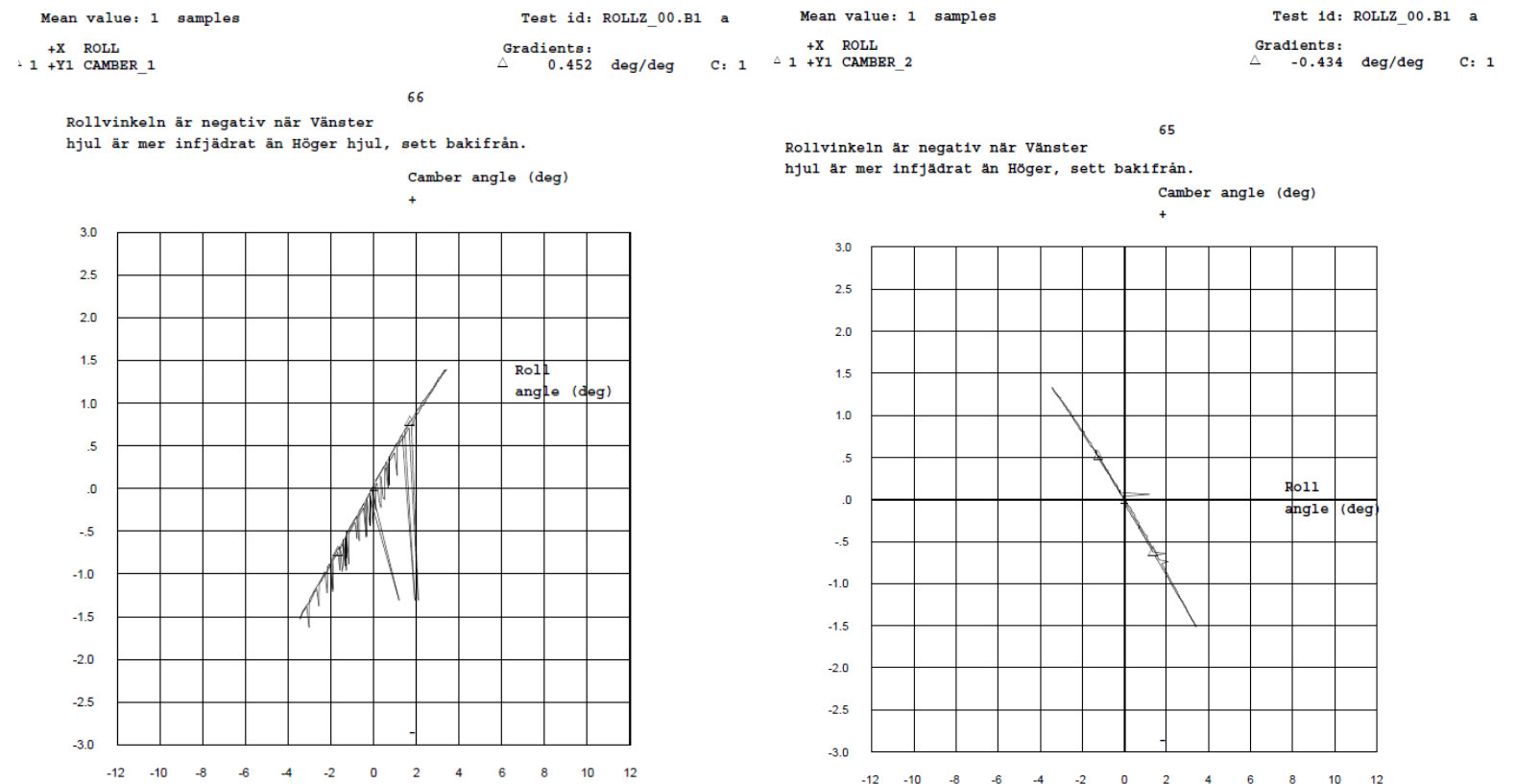


Figure G 8. Camber angle at double-sided roll movement. Left Rear and Right Rear wheels are shown in the left and right picture respectively.

G9

# H - Test 1 data illustration

As an example to illustrate the erroneously recorded data, the recorded lateral velocity from one counter clockwise circular test is plotted in Figure H 2<sup>26</sup>, as well as the respective steering wheel angle in Figure H 1. Those two figures describe two contradictory vehicle behaviours, which prove this data corruption that occurred. In Figure H 1 it can be seen that the steering wheel angle starts from a positive value (that is a counter clockwise turn of the steering wheel) and constantly increases as the longitudinal speed also increases, up to the point that the constant radius cannot be maintained anymore.

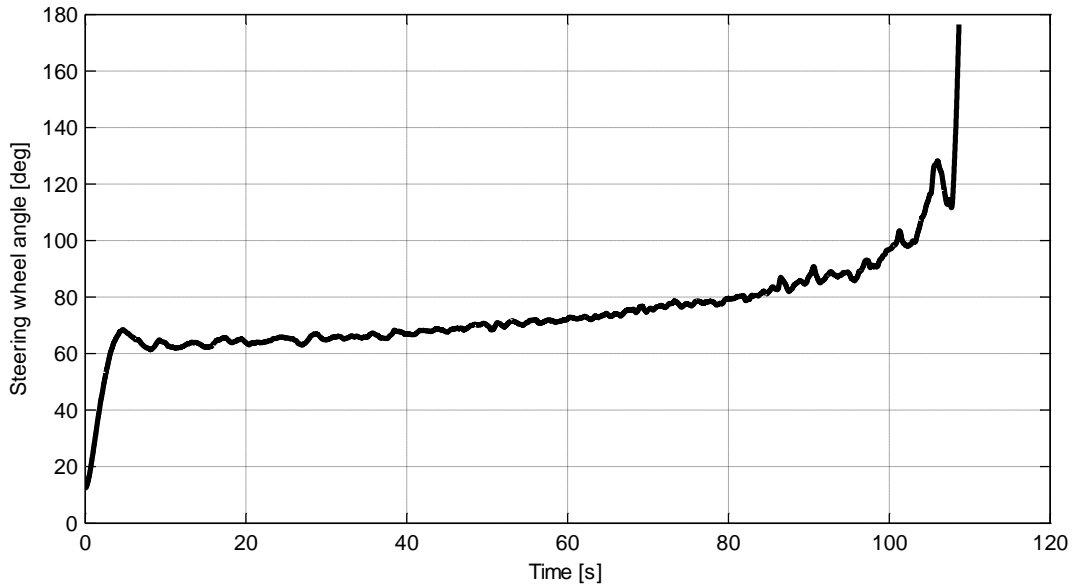
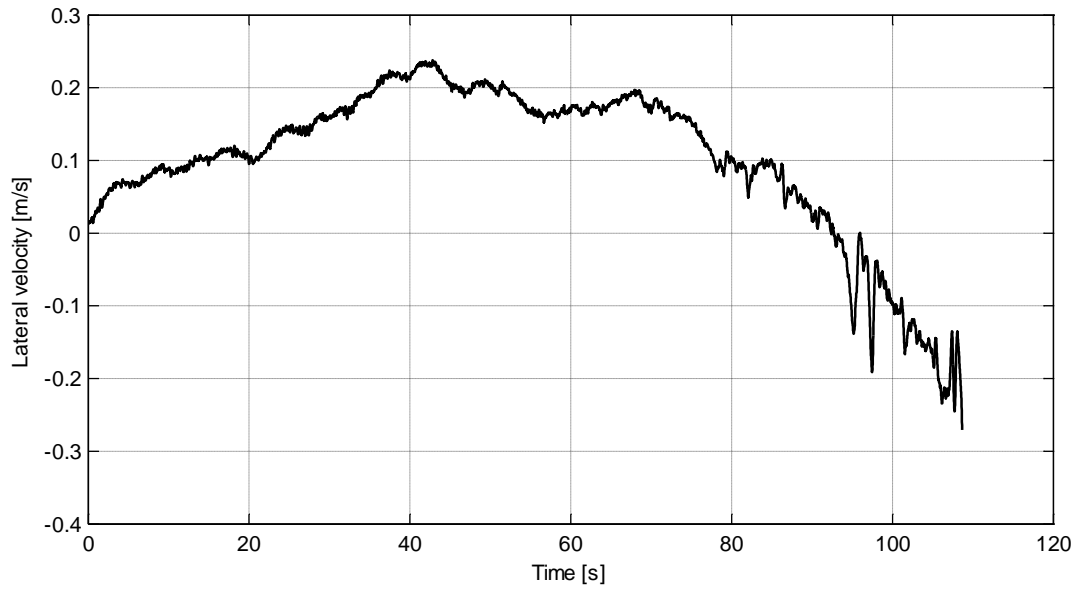


Figure H 1. Steering wheel angle measured by the steering robot.

This implies an understeering behaviour. Next, Figure H 2 is red. The lateral velocity of the vehicle, starting from a positive value, initially increases and after a while it starts decreasing and even changing sign. With the help of Figure H 3 it becomes apparent what this lateral velocity profile indicates: Initially, when the lateral velocity has a positive sign, the vehicle understeers. Up to about 42 seconds the lateral velocity component increases, which means the vehicle tends to understeer even more as the time passes and the longitudinal velocity increases. After the first 42 seconds, though, the vehicle's lateral speed starts decreasing, which means that the vehicle starts to understeer less with an ever increasing longitudinal speed, it then becomes neutral steer at around 90 seconds when the lateral velocity is zero, and then it starts oversteering after that time. This behaviour contradicts the one occurring

<sup>26</sup> The lateral velocity graph is filtered with a low pass filter – see the filtering at the curve fitting part below.

from the graph of the steering wheel angle, which is only increasing, implying constant understeer as mentioned before.



**Figure H 2.** Lateral velocity calculated and recorded by the steering robot.

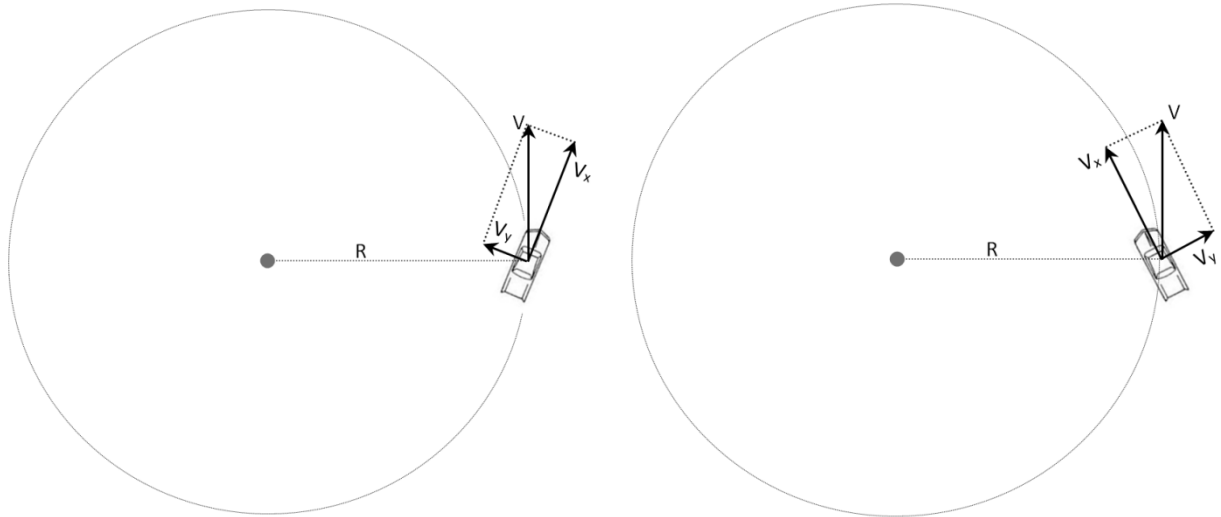


**Figure H 3.** The left case shows a vehicle understeering ( $V_y > 0$ ) during a counter clockwise circular drive while the right case shows vehicle oversteering ( $V_y < 0$ ) during a counter clockwise circular drive.

# I - Simulink bicycle model

Nonlinear Bicycle Model. The model is used for evaluating the B,C,D values for the magic formula  $\mu = D \sin(C \tan(Bs))$  by fitting the yaw rates and lateral accelerations from measurements with the model. In the model, only the lateral slip for the tires is utilized (assume  $s_x=0$ )

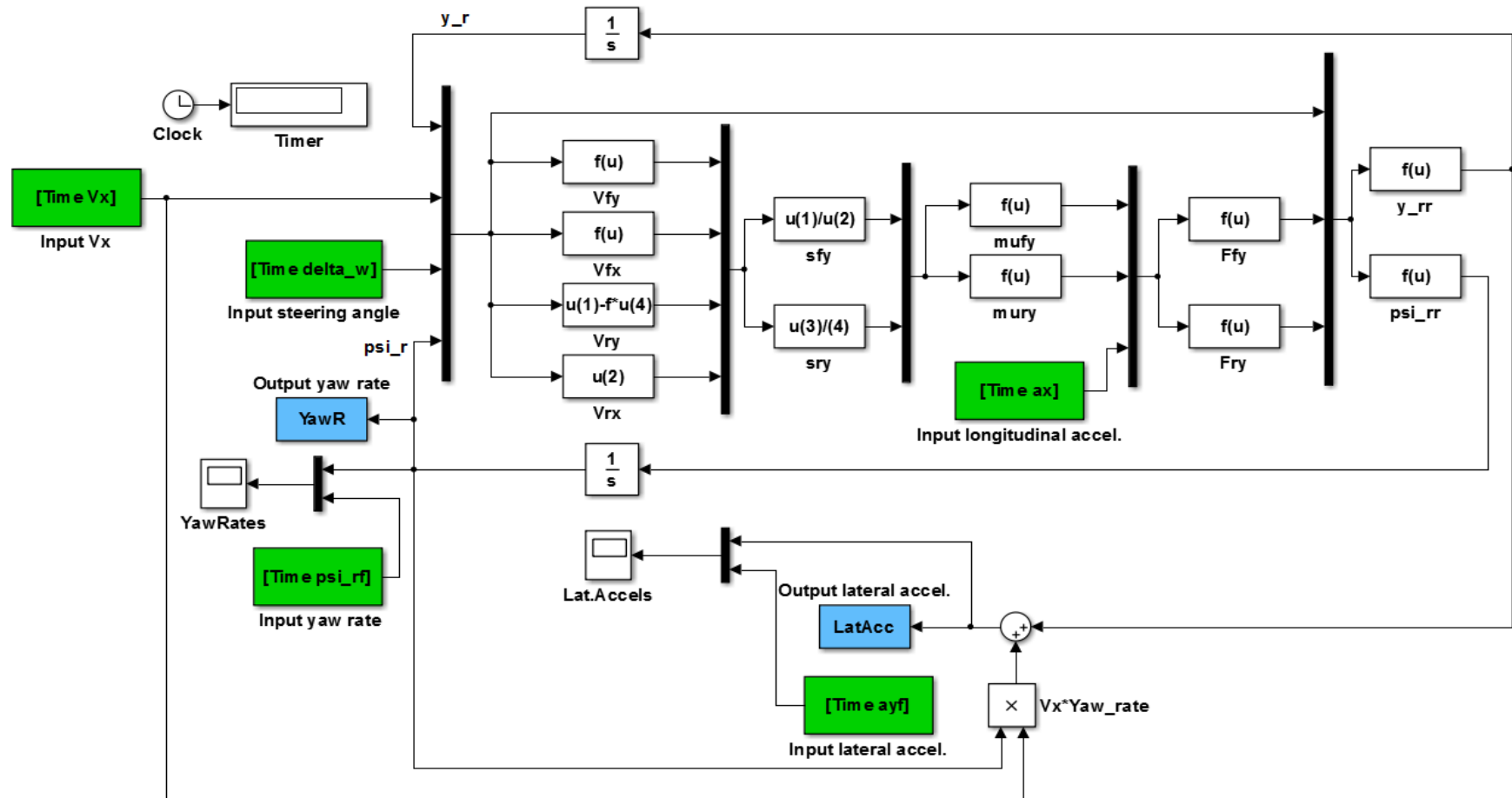


Figure I 1. Bicycle model with nonlinear tire model to be used for curve fitting.

In Figure I 1 Vx is the CoG longitudinal velocity, delta\_w is the steering angle, Vfy is the front wheel lateral velocity, Vfx is the front wheel longitudinal velocity, Vry is the rear wheel lateral velocity, Vrx is the rear wheel longitudinal velocity, sfy is the front wheel lateral slip, sry is the rear wheel lateral slip, mufy is the front wheel lateral friction coefficient, mury is the rear wheel lateral friction coefficient, Ffy is the front lateral force, Fry is the rear wheel lateral force, y\_r is the CoG lateral velocity, psi\_r is the yaw rate, psi\_rr is the yaw acceleration, YawR is the calculated yaw rate, LatAcc is the calculated lateral acceleration, psi\_rf is the measured and filtered yaw rate, ayf is the measured and filtered lateral acceleration and ax is the longitudinal acceleration.